[Browse all Theses and Dissertations](#)

Theses and Dissertations

2017

Low Velocity Impact and RF Response of 3D Printed Heterogeneous Structures

Sandeep Keerthi
Wright State University

Follow this and additional works at: https://corescholar.libraries.wright.edu/etd_all

Part of the Mechanical Engineering Commons

LOW VELOCITY IMPACT AND RF RESPONSE OF 3D PRINTED HETEROGENEOUS STRUCTURES

A thesis submitted in partial fulfillment of the
requirements for the degree of
Master of Science in Mechanical Engineering

By

SANDEEP KEERTHI
B. Tech., Jawaharlal Nehru Technological University, Hyderabad, 2014

2017
Wright State University

WRIGHT STATE UNIVERSITY

GRADUATE SCHOOL

December 6, 2017

I HEREBY RECOMMEND THAT THE THESIS PREPARED UNDER MY SUPERVISION BY Sandeep Keerthi ENTITLED Low-Velocity Impact and RF Response of 3D Printed Heterogeneous Structures BE ACCEPTED IN PARTIAL FULLFILLMENT OF THE REQUIRMENT FOR THE DEGREE OF Master of Science of Mechanical Engineering.

_____

Ahsan Mian, Ph.D.
Thesis Director

_____

Joseph C. Slater, Ph.D., P.E.
Chair, Department of Mechanical and
Materials Engineering

Committee on final examination:

_____

Ahsan Mian, Ph.D.

_____

Joy Gockel, Ph.D.

_____

Raghavan Srinivasan, Ph.D., P.E.

_____

Barry Milligan, Ph.D.
Interim Dean of the Graduate School

ABSTRACT

Keerthi, Sandeep. M.S.M.E., Department of Mechanical and Materials Engineering, Wright State University, 2017. *Low-Velocity Impact and RF Response of 3D Printed Heterogeneous Structures.*

Three-dimensional (3D) printing, a form of Additive manufacturing (AM), is currently being explored to design materials or structures with required Electro-Mechanical-Physical properties. Microstrip patch antennas with a tunable radio-frequency (RF) response are a great candidate for 3D printing process. Due to the nature of extrusion based layered fabrication; the processed parts are of three-layer construction having inherent heterogeneity that affects structural and functional response. The purpose of this study is to identify the relationship between the anisotropy in dielectric properties of AM fabricated *acrylonitrile butadiene styrene* (*ABS*) substrates in the RF domain and resonant frequencies of associated patch antennas and also to identify the response of the antenna before and after a low velocity impact. In this study, ANSYS high frequency structure simulator (HFSS) is utilized to analyze RF response of patch antenna and compared with the experimental work. First, a model with dimensions of 50 mm x 50 mm x 5 mm is designed in Solidworks and three separate sets of samples are fabricated at three different machine preset fill densities using an extrusion based 3D printer LulzBot TAZ 5. The actual solid volume fraction of each set of samples is measured using a 3D X-ray computed tomography microscope. The printed materials appeared to exhibit anisotropy such that the

Thickness direction dielectric properties are different from the planar properties. The experimental resonant frequency for one fill-density is combined with ANSYS-HFSS simulation results to estimate the bulk dielectric constant of ABS and the equivalent dielectric properties in planar and thickness directions. The bulk dielectric properties are then used in HFSS models for other two fill densities and the simulated results appear to match reasonably well with experimental findings. The similar HFSS modeling scheme was adopted to understand the effect of material heterogeneity on RF response. In addition, a hybrid structure with dimensions of 50 mm x 50 mm x 20 mm is designed with the first 15 mm thickness being a cellular BCC structure and the other 5 mm being a solid cuboid. These samples are printed on an extrusion based 3D printer Stratasys uPrint using ABS. A patch antenna is embedded at the interface of the solid and the cellular structure. Both ABAQUS finite element modeling and experimental methods are used to understand the load-displacement and the energy absorption behavior of the hybrid structure under low velocity impact loadings. The hybrid structure is impacted on both sides to investigate the damage tolerance capabilities of embedded electronic components.

TABLE OF CONTENTS

Title	Page

LIST OF FIGURES

LIST OF TABLES

xvi

LIST OF NOMENCLATURE

ε_r Relative dielectric constant

F   Applied force, N

g   Acceleration due to gravity, m/s^2

h   Height, m

K   Stiffness, N/m

KE   Kinetic energy, Joule

M   Mass, Kg

PE   Potential energy, Joule

t   Time, sec

v Velocity, m/s

W   Total energy absorbed, Joule

x Deflection, mm

LIST OF ACRONYMS

3D	3-Dimensional
ABS	Acrylonitrile Butadiene Styrene
AM	Additive Manufacturing
AISI	American Iron and Steel Institute
ASTM	American Society for Testing and Materials
BC	Boundary Condition
CAD	Computer Aided Design
CST	Computer Simulation Technology
Cumtrapz	Cumulative Trapezoidal Integration MATLAB Function
EM	Electro-Magnetic
FDM	Fused Deposition Modeling
FEA	Finite Element Analysis
HFSS	High Frequency Structure Simulator
ISO	International Standards Organization
SLM	Selective Laser Melting
STL	STereoLithography
VNA	Vector Network Analyzer

ACKNOWLEDGMENTS

Dedicated to my family

CHAPTER 1 : INTRODUCTION

1.1 Overview

In this chapter, 3D printing or additive manufacturing (AM) is briefly explained, focusing on the types of AM technologies. Microstrip patch antenna and cellular structures are discussed. The motivation behind developing a hybrid structure is discussed.

1.2 Microstrip Patch Antenna

An antenna is transducer that transmits or receives electromagnetic (EM) waves. The antenna transforms the electric current into electromagnetic waves by transmitting a signal into radio waves and vice-versa by receiving. The IEEE definition of an antenna is "That part of a transmitting or receiving system that is designed to radiate or receive electromagnetic waves". Planar antennas, such as microstrip antennas are very attractive because of their low profile, small size and ease of integration with active integrated circuits. The microstrip antenna consists of a ground plane on one side of a dielectric substrate that has a radiating metallic patch on the other side as shown in Figure 1.1. The size and shape of the patch determine the operating frequency of the antenna and its performance. The patch is generally made up of a conducting material such as copper or gold and can be of any possible shape like circular, elliptical, rectangular, triangular etc. This antenna can be easily attached on the surface of satellites, aircrafts, space crafts, missiles and even on the mobile devices. Microstrip patch antenna radiates mainly due to the fringing fields between the ground plane and the patch edge [1]. For good antenna

performance, a thick dielectric substrate having a low dielectric constant (<6) is desirable since it provides better radiation, larger bandwidth and higher efficiency.
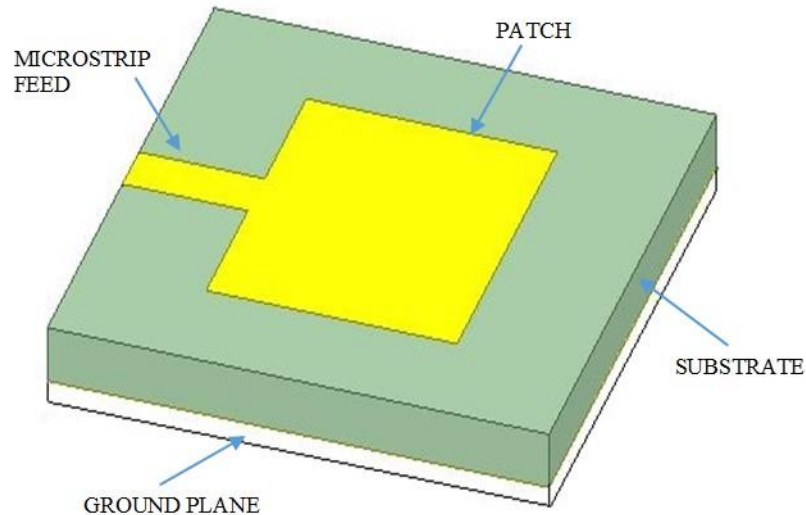
Figure 1.1 Schematic of a Microstrip patch antenna.

Excitation directs the electromagnetic energy source to the patch, producing negative charges around the feed point and positive charges on the other part of the patch. Three types of electromagnetic waves are radiated due to the difference in the charges. The first part is the useful radiation which is radiated into space. The second part is diffracted waves, which are reflected back into space between the patch and the ground plane, contributing the actual power transmission. The third part of the wave remains trapped in the dielectric substrate due to total reflection at the air-dielectric separation surface which are generally neglected.

Conformal application is a key area that can tremendously benefit from the design and manufacture of microstrip antenna arrays as because such arrays can be made to be the integral part of a structure such as an air vehicle, a car or a projectile. Microstrip antennas and arrays require one or more layers of dielectric substrates in order to obtain proper

functionalities, e.g. resonant frequency, bandwidth, gain, pattern, polarization, beam scanning etc. The advent of additive manufacturing brought forth new opportunities for low loss substrate and radome design which will undoubtedly facilitate highly efficient microstrip patch antennas and array design and development especially those that are conformal. While a thick dielectric substrate with low dielectric constant is desirable for a single patch antenna for wide bandwidth and high efficiency [2] dielectric constant variation in the lateral as well as in the thickness direction could be keys to achieve good radome material design.

1.3 Cellular Lattice Structure

Cellular structures have unique functional characteristics that leverage design freedom beyond the capability of solid structures. These characteristics include enhanced absorption of mechanical energy, high specific stiffness and strength, and heat transfer control [3]. The idea of designing cellular structures is inspired by the motive to place material only where it is required for a specific application. From a mechanical engineering perspective, the key advantage offered by cellular materials is high strength-to-weight ratio [4]. Some examples of cellular structures are honeycomb, foam, and lattice structure as shown in Figure 1.2. Cell structures are shaped by intermittent or hypothetical arrangements of closed or open cell types, with either two-dimensional cell configuration (e.g. honeycomb) or three-dimensional polyhedral formats (e.g. cross section structures). The mechanical behavior of the cellular structures is reliant on factors, for example, number of cells, cell topology, geometric parameters, including strut diameter and cell dimensions; material and assembling process qualities; and also structural boundary and loading conditions.
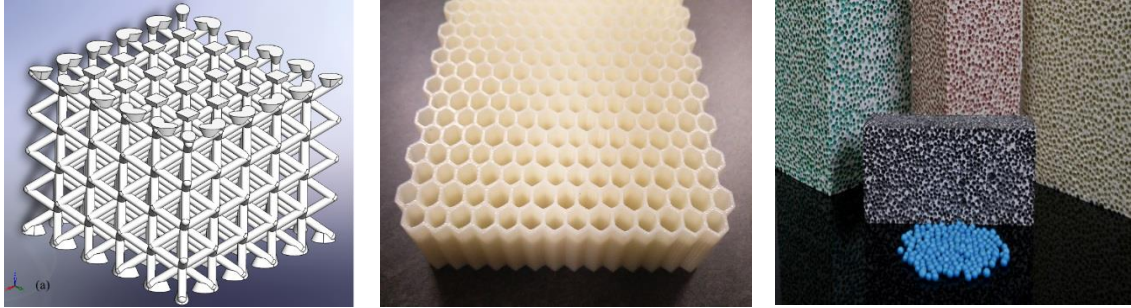
Figure 1.2 Cellular structures (a) Lattice, (b) Honeycomb, (c) Foam [5].

Generally, open-cell lattice structures indicate either a stretch or a bending dominated behavior depending on cell topology. Lattice structures are therefore of specific interest; by choosing the cell topology they can address a range of structural requirements, from high compliance (for an energy absorption or dampening) to high specific strength (for light weight structure) [3]. The smallest group of struts in the structure that constitute a repeating pattern is termed as unit cell. The unit cell effectively defines the symmetry and structure of the entire lattice, which is built up by repetitive construction of the unit cell along its principal axes [6]. There are many types of unit cell configurations available. Some of them are shown in Figure 1.3.

There are several methods to fabricate these lattice structures. 3D printing method is considered to be fast and easy for printing these lattice structures. In this thesis work, Body Centered Cubic unit cell (BCC) of dimension 5 mm x 5 mm x 5 mm is used to design and fabricate lattice structures and a low-speed impact test is performed on the printed samples.

4
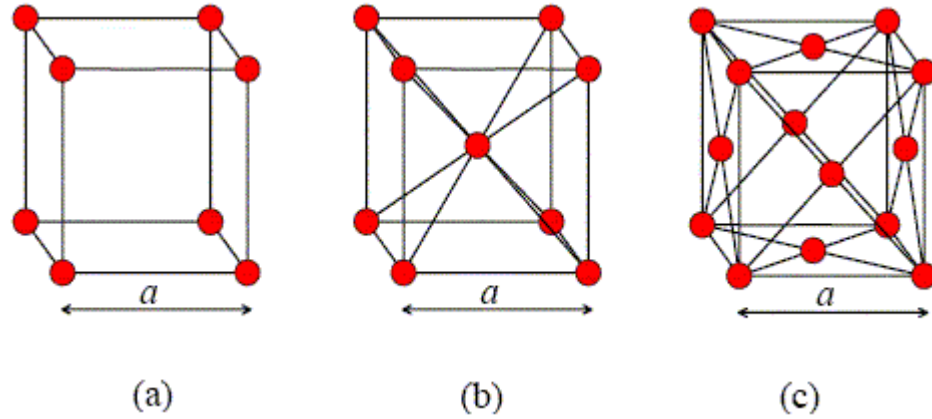
Figure 1.3 (a) Simple Cubic, (b) Body Centered Cubic, (C) Face Centered Cubic [7].

1.4 Additive Manufacturing

Additive manufacturing (AM), generally known as 3D printing, rapid prototyping or freeform fabrication, is a unique technology that operates by deconstructing a geometry into distinct layers, then building up those layers one-by-one. As opposed to subtractive manufacturing methodologies like milling, machining etc., AM fabrication deposits material on top of the material discreetly layer-by-layer to build a 3D form (Figure 1.4).
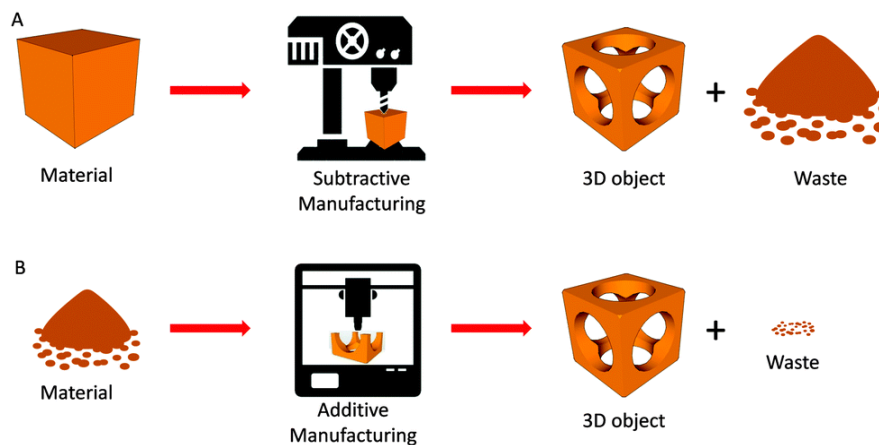
Figure 1.4 Additive vs. Subtractive manufacturing [8].

The real material of the end product can be substituted with other 3D printable materials to test "form, fit, and function" which likely reduces the cost of time and material

stock to produce. This model can be tested to match the visual and engineering specifications, and also completeness, accuracy, and overall design integrity [9, 10]. Usually, a model is designed in a computer aided design (CAD) software like Solidworks, and converted into STereoLithography (STL) file format which is recognized by most of the 3D printers to print the objects.

The American Society for Testing Materials (ASTM) has classified AM into following categories as shown in Figure 1.5.
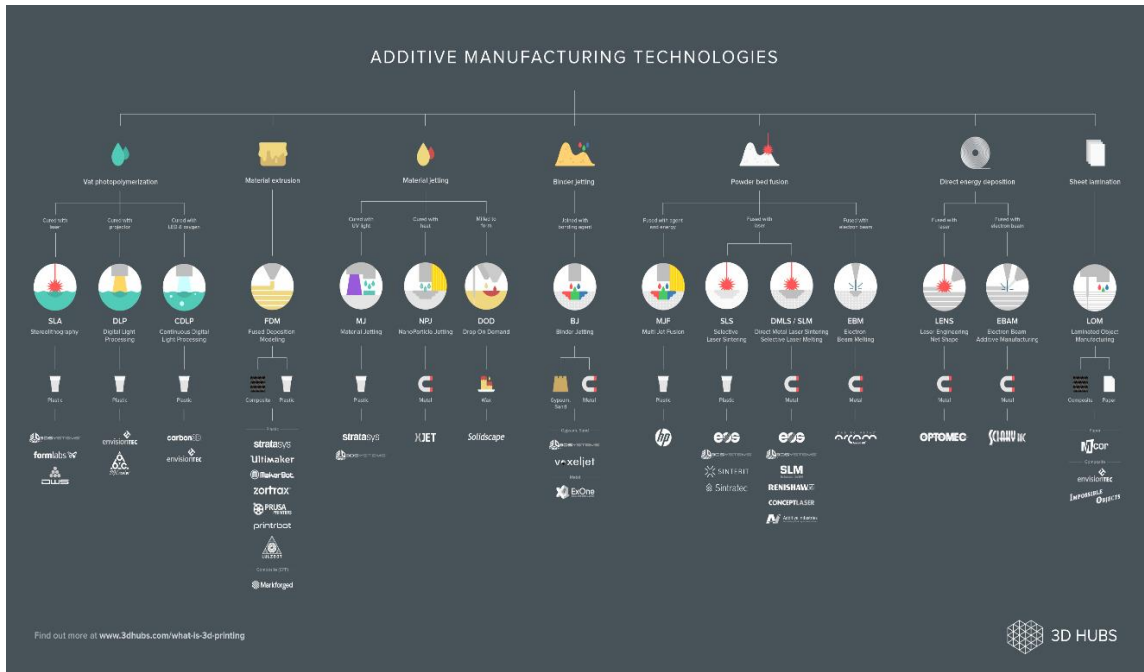
Figure 1.5 Additive manufacturing technologies infographic [11].

1.4.1 Vat Photopolymerization

In this process, 3D objects are created by solidifying a liquid (photopolymer) resin with the help of a light source. A build platform is submerged into a translucent tank filled with liquid resin. A light present inside the machine maps each layer of the object through the base of the tank, thereby thickening the material. After the layer has been mapped and

6

solidified by the light source, the stage lifts up allowing a new layer of resin flow beneath the object. This procedure is iterated to build the 3D form of the object. This process is differentiated by the light source into two types: (a) Stereolithography (SLA) uses a laser, (b) Digital Light Processing (DLP).
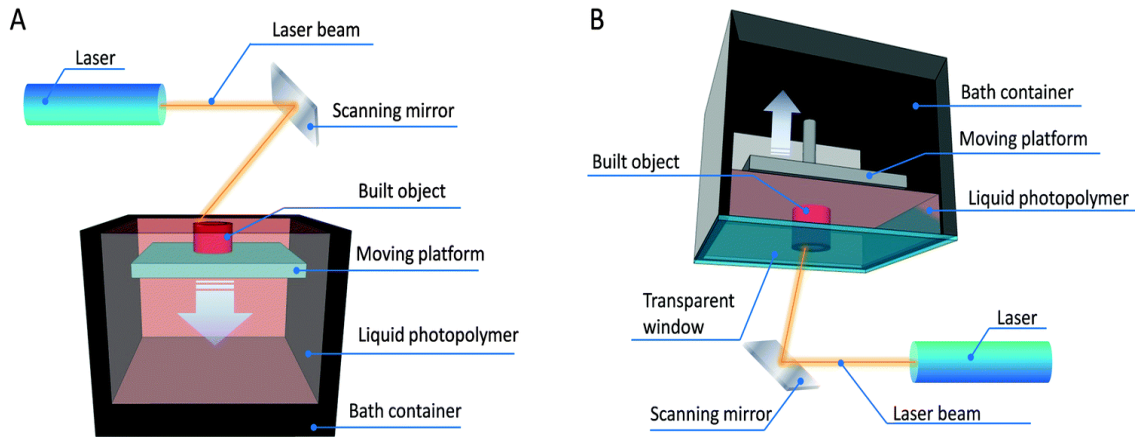
Figure 1.6 SLA 3D printer where laser is scanned, (A) across the liquid surface and (B) from the bottom of the liquid tank [8].

1.4.2   Fused Deposition Modeling (FDM)

This is the popular technology available in the desktop 3D printers due to its quick and low-cost prototyping. The FDM technique utilizes a string of solid material called the filament, which is guided from a reel through a tube into a heated nozzle which is maintained at certain temperature. The filament in molten state is extruded on a specific and foreordained path created by the software on the computer. The bed of the printer is also maintained at certain temperature. The material extruded on the bed, gradually cools down and solidifies – providing the foundation for the next layer of material to be printed [11].
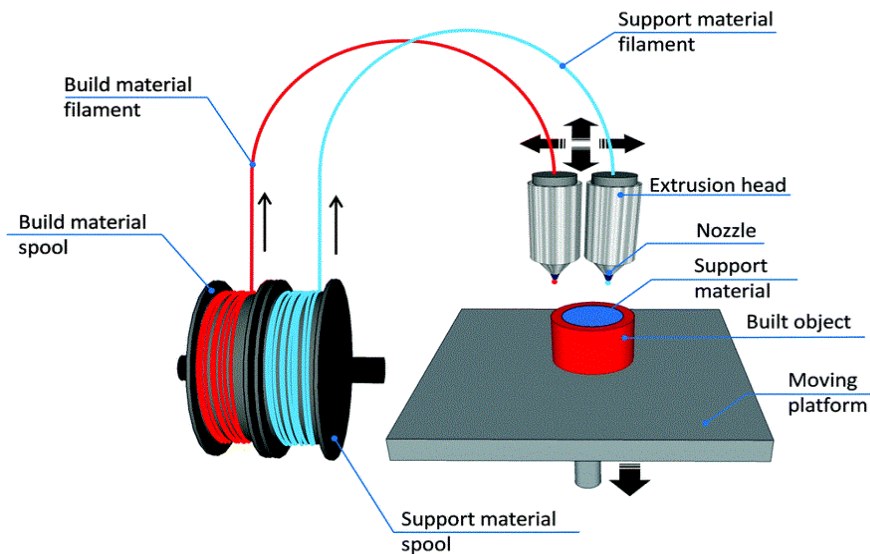
Figure 1.7 Schematic diagram of FDM technology [8].

1.4.3 Selective Laser Sintering (SLS)

Selective laser sintering is the process in which layers of powdered material are melted and solidified into finished objects using a laser. The printer consists of two beds which are called as pistons. In this process, the first layer of the powder is mapped with a laser, which selectively melts – or sinters – the material. After the solidification of the first layer, the bed moves downwards and the other bed with the powder moves up; and a roller spreads a new layer of powder atop the object [11]. This process is iterated layer by layer until the desired object is printed. SLS is widely used for fabricating end products as well as some parts for functional prototypes. The advantages of laser sintering include design freedom, and the excess unmelted powder acts as a support for the printed structure with intricate and complex geometries.
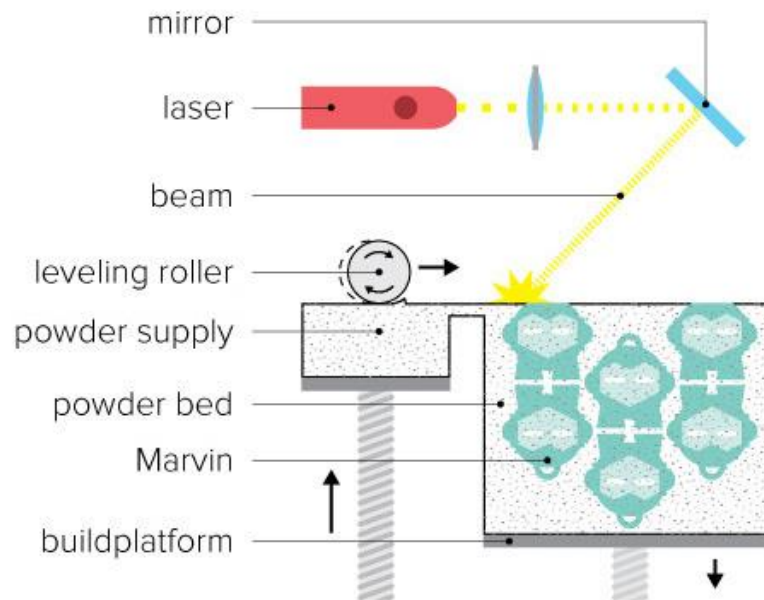
Figure 1.8 Schematic diagram of SLS technology [11].

1.4.4 Material Jetting

Material jetting is the process in which layers of tiny droplets of photopolymer are sprayed onto a build tray, which are instantly cured with the help of a UV light. These thin layers compile together to create precise object on the build tray. In case of complex and intricate structure, the printer jets a removable gel-like support material, which can be removed after the fabrication. The selection of the liquid photopolymer depends on various properties including toughness, transparency or rubber-like flexibility. Material Jetting has many advantages that include rapid tooling, functional prototyping with fine details and precision. These 3D printers have a layer resolution of 16-micron layers [11]. This technology is also termed as drop on demand, multi-jet modeling. The drawback of the technology is that it only works with wax-like materials.

9
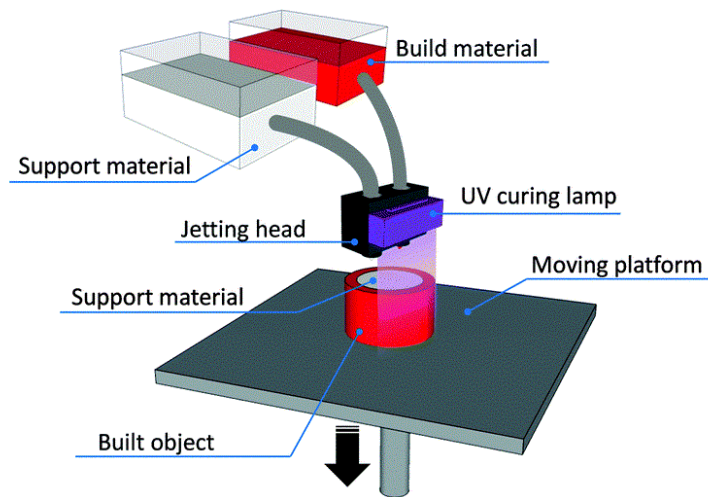
Figure 1.9 Schematic diagram of Material Jetting [8].

1.4.5   Binder Jetting

Binder jetting technology is similar to SLS printing technology. These printers use a binding agent to bind the powder together whereas in SLS printers utilize a laser that sinters the powder together [11]. A powder supply integrated with a leveling roller spreads a thin layer of powder material onto the building platform. An inkjet dispenser controlled by a monitor deposits the glue (or binder) liquid according to the layer design. Once the first layer is completed, a second layer of powder is distributed on the top of the first layer. This is achieved by the controlled downward movement of the building platform and upward movement of the supply container [8]. This technology is unique as there is no heat employed in the build process whereas in other AM technologies, a heat source is used which creates residual stresses in the printed object.
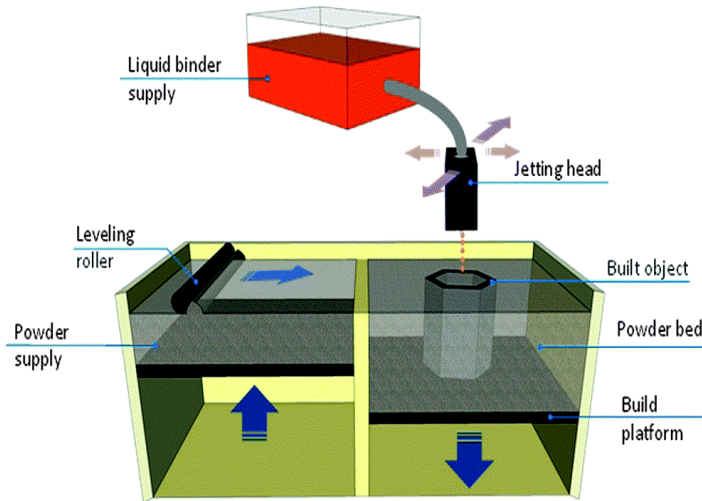
Figure 1.10 Schematic diagram of Binder Jetting [8].

1.4.6 Metal Printing

In the last decade, metal 3D printing has become increasingly popular. Selective Laser Melting and Electron Beam Melting (SLM and EBM) are the most commonly used metal 3D printing technologies. When compared with the traditional machined part, the 3D printed part is light in weight and saves a lot of manufacturing time. In metal 3D printing process, a layer of metal powder is distributed on the bed, which is melted by an electron beam or a laser. A new layer of metal powder is distributed on the top of the previous layer as the build platform lowers and this process iterates until the object is fabricated [11]. Both SLM and EBM require support structures enabling the heat transfer away from the melted powder. SLM requires a low oxygen environment and EBM requires vacuum in order to reduce thermal stresses and prevent warping. The application of such printers is widely in aerospace, aircraft, automotive and healthcare industries. Materials like steel, titanium, aluminum, cobalt-chrome and nickel can be printed using this printing technology.

11
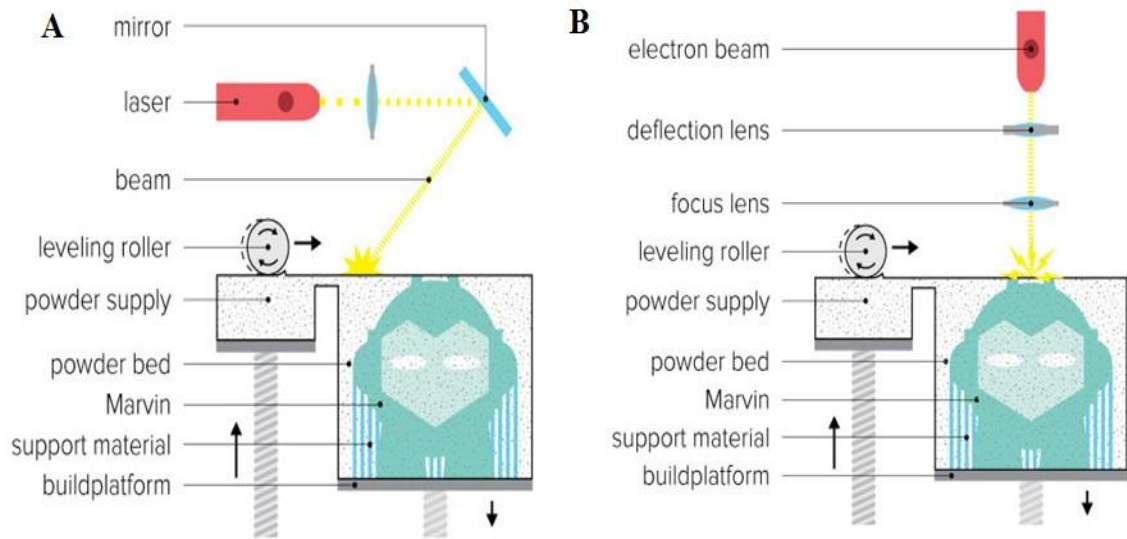
Figure 1.11 Schematic diagram of (A) SLM process, (B) EBM process [11].

1.5 Sandwich Structure

Sandwich structure consists of two relatively thin, stiff and strong faces separated by a relatively thick lightweight core as shown in Figure 1.12.
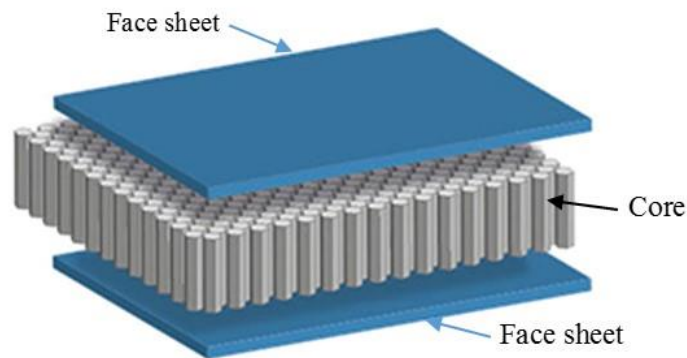
Figure 1.12 Sandwich structure [12].

The sandwich structures provide high bending stiffness and high strength-to-weight ratio and are used in aerospace, aircraft, motor vehicles, etc. The face sheets are generally

made of Kevlar, aramid and glass, while the core is made of a lattice structure (matrix material). The material selection depends on the application. The face sheet and the core are bond together with the help of epoxy resins. In this thesis work, a two-part heavy-duty epoxy resin (Loctite) was used to attach a four layered Kevlar sheet to the lattice of the hybrid structure. A low-speed impact test was performed on the 'Kevlar side' of the hybrid structure.

1.6 Computational Analysis

1.6.1 Electromagnetic Simulation Analysis

The software selection for antenna design and simulation depends mainly on the geometry of the structure and the required accuracy of the solution. Software like Computer Simulation Technology (CST) Microwave studio, HFSS, FEKO, and COMSOL Multiphysics are generally used for antenna simulations. The numerical methods used to solve Computational Electromagnetic simulation Method (CEM) are integral-equation solvers, differential equation (DE) solvers, asymptotic techniques, and other numerical methods. These software use methods like moment of methods (MOM), multilevel fast multipole method (MLFMM), finite-difference time-domain (FDTD), finite-element-method (FEM), transmission-line-matrix (TLM) methods, physical optics (PO), geometric optics (GO) and uniform theory of diffraction (UTD) for solving the EM simulation as shown in Figure 1.13 [13].

In this thesis work, HFSS is used for simulation. HFSS uses the numerical method called finite element method. In this technique, the structure is subdivided into many

smaller subsections called finite elements which are tetrahedral and are collectively named as mesh.
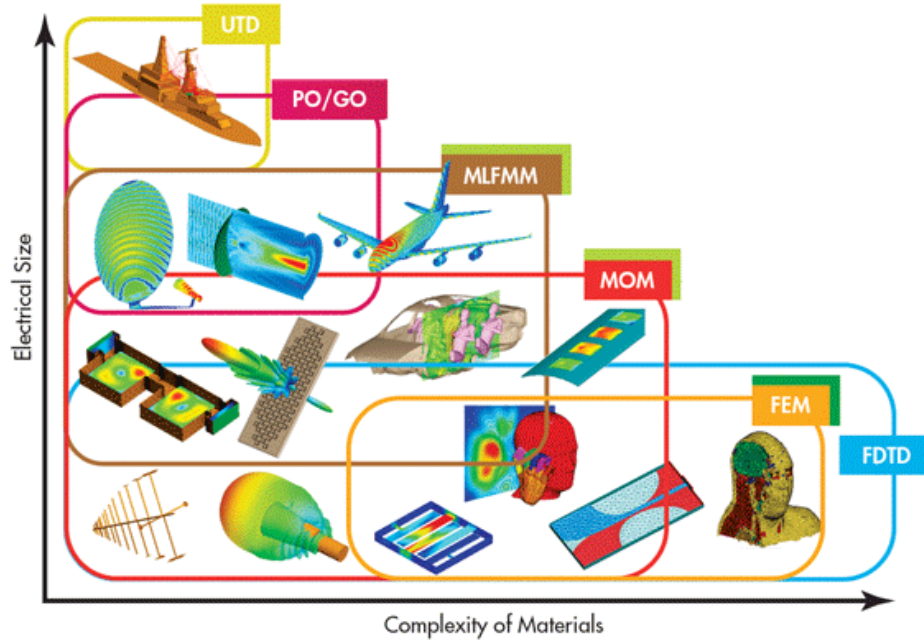
Figure 1.13 Multiple methods for effective EM simulation [13].

A solution for these fields within the finite elements is found. The Maxwell's equations are satisfied across inter-element boundaries because these fields are interrelated, which yields a field solution for the entire original structure. The generalized S-matrix is determined with the help of this field solution as shown in Figure 1.14 [14].
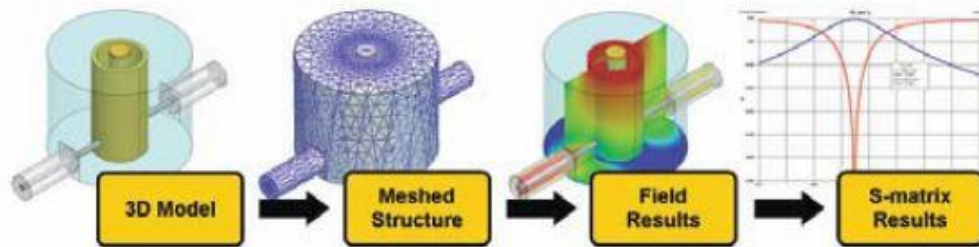
Figure 1.14 Schematic diagram of HFSS simulation [14].

HFSS simulation incorporates a volume that consists of both electric and magnetic fields. These volumes include conducting materials as well as the dielectric materials, including air, that surround the conductors. HFSS utilizes an iterative field solution process, which runs the simulation until the correct field solution is obtained. This iterative process is the key to the highly accurate results that HFSS provides. In brief, there are six main steps to create and solve a proper HFSS simulation.

1. *Creating a model/geometry*: The model can either be created in the 3D modeler window or can be imported from the CAD software such as SolidWorks, Pro/E or AutoCAD.

2. *Assign boundaries*: Assigning of the boundary conditions depends on the type of electromagnetic model (open or a closed) or to simplify the electromagnetic or geometric complexity of the electromagnetic model.

3. *Assign excitations*: There are seven types of excitations in HFSS: Current Sources, Wave Ports, Lumped Ports, Floquet Ports, Incident Fields, Voltage Sources and Magnetic Bias Source. All excitation types provide field information, but only the Wave port, Lumped Port, and Floquet port provide S-parameters.

4. *Set up the solution*: In this step, the following parameters are defined: solution frequency, convergence criteria, number of adaptive passes, a frequency band, a solution type and a frequency sweep methodology.

5. *Solve*: The model is ready to be analyzed, once the above steps have been completed. The time required for the analysis is highly dependent on the model geometry, solution frequency, and available computer resources.

6. *Post-process the results*: This step involves generating the S-parameter of the model or plotting the field in and around the structure, etc.

1.6.2 Finite Element Analysis (FEA)

The finite element analysis is the simulation process that utilizes a numerical technique called Finite Element Method (FEM) to solve the engineering and physics problems. It is used to reduce the experimental cost and time. In this analysis, the user has the design freedom which allows him to optimize the design components to develop better products faster. The finite element analysis solves the mathematical equations of the problems like structural or fluid behavior and thermal transport, etc. Most of these problems are represented using Partial Differential Equations (PDE) [15]. These partial differential equations (PDEs) are solved in order to compute the significant quantities of a structure (like stress, strain, etc.). The model is divided into small quantities called as mesh elements, which are generally solved under the given load and boundary conditions. FEA gives an approximate solution to the problem. The results of a simulation based on the FEA method are usually depicted via a color scale that shows for example the pressure distribution over the object as shown in Figure 1.15.
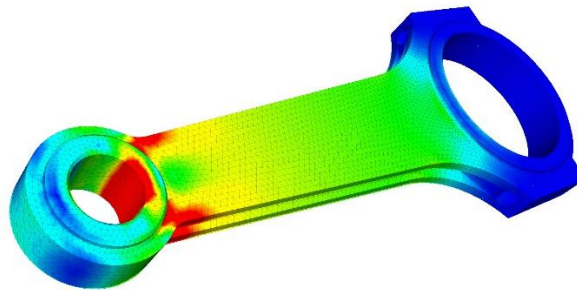
Figure 1.15 ABAQUS (FEA) simulation of a piston rod [15].

Abaqus CAE is one of the commercial FEA software available in the market. Abaqus software is generally used to solve large and complex structures. It consists of two different types of analyses namely, Abaqus/Explicit and Abaqus/Standard. Abaqus/Explicit is generally used to simulate transient dynamic events such as consumer electronics drop testing, automotive crashworthiness, and ballistic impact. This analysis solves highly discontinuous problems like impact testing with adding any additional degrees of freedom. Abaqus/Explicit effectively handles the nonlinear behavior such as rolling of hot metal and slow crushing of energy absorbing devices [16].

The results obtained in Explicit can be used as starting conditions for the continuation of the problem in Standard analysis and vice-versa. By leveraging this integration, Abaqus/Explicit can be applied to the continuation of the analysis where high-speed, nonlinear response dominates the solution and while Abaqus/Standard can be applied to the portion of the analysis such as static, low-speed dynamic models.

1.7 Aim and Scope

The aim of this research is to design an electrically and a structurally effective antenna structure for future mobile communication, the next generation of structural surface technology and automobile applications. Structurally effective materials with high electrical loss must not lower the antenna efficiency in order to obtain both high electrical and structural performances in the hybrid structure. The design procedure is focused on tuning the operational frequency of the antenna, while having mechanical robustness, so that the electrical components undergo minimal damage under low-velocity impact loads.

The following steps are the orderly representation of the research performed.

- First, three samples with dimensions of 50 mm x 50 mm x 5 mm were created at three different machine preset fill densities using a 3D printer-LulzBot.

- 3D X-ray microscopy was performed to observe the actual fill density in the printed samples. Microstrip patch antennas were created on the printed ABS samples and tested for resonating frequencies.

- Two specific models were considered: (1) Model A – Three Layer Model and (2) Model B – One Layer Model. In either case a microstrip patch antenna model was created using ANSYS-HFSS on the substrate that mimics the experimental patch.

- A hybrid structure was designed with a lattice part of thickness 15 mm and a solid part of thickness 5 mm, to add structural strength to the above structure.

- A low-velocity impact test was performed on the both sides fabricated hybrid structure and a numerical analysis with ABAQUS Explicit was performed to match the experimental results.

- HFSS simulations were performed on the hybrid structure with antenna embedded at the interface of lattice and solid parts before and after impact test and the effect of the impact load on the resonant frequency of the antenna was calculated.

CHAPTER 2 : LITERATURE REVIEW

2.1 Overview

In this chapter, a literature survey on the topics related to the current research is presented. It deals with past work done on 3D printing of dielectric substrates and also microstrip patch antennas. Different materials used by researchers for 3D printing of the dielectric substrates are discussed. A brief research is done on how ANSYS-HFSS was utilized for performing the EM finite element analysis by different researchers. The basic design rules for patch antennas are also mentioned. Previous work done on developing electro-mechanical structures is reviewed and is related to the current research work. This chapter gives more clear understanding on the development of hybrid structure.

2.2 3D Printed Dielectrics and Dielectric Materials

By adapting 3D printing techniques to fabricate the dielectric materials, it allows the engineers to customize the substrate dimensions as in conformal antenna applications. 3D printing can be used to create multi-material objects in a single process by eliminating the assembly process. Zhang et al [17] demonstrated the combination of nontoxic material polylactic acid (PLA) and air to spawn novel dielectric substrates. The dielectric properties of materials such as permittivity and loss factor have been tailored with different air to PLA percentage ratios. In their research, six dielectric substrate samples were printed with two different patterns by varying the infill densities as shown in

Figure 2.1. They presented the feasibility of creating low loss dielectric substrates with various relative permittivities and loss tangent values using 3D printing. It is concluded that these highly customizable dielectric substrates will improve the flexibility of antenna design and EM related applications.
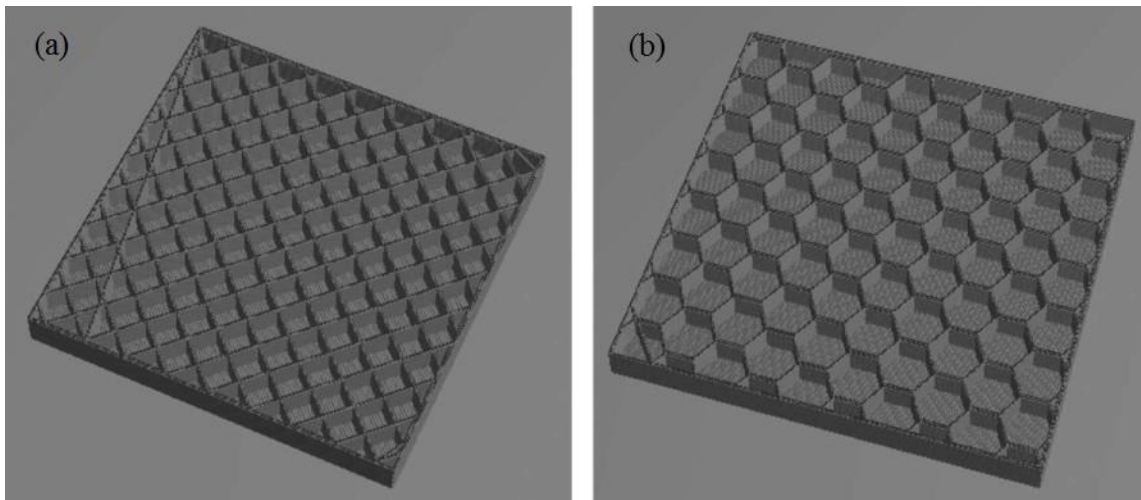
Figure 2.1 CAD sketch of different internal structures of 3D printed dielectric substrates, (a) Waffle infill and (b) Honeycomb infill [17].

A similar research was done by Tummala, et al [18] on 3D printed porous dielectric substrates for RF applications. In their research work, ABS substrates of dimensions 50 mm x 50 mm x 5 mm were printed at three machine preset fill densities. 3D X-ray images were taken for a lucid description of the internal features of printed substrates. The volume fraction calculations from the image analysis for those samples exhibited a minor deviation from the preset fill density value. Microstrip patch antennas were printed on substrates and RF characterization was performed. They concluded that their results clearly demonstrated the ability to control the dielectric constant of printed substrates based on prescribed fill density. Results obtained from their research are important to design and characterize dielectric substrates with desired anisotropy.

After reviewing the above research works, in this thesis ABS material was chosen for 3D printing the substrates with predefined fill densities.

2.3 HFSS – Finite Element Analysis

Most of the researchers use HFSS for the EM finite element analysis of the microstrip patch antenna. In the year 2001, Yang. F, et al, designed a novel single-patch wide-band microstrip antenna: the E-shaped patch antenna (Figure 2.2). They validated their design concept by demonstrating two examples with 21.3% and 32.3% bandwidths [19]. The resonating frequency, radiation pattern and the directivity were designed with help of HFSS software. They measured the S_{11} parameter on network analyzer and compared the results with the numerical data given by HFSS.
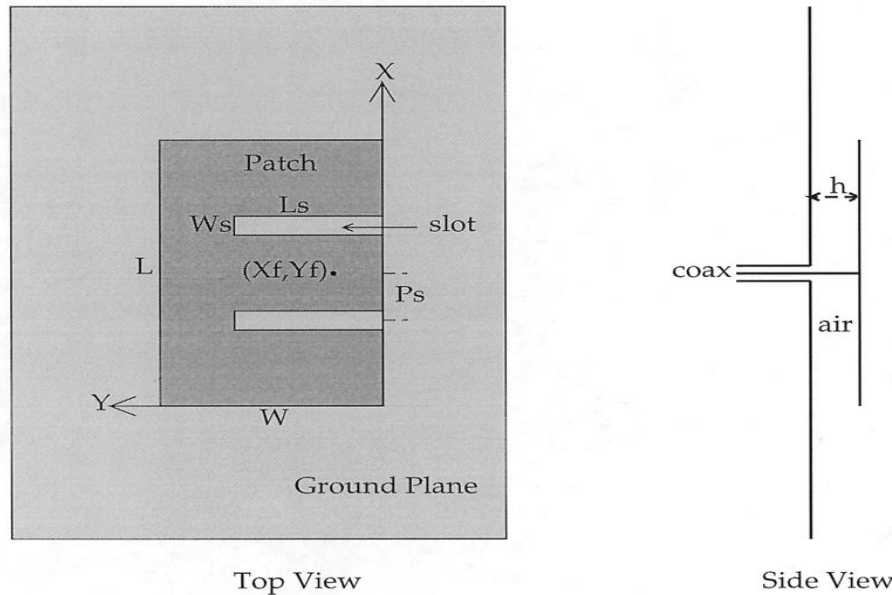
Figure 2.2 Geometry of a wide band E-shaped patch antenna with two parallel slots [19].

A similar research was performed by Ahmed Khidre, et al, [20] to achieve a circularly polarized probe-fed single-layer microstrip-patch antenna with wideband axial ratio. Investigations of the effect of various dimensions of the antenna were carried out via

HFSS parametric analysis. The performance of the fabricated antenna was measured and compared with simulation results. They concluded that their proposed design (Figure 2.3) was feasible for the implementation of a reconfigurable antenna with switchable left-hand circularly polarized/right-hand circularly polarized operation.
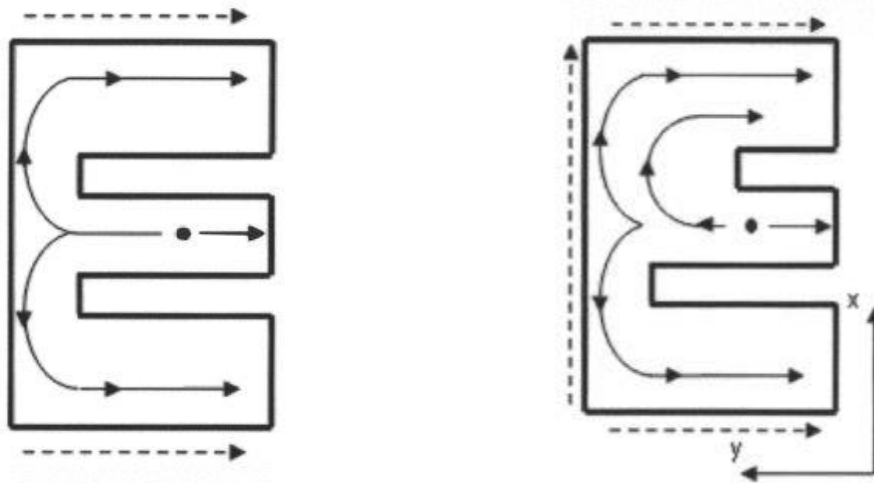
Figure 2.3 The current flow across the E-patch polarized: (a) linear, (b) circular [20].

The anisotropy in the printed substrate with air gap was analyzed by Yamina, et al, [21] while researching on antennas using neural networks. In antenna modeling, the resonant frequency of the rectangular microstrip antenna with or without air gap printed on isotropic or uniaxial anisotropic substrate was calculated with numerical analysis in HFSS. The relative dielectric permittivity ε_r, was replaced with tensor as uniaxial anisotropy was taken into account. Electromagnetic knowledge combined with artificial neural network was proposed to solve the data generation problem. Effective dielectric constant and height were determined for the case of isotropic substrate with air gap and uniaxial anisotropic substrate without air gap, respectively. These parameters were used in Green's function of isotropic substrate without air gap to calibrate the results.

- For the case of isotropic substrate with air gap, the effective dielectric constant ε_{re} and the effective dielectric thickness H_e are given by:

$$\varepsilon_{re} = \frac{\varepsilon_r * (H_a + H_d)}{(H_d + H_a * \varepsilon_r)} \tag{1}$$

$$H_e = H_d + H_a * \sqrt{\varepsilon_r} \tag{2}$$
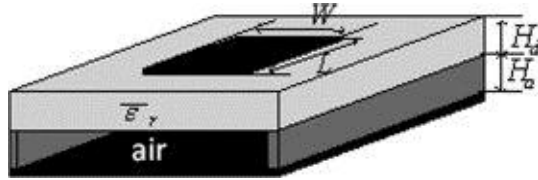
Figure 2.4 Rectangular patch antenna with air gap of thickness Ha printed on anisotropic substrate of thickness Hd [21].

- For the case of uniaxial anisotropic substrate without air gap, ε_{re} and H_e are given by

$$\varepsilon_{re} = \varepsilon_{rz} \tag{3}$$

$$H_e = H_d * \sqrt{\frac{\varepsilon_{rx}}{\varepsilon_{rz}}} \tag{4}$$

A comparison between the commercial software packages for microstrip antenna analysis was done by D. M. Pozar, et al [22]. In their study, four different antenna geometries were compared. The input impedance of each antenna was measured at a set of 9 to 15 frequencies near resonance, and were compared with results obtained from the five commercial CAD packages (Ensemble, PCAAD, Momentum, HFSS, IE3D), using their own respective custom analysis codes. In order to obtain a good measure of accuracy, they

defined an error criteria at each frequency between the measured and calculated reflection coefficients.

Based on the above research, HFSS was used as the simulation software for analyzing the anisotropy in the printed dielectric substrate. The anisotropy was analyzed in the planar and thickness directions.

2.4 Microstrip Patch Antenna

The microstrip antenna was first proposed by Deschamps [23] in 1953. Later, in 1955 (France), a patent was issued in the names of Gutton and Baissinot [24]. It took about 20 years for the practical antennas to be developed by Howell and Munson [25]. The development of microstrip antennas was accelerated by the availability of good substrates with loss tangent and attractive thermal and mechanical properties, improved photolithographic techniques, and better theoretical models. Since then, an effective and extensive research was performed in developing the microstrip antennas (array). The research aimed at exploiting their numerous advantages such as light weight, low volume, low cost, conformal configuration, compatibility with integrated circuits.

The idea of microstrip patch antennas arose from utilizing printed circuit technology for the radiating elements of an electronic system. The basic patch shapes are shown in Figure 2.5. Feeding is usually done by a coaxial probe or a stripline and can be directly connected to the patch, or coupled through an aperture, or proximity coupled to the patch [26]. These are illustrated in Figure 2.6.
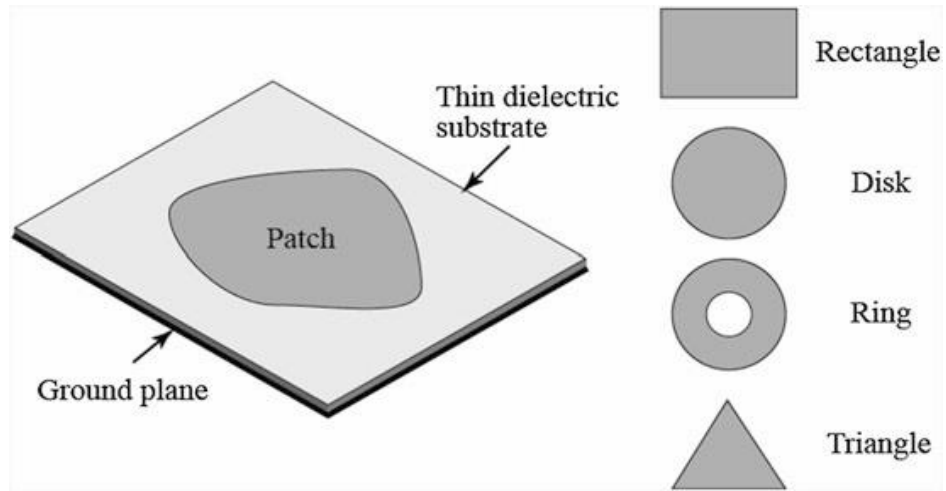
Figure 2.5 The elemental structures of a microstrip patch antenna [26].
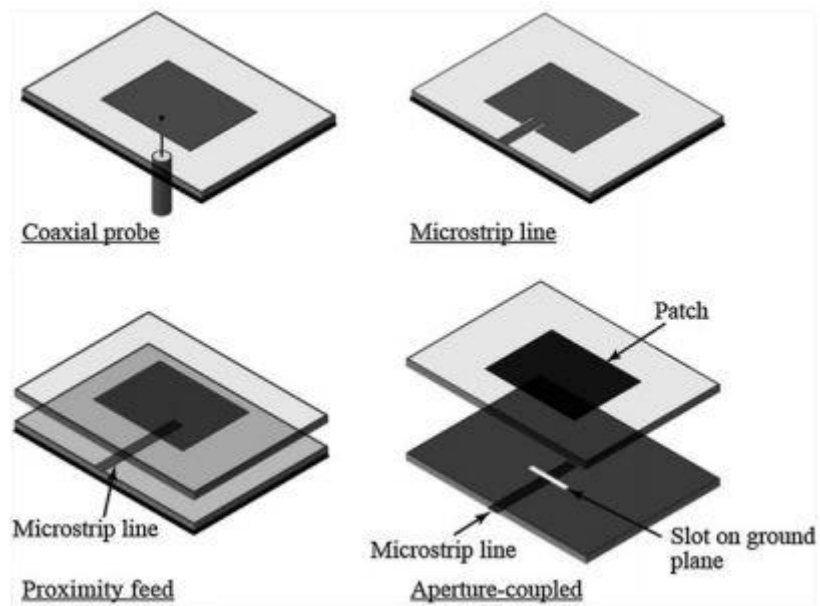
Figure 2.6 Common feeding techniques of microstrip patch antenna [26].

Two approaches can be utilized to calibrate the performance characteristics of microstrip patch antennas. One approach is to devise a physical model based on a number of simplifying assumptions; the other approach is to solve Maxwell's equations subject to

the boundary conditions. For the coaxial feed microstrip patch antenna shown in Figure 2.6(a), known as the cavity model [27], has been developed to calibrate the performance characteristics of the antenna. It is based on a number of simplifying assumptions which are valid for thin substrates. These assumptions allow the fields between the patch and the ground plane to be analytically determined. The radiation and impedance characteristics of the basic microstrip patch antenna geometry can be calculated from the above assumptions. The Maxwell's equations that are solved without relying on the thin substrate assumption are also called as full-wave. A method used to solve the Maxwell's equation treats the currents on the antenna structure to be the unknowns for solving the structure. The integral equations obtained for the unknown currents that satisfy the boundary and excitation conditions are solved by a numerical method called as the moment method [28]. In the last 20 years, many commercial FEA software were built based on full-wave methods. These software played an important role in the rapid development of microstrip antenna research. They have become indispensable tools in the design of these antennas.

The effective permittivity of the cavity will change, if an air gap is introduced between the substrate and the ground plane in a microstrip patch antenna. The calculated effective permittivity value can be used to tune the resonant frequency [29]. The geometry of a microstrip patch antenna with an air gap is shown in Figure 2.7.
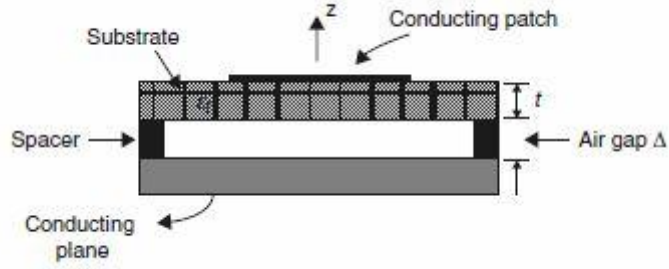
Figure 2.7 Microstrip patch antenna with an air gap [26].

A cavity was considered under the conducting patch. This structure was made of two layers: an air region of thickness 'Δ' and a substrate of thickness t. The effective permittivity of the cavity is smaller when compared to the structure with no air gap. As a result, there will be an increase in the resonant frequencies of the various modes. Since, the effective permittivity is inversely proportional to the Δ, it tends toward the free-space value of unity as Δ → ∞ and it can be inferred that the resonant frequencies can be tuned by adjusting the air gap with Δ. As bandwidth is related to the resonant frequency, it will also increase partly due to the increase in the height of the dielectric medium and partly because the effective permittivity is smaller [29]. It was noted that substrate and etching tolerances were compensated by adjusting Δ. A heuristic derivation of the effective permittivity and the resonant frequency of the two-layer cavity was derived by considering the capacitance of a capacitor with two dielectric layers, as shown in Figure 2.8. The overall capacitance is calculated as the two capacitors are in series:

$$C = \frac{\varepsilon_1 * \varepsilon_2 * A}{\varepsilon_1 * d_2 + \varepsilon_2 * d_1} = \frac{\varepsilon_{eff} * A}{d_1 + d_2} \tag{5}$$

Where,

$$\tag{6}$$

27

$$\varepsilon_{eff} = \frac{\varepsilon_1 * \varepsilon_2 * (d_1 + d_2)}{\varepsilon_1 * d_2 + \varepsilon_2 * d_1}$$
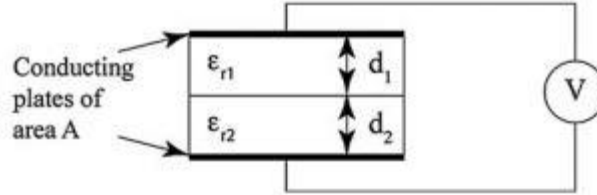
Figure 2.8 A capacitor with two dielectrics layers [26].

The disadvantage of applying the adjustable air gap method to coaxially fed patches is that, every time the air gap width is changed, the coaxial probe has to be de-soldered and re-soldered to the patch. So, in this thesis project, instead of adding an airgap, infill density is varied, so that there is no need for the coaxial probe to be de-soldered and re-soldered.

2.5 Basic Design Rules for Patch Antennas

For a microstrip configuration the guided wavelength of an EM wave in isotropic medium is defined as [30],

$$\lambda_g = \frac{c}{f * \sqrt{\varepsilon_{eff}}} \tag{7}$$

Where, $c = 3 * 10^8$ m/s, f is the frequency in Hz.

The effective permittivity, ε_{eff} of the substrate is given by,

$$\varepsilon_{eff} = \frac{\varepsilon_r + 1}{2} + \frac{\varepsilon_r - 1}{2} * \frac{1}{\sqrt{1 + \frac{12d}{W}}} \tag{8}$$

28

Where, ε_r is the dielectric constant of the material, d is the thickness, and W is the width of the patch antenna.

If the material is not uniform, as in the 3D printed structures, ε_r will not be considered as equivalent dielectric constant in the thickness direction. For a particular test system and patch antenna dimensions d, W, λ_g are constant. Thus, the equations (7) and (8) can be combined and written as,

$$\frac{1}{f^2} = C_1 * \varepsilon_r + C_2 \tag{9}$$

Where, C_1 and C_2 are constants and depend upon the wavelength, thickness, and antenna width. It is clear from equation (9) that inverse of the square of the resonant frequency varies linearly with relative permittivity of substrates.

2.6 Multi-functional AM Structures

At present, the AM technologies are confined to a minimal number of materials in a given fabrication. However, the recent research started focusing on developing sophisticated AM methodologies with process interruption capabilities including (1) inserting electronic sensor components into specific cavities within fabricated structures [31, 32, 33], (2) dispensing widely dissimilar materials for fabricating composite materials that have good thermal and electrical conductivity [34, 35, 36] and (3) embedding solid conductors within thermoplastic polymer substrates through ultrasonic or thermal energy in order to provide high performance electrical interconnect. By combining these technologies together, complex functional electronic and electromechanical systems are being fabricated in an automated manner [37]. By introducing micromachining and laser

ablation capabilities in the current FDM technology, substrates with enhanced dielectric and mechanical properties can be fabricated while simultaneously providing the required dimensional accuracies. An additional benefit of thermoplastics, as opposed to thermosetting photopolymers that do not remelt, Thermoplastics have the ability to thermally embed solid wire conductors into the substrate without affecting planarization.

David, et al, [37] utilized FDM process enhanced by complementary subtractive technologies (micromachining and laser ablation) to fabricate a 3D electronic substrate that can be used for aerospace applications. Figure 2.9 represents the steps for producing the 3D-printed CubeSat module using FDM and conductive inks.

build substrate with FDM   machine channels and cavities for circuitry   dispense conductive ink

place electronic components   join traces and electronic components   cure conductive inks
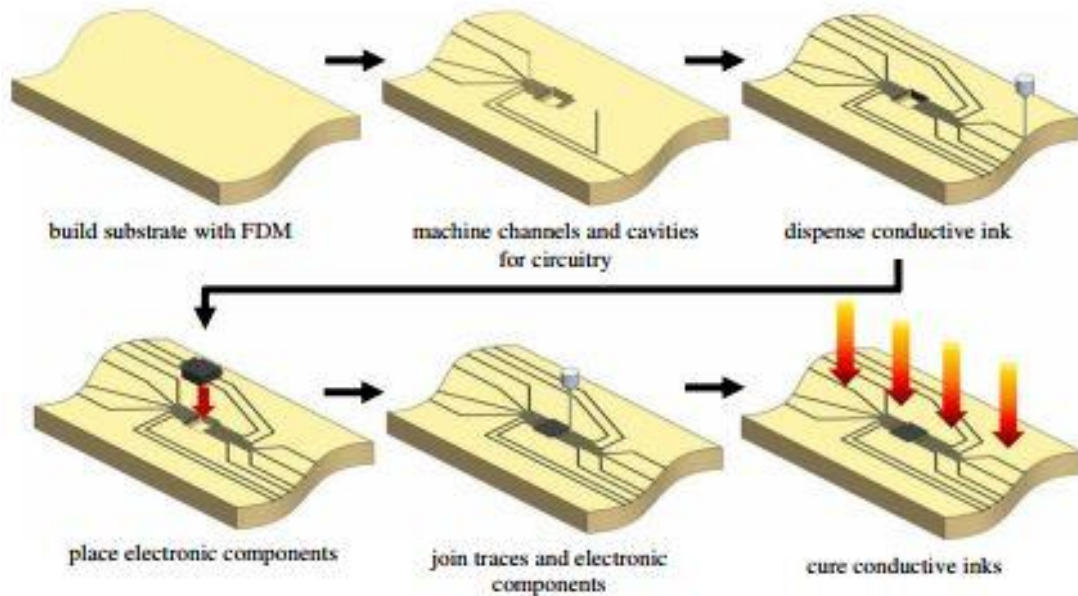
Figure 2.9 Steps followed for fabricating the 3D-printed CubeSat module utilizing FDM and conductive inks [37].

In this thesis work, the cellular lattice in hybrid structure gives a good mechanical strength and the solid part of the hybrid structure with preset fill density acts a good dielectric, resulting in a good electro-mechanical structure.

2.7 Low-Speed Impact Test

The Low-velocity impact test performed by the previous researchers was directed in observing the load-deflection curves [38, 39, 40, 41]. Correlation of load fluctuations to visible damage size, deflection quantity, crack length, delaminated area could be made [42] and [43]. The quasi-static loading tests give the same size, shape, and location of damage for a given transverse load as low velocity impact tests do.

Farooq et al. [44] explored low-velocity impact test on 24-Ply carbon fiber-reinforced composite structure. They used two types of the impactors: round and flat nose impactors. The impact test was carried out using INSTRON™ 9250HV where clamped boundary conditions was used to hold the specimens. There were two guide bars to align the impactor directly down into the specimen and the height was adjusted so that the impactor can hit the specimen with different velocities (1.5-5 m/s). The energy level can be adjusted by adding some weights to the machine. To predict the damage area, the specimens of both flat and round nose impactors were C-scanned. The round nose impactor showed almost steady behavior and there was no elastic energy. In contrast, the flat nose impactor showed that the energy level has substantially changed. The impactors were compared by plotting the load-displacement curves. They developed a numerical analysis using commercial software ABAQUS™/Explicit dynamics to compare the results to those specimens of experimental work. Finally, a MATLAB code was used to predict the failure with numerically integrated in-plane stresses.

a) Flat nose   **b) Round nose**
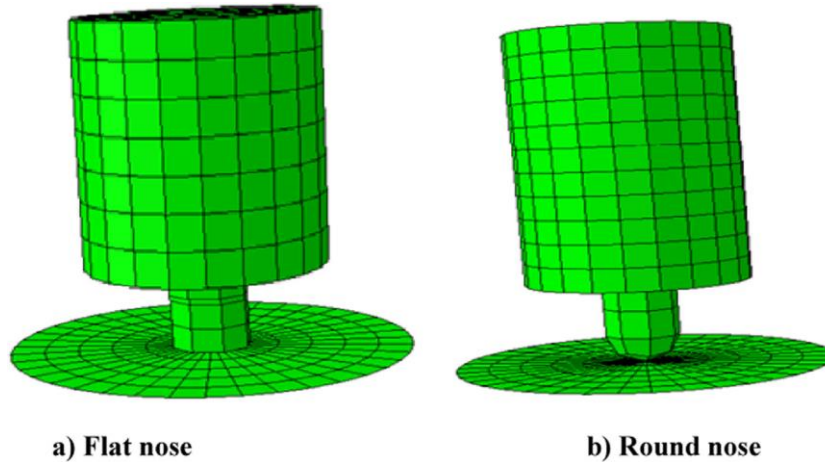
Figure 2.10 FEA impact models: (a) Flat (b) Round nose impactors [44].

Analytical and numerical models were suggested for prediction of impact damage initiation and growth during quasi-static response. Delfosse [45] compared impacts on fibrous composites by hemispherical shaped impactors that had the same incident energy over a range of velocities for conical, hemispherical and blunt nosed projectiles. Nyman et al [46] predicted the progressive failure in composite laminated laminates. Experimental and numerical investigations of low velocity impact on laminated composites were carried out in [47] and [48].
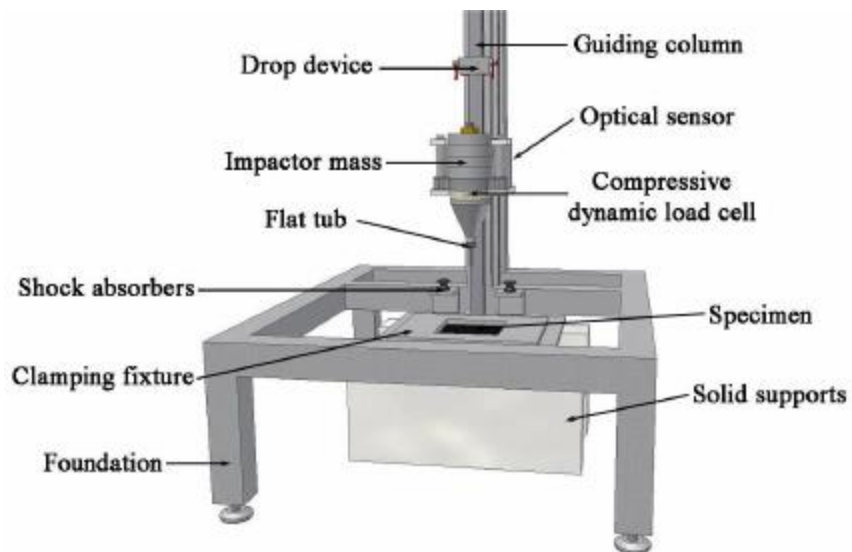
Figure 2.11 Schematic Diagram of a low-velocity impact tester [49].

St-Pierre et al. performed a low-speed impact test on Y-frame and corrugated sandwich beams [50]. A core and face sheets of 0.3 mm thickness were made from AISI 304 SS. They used two boundary conditions on the sandwich beam: simply supported and clamped boundary conditions, as shown in Figure 2.12. In the simply-supported boundary condition, the projectile weight was 2 Kg, whereas in the clamped boundary condition, the projectile weight was 3 Kg because more energy level was required in the clamped boundary condition than in the simply supported boundary condition. Transparent tube was used to guide the cylindrical impactor to the sandwich beam. The height of impact was 1.3 m. They attached a piezoelectric load cell onto the roller to calculate the transferred load to the sandwich beam. To plot load-displacement curve, a high speed camera was used to find the deflection of the roller. An FEA model was developed to compare the results with experimental data.
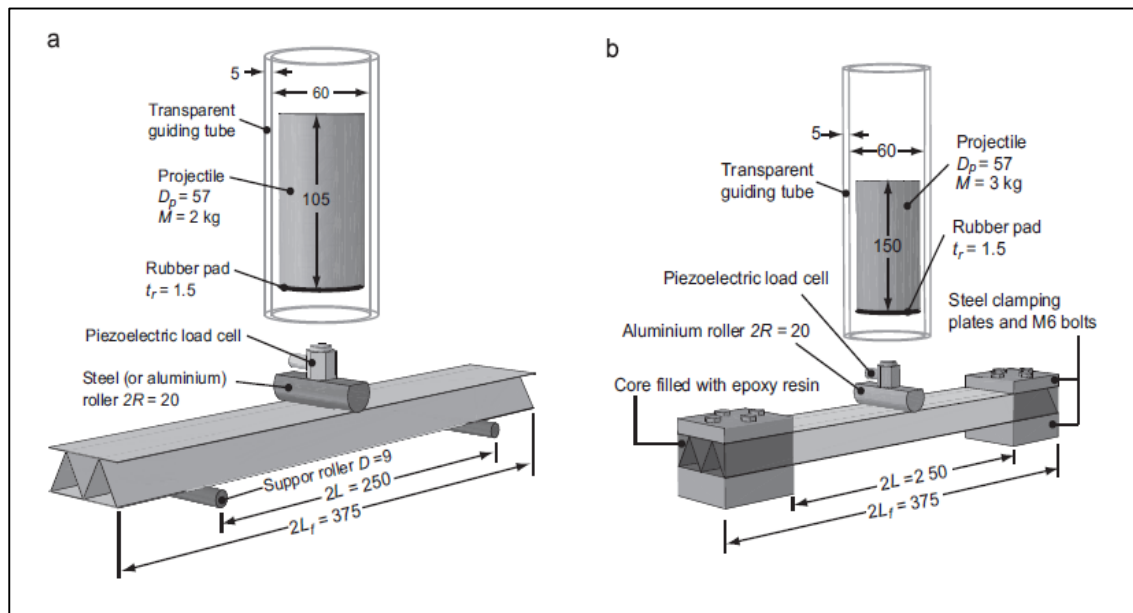
Figure 2.12 Boundary conditions of the impact test [50].

CHAPTER 3 : SAMPLE DESIGN AND FABRICATION

3.1 Overview

In this chapter, the design of the lattice core structure and the substrate for microstrip patch antenna are discussed. SolidWorks©, a Computer Aided Design (CAD) software, is used to design the lattice of the hybrid structure. The 3D printers used for fabricating the specimens are mentioned. The fabrication of Kevlar face sheets used for impact testing is also explained in detail.

3.2 Substrate Preparation for Patch Antenna

The most common 3D printing technology, Fused Deposition Modeling (FDM) is utilized to vary the physical properties of substrate like printing pattern, layer height, printing speed and infill density. Three different substrates with dimensions of 50 mm x 50 mm x 5 mm and fill densities of 25%, 50%, 75% were fabricated by using an extrusion based LulzBot TAZ-5 printer [51].
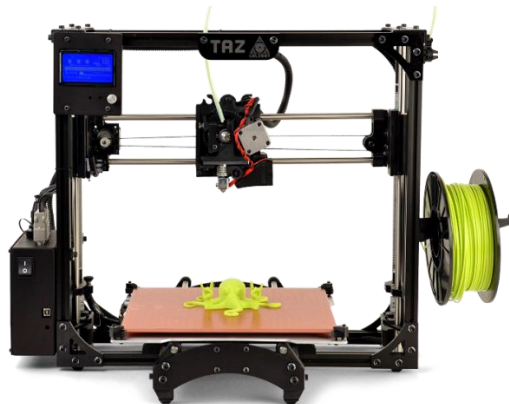
Figure 3.1 LulzBot TAZ 5 – an FDM 3D printer [55].

The infill pattern shows outer wall, inner wall and a grid infill pattern with lines in both diagonal directions per layer (Figure 3.2). FDM deposits a molten filament of ABS in a crisscross manner resulting in direction dependent or anisotropic material properties [52]. In this practicability, computer-aided design (CAD) software SolidWorks was used to create a 3D model as shown in Figure 3.3.
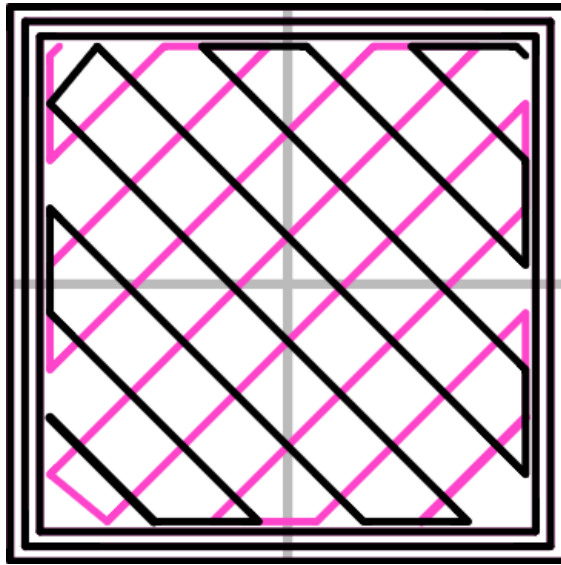
Figure 3.2 Infill pattern shows a grid with lines in two diagonal directions per layer.
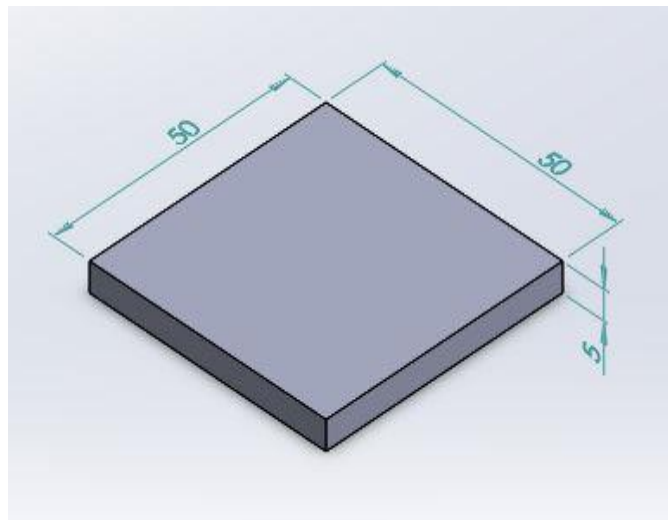
Figure 3.3 3D CAD model of patch antenna substrate.

Also, SolidWorks software was utilized to prepare Stereo lithography file format (.STL) that stores the surface geometry information of the model for printing. CURA slicing software [53] was used to convert the 3D .STL model into 2D model by slicing it horizontally to form thin sections, which represent the 3D model when piled one upon other. STL file is processed in the software and FDM printer starts slicing the model mathematically for the build process. In this process, three samples with same dimensions and at various fill densities were fabricated. Other printer parameters that were kept fixed for all samples are shown in Table 1.

Table 1: Basic and advanced printer settings used to create samples

Parameter	Value
Layer height (mm)	0.1
Shell thickness (mm)	0.7
Bottom/Top fill thickness (mm)	0.6
Print speed (mm/s)	40
Printing temperature (ºC)	245
Bed temperature (ºC)	110
Retraction Speed (mm/s)	25
Retraction Distance (mm)	1.5
Initial Layer thickness(mm)	0.3
Initial Layer line width (%)	100
Dual Extrusion overlap (mm)	0.15

3.3 Design and Fabrication of Hybrid Structure.

The hybrid structure comprising of a cellular lattice of thickness 15 mm and a solid cuboid of thickness 5 mm, collectively of dimensions 50 mm x 50 mm x 20 mm are designed in SolidWorks CAD software. BCC lattice structure configuration was considered for developing the hybrid structure. The dimensions of a single unit cell are 5

mm x 5 mm 5 mm and the diameter of the truss elements is 1 mm. The unit cell is multiplied by ten times in both x and y direction by using a feature called 'linear pattern', resulting to form a square of 100 unit cells. This array of unit cells is multiplied by three times in z-direction to form a cuboid comprising 300 unit cells. On the top surface of this lattice structure, a square of dimensions 50 mm x 50 mm is base extruded to 5 mm. This process is shown in Figure 3.4 (a) Unit cell, (b) 10 x 10 unit cell array, (c) 10 x 10 x 3 unit cell array
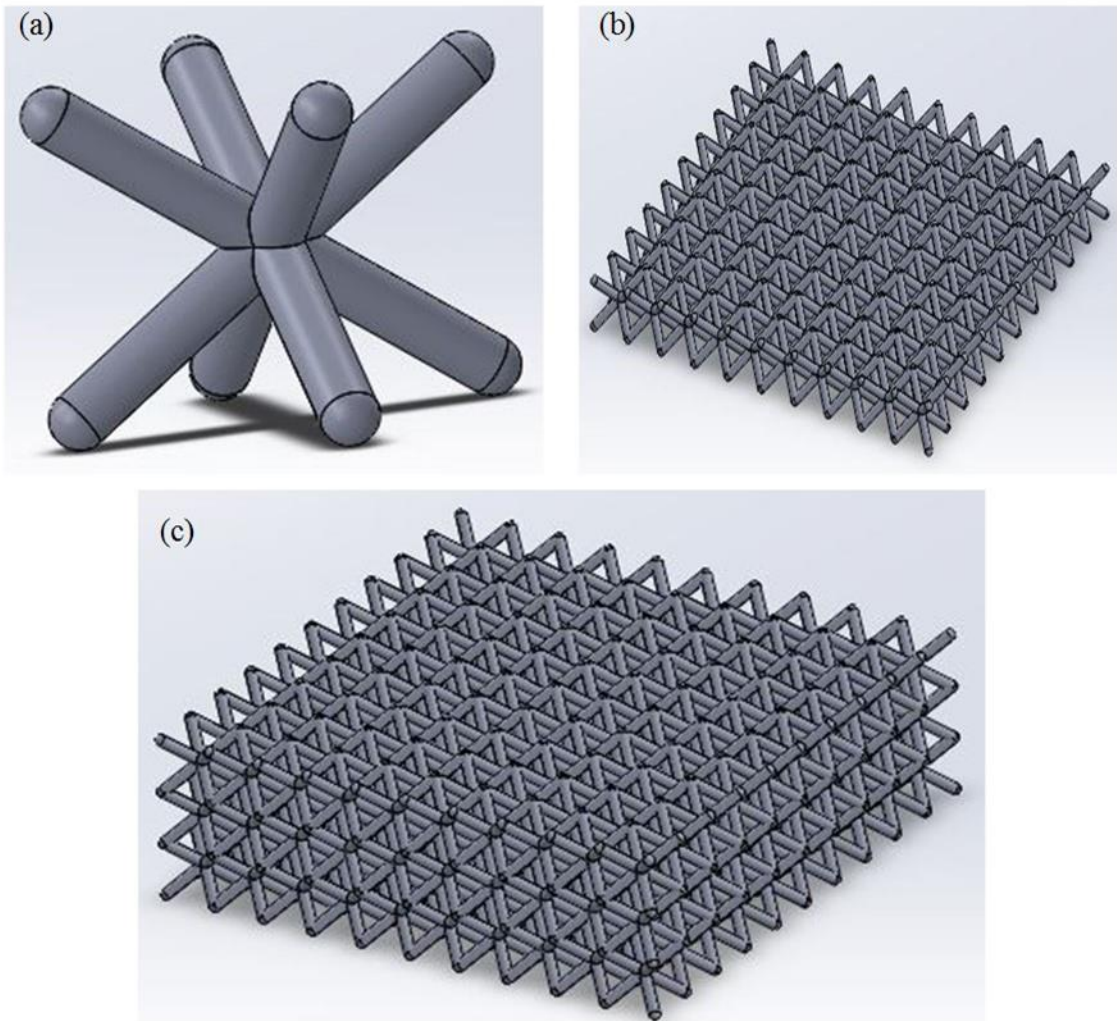
Figure 3.4 (a) Unit cell, (b) 10 x 10 unit cell array, (c) 10 x 10 x 3 unit cell array

The strut diameter was measured after fabrication and was found to be 1.1 mm. The BCC unit cell was studied and developed by many researchers. Shen et al studied the performance of the BCC unit cell [54]. Based on the information gathered from the previous researches, the BCC unit was chosen for building the lattice of hybrid structure. Figure 3.5 shows the isometric view and side view of the hybrid structure. The dimensions of the hybrid structure were derived from the ASTM Standard D7136/D7136M-15. Three specimens were fabricated to eliminate the uncertainties in printing and experimenting procedures.
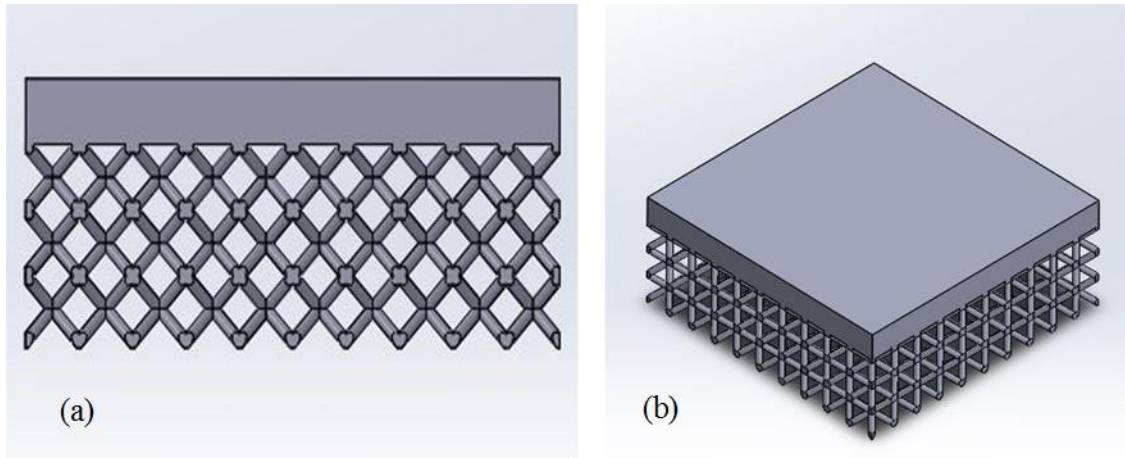
Figure 3.5 3D CAD model of Hybrid structure (a) Side view, (b) Isometric view.

Two 3D printers have been used for this research purpose. For printing the dielectric substrates, LulzBot TAZ 5 was used and for printing the hybrid structure Stratasys uPrint SE plus (Figure 3.6) was used. LulzBot printer doesn't requires support material to build the structures whereas Stratasys printer utilizes a support material called SR-30 to print the structures. The printer settings of LulzBot were discussed above section. The layer thickness capability of the Stratasys printer is 0.33 mm. It works on FDM based technology. The printing area is of 200 mm x 200 mm x 150 mm. The temperature of the printing head is maintained at 300 °C, and the base envelope is maintained at 77 °C. These

are user default settings, so we cannot modify them, unlike in LulzBot, the printer settings can be varied. When compared to each other in precision and surface finish, Stratasys printer has the upper hand on LulzBot printer. Stratasys printer takes about 5 hours to print the hybrid structure.

An ivory-colored production-grade thermoplastic (ABSplus-P430) model material is used by this printer. The printer uses a software called CatalystEX to process the .STL file. The interface is really simple and gives the user the choice to choose an STL file containing the 3d model, choose the orientation, scale and position on the building platform, and some basic build options (layer resolution, model interior fillings and type of support structure) and it generates the data for the machine stored as a CMB-File. CatalystEX only shows the 2D footprint on the building platform and statistics about the amount of building material and time needed. This is basically a slice viewer, displaying toolpaths of one build-slice. Using the home, end, page-up and page-down keys, one can conveniently step through all slices. This software has three options for building the support material: basic, smart, surround.

After the fabrication process, there will be some support material left in the model that should be cleaned (Figure 3.8). The amount of support material depends on the geometry of the model. For some models, the support material can be removed with help of some tools provided by the 3D printer manufacturer. In case of cellular structures, the support material lies inside the lattice, so a chemical solvent should be used to remove the support material. The chemical solvent suggested by the 3D printer manufacturer was P400-SC Waterworks soluble concentrate. This is an alkaline cleaning agent that contains Sodium hydroxide, Sodium carbonate, Sodium lauryl sulfate, Sodium metasilicate. It is

mixed with water in 1:10 ratio and poured in a support cleaning apparatus (SCA-1200) that is shown in Figure 3.7. The chemical solution is maintained at 70 °C for about 4 hours for the support material to dissolve in the solution. It is recommended to use safety glasses and gloves while using the chemical bath. After removing the material, the model should be washed with water at room temperature.

Figure 3.6 Stratasys uPrint SE plus 3D printer.

Figure 3.7 Support cleaning apparatus [58].
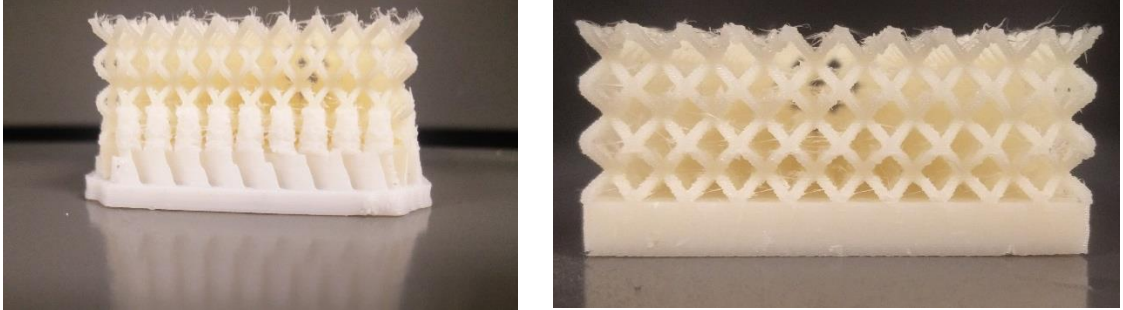
Figure 3.8 Hybrid structure (a) with support (b) without support material.

By observing the hybrid structure after the removal of support material, it was inferred that same unit cells along the edges of the structure were fractured before testing. This occurred in one of the three samples that were printed.

3.4 Kevlar Face Sheet

The hybrid structure is attached with a Kevlar face sheet at the bottom. Four layers of Hexcel Composites' K285-38"-F161 Kevlar Fabric is laminated together to form the face sheet. Kev. 49 1140 Fiber with a crowfoot weave is the type of Kevlar used. These Kevlar fabrics are pre-impregnated with a laminate-grade epoxy resin in order to reinforce the Kevlar. The mechanical properties of dry Kev. 49 at 24 °C are shown in Table 2. There are three stages in the cure cycle of the Kevlar: heat-up, hold and cool down. The hot press used for laminating the four layers of Kevlar is shown in the Figure 3.9. The four layers of Kevlar were lubricated with silicon oil and were encased in an aluminum foil. A pressure of 3 metric tons for a period of three hours at 220 °C was maintained. After three hours at 220 °C, the Kevlar was maintained at the same pressure until it reached the room temperature. Finally, the face sheet with dimensions of 105 mm x 105 mm x 0.86 mm was fabricated and cut into pieces of required dimensions so that they can be attached to the lattice of hybrid structure. Figure 3.10 shows the Kevlar fabrication process.

41

Table 2: Mechanical properties of Kevlar fabric at 24 °C [56].

Kevlar	Tensile Modulus (GPa)	Tensile Strength (MPa)	Compression Strength (MPa)	Resin Fracture Toughness (MPa.$\sqrt{m}$)
Kev. 49	26.5	428	308	0.433
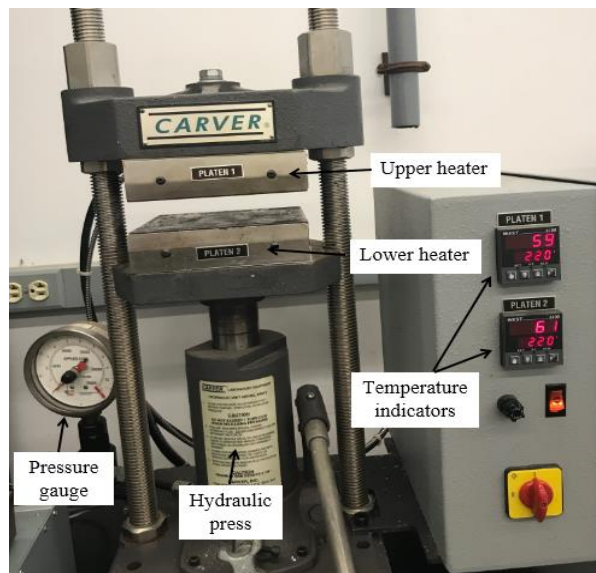
Figure 3.9 Carver Hot Press [60].
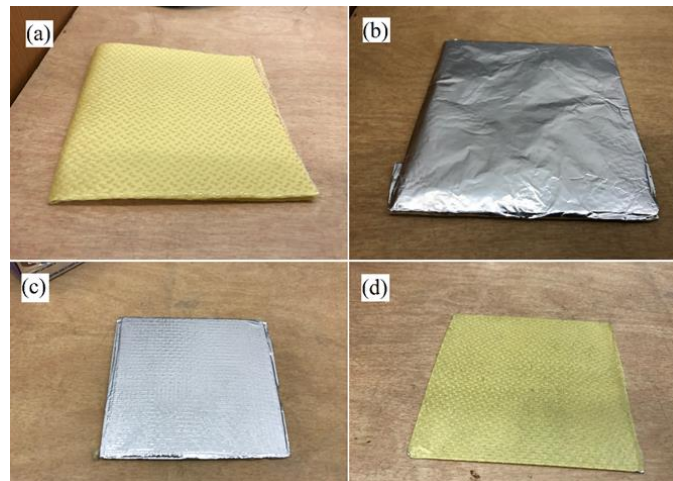
Figure 3.10 Four ply Kevlar (a) Before compression, (b) Covered with Aluminum foil, (c) After compression with aluminum foil (d) Final Kevlar face sheet.

3.5 Attaching Kevlar Sheet to the Hybrid Structure

The hybrid lattice structure after fabrication, was attached to the Kevlar sheet. Loctite® Heavy Duty Epoxy resin was used for adhering the face sheet. The resin consists of a hardener and a resin. These two parts are generally mixed in equal ratios. Once they are mixed an exothermic reaction tends to happen as it becomes a little hotter. Figure 3.11 shows the epoxy used in this process. The fabricated Kevlar face sheet is cut into 3 pieces of dimension 50 mm x 50 mm. A detailed procedure of attaching the face sheet is shown in the Figure 3.12. After attaching the face sheet, it is recommended to put a weight of 4-5 kg for 24 hours on the specimen for the resin to harden. The weight of the specimen is measured to be 21 grams including the face sheet and epoxy resin. When measured individually the hybrid structure and the face sheet were 18.4 grams and 2.5 grams respectively.

Figure 3.11 Loctite® Heavy Duty Epoxy resin.
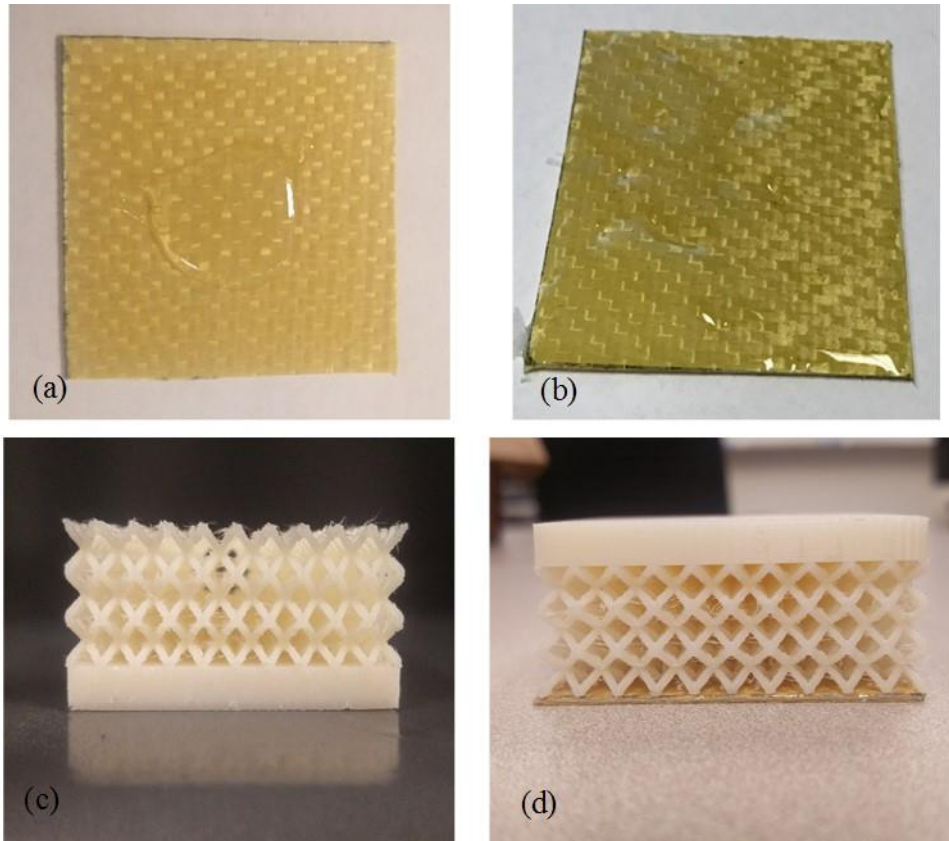
Figure 3.12 Procedure of attaching Kevlar to the hybrid structure.

CHAPTER 4 : EXPERIMENTAL CHARACTERIZATION WORK

4.1 Overview

In this chapter, the experiment performed on the dielectric samples printed on LulzBot 3D printer to determine the resonant frequency of the microstrip patch antenna is discussed. A 3D X-Ray microscopy on the dielectric samples is examined. The low-velocity impact test performed on hybrid structure is explained in detail. The process exercised for observing the amount of indentation in the impact test samples is also demonstrated.

4.2 3D X-Ray Microscopy

A thorough and complete experimental approach is required for understanding the internal lattice structures of the 3D printed ABS substrates. The goal of this is to identify or visualize small scale basic changes by using a nondestructive testing apparatus. The arrangements obtained from the test will help find permittivity in three orthogonal directions. Also, the actual solid volume fraction is required for calculating equivalent permittivity to be used as an input to ANSYS-HFSS simulation. Conventional imaging tools such as optical magnifying lens, scanning electron microscopy (SEM) or transmission electron microscopy (TEM) provides images of regions considerably smaller than specimen. Therefore, a 3D X-ray microscope by Zeiss is utilized in this case, which can nondestructively characterize the diverse microstructure designs at a chosen level of high resolution (down to 700nm) and sought field of view. 3D X-ray microscope (XRM) reveals

45

the details of the structure and provides imaging solution in three dimensions. This also preserves the integrity of the samples for further investigation. The deep penetration of X-rays can eliminate or minimize the need for extensive sample preparation. Full X-ray tomography also does not alter the sample and hence does not suffer from mechanical sectioning artifacts and non-cubic voxels. The result is superior visualization and quantification of 3D microstructures. The principle operation of the microscope depends upon the standard computed tomography by reconstructing the 2D slices of XRM image to supply 3D image. The microscope provides advanced imaging solution in 3D by accomplished high contrast and high-resolution imaging even for large sample [58, 59]. Figure 4.1 illustrates the application examples for 3D X-ray imaging.
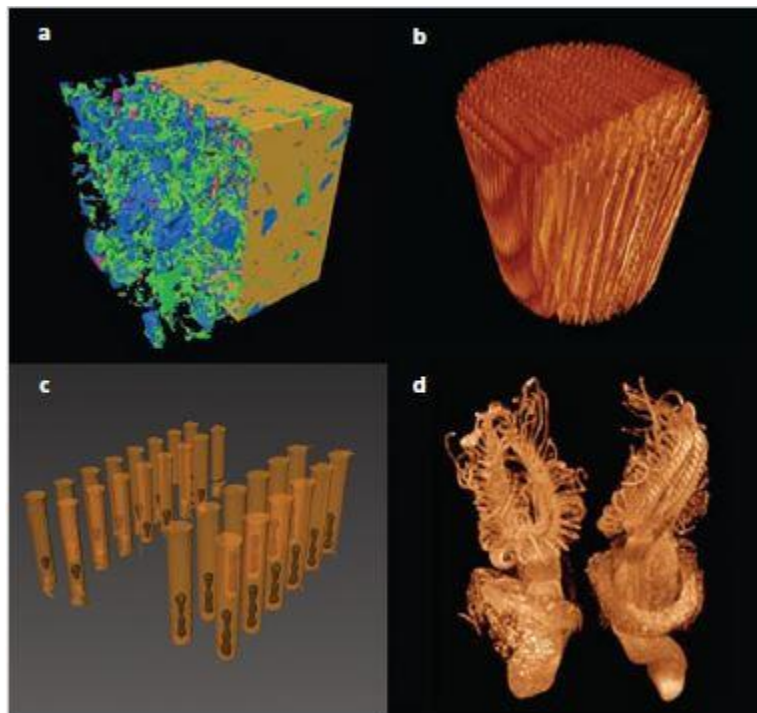
Figure 4.1 application examples for 3D X-ray imaging [60].

Figure 4.1 depicts [a] Geology – Segmented sandstone that is composed of grain matrix (yellow), clay (blue), pore (green), and high Z materials (red). [b] Materials Science

– Wood tomography visualization of fiber microstructure and can be used to determine hygroscopic properties. [c] Semiconductor industry – Tomography of through Silicon Vias (TSVs) detects voids formed. [d] Life Sciences – Freshwater bryozoans Cristatellamucedo stained with PTA (Image provided by Brian Metscher and Gerd Müller of the Department of Theoretical Biology, University of Vienna).

Figure 4.2 ZEISS Xradia 520 Versa X-ray microscope [61].

The microscope shown in Figure 4.2 has been used for the experiment. In this technique, microscopic analysis was done by using x-ray microscopy that has usable magnification level 1X, considering the additively manufactured size and most significantly to get large view and detect their inner structure. 3D X-ray images were captured for every one of the three ABS fill densities of 25%, 50% and 75% with pixel sizes of 16.6, 15.3 and 16.6 respectively. Advanced image segmentation was performed to isolate solid and pore volumes. Then the percentage of solid volume fraction from a

representative volume element (RVE) was calculated. The solid volume fraction was subtracted from 100% to calculate pore fraction.

The dimensions of RVE for the 75%, 50%, and 25% samples were 6.7 mm x 1.5 mm x 2.1 mm, 5.4 mm x 2.4 mm x 2.1 mm, and 6.4 mm x 3.9 mm x 2.1 mm, respectively as shown in Figure 4.3. In this case, only the core regions were considered to measure actual porosity because the printer preset fill densities are observed to influence the core region as seen from the x-ray images in Figure 4.3. To calculate volume fraction, advanced image analysis was performed using a combination of computational tools.
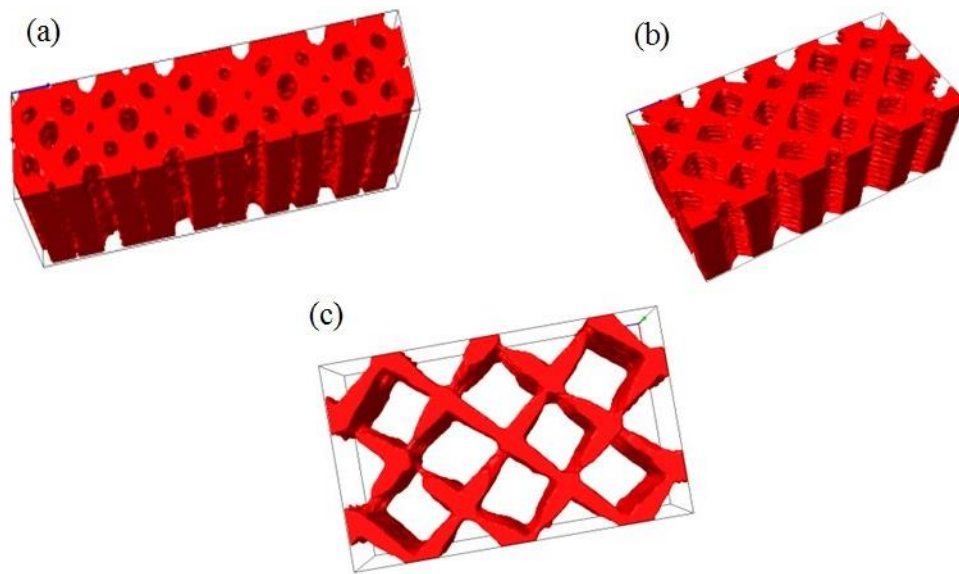
Figure 4.3 Image analysis performed to calculate the actual volume fractions LulzBot printed samples, (a) Fill density 75%. RVE dimension: 6.7 mm x 1.4 mm x 2.1 mm, (b) Fill density 50%. RVE dimension: 5.4 mm x 2.4 mm x 2.1 mm, (c) Fill density 25%. RVE dimension 6.4 mm x 3.9 mm x 2.1 mm [18].

First, XMReconstructor software by Zeiss converts acquired tomography projections into DICOMM format that was then imported in Simpleware ScanIP software. Segmentation algorithm in ScanIP isolates solid and pore volumes in the 3D image (Figure

4.3). A representative volume element (RVE) was selected based on the repeat pattern of the segmented image for each specimen type, and the percentage of solid volume fraction were calculated.

4.3 Antenna Preparation

The concentration of the RF characterization was discussed and compared in term of the impact of material porosity change on the resonant frequency of patch antenna. Patch antenna configuration and design was considered [62, 63]. Three patch antennas were constructed on 3D printed dielectric material substrate as shown in Figure 4.3. Every patch antenna was designed utilizing a similar size square copper tape material with dimension and feed location as shown in Figure 4.4(a). On the opposite side of the patch antenna, a ground plane was designed utilizing a large piece of copper tape. Also, a drill press was used to create a hole for the feed conductor.
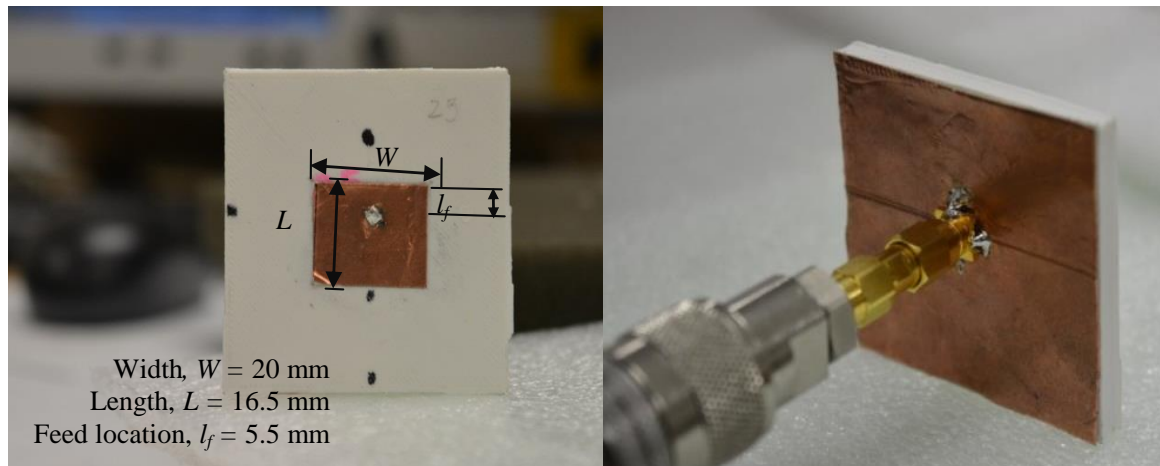
Figure 4.4 Patch antennas created on printed samples. (a) Front view displaying the feed location; (b) Back view of an antenna attached with copper-tape ground plane.

Copper around the hole on the ground plane was removed completely to prevent electrical short between the feed conductor and the ground plane. The back surface of the

antenna was covered with copper tape as shown in Figure 4.4(b). A 50 ohm SMA connector was utilized to connect the patch antenna with the internal pin of the SMA. The outer conductor of the SMA was soldered to the ground plane. Vector Network Analyzer (VNA) was then calibrated using open, short, and 50-ohm load over a broad frequency range of interest [64]. S-parameter (S11) data was measured for each antenna sample by connecting to (VNA). The resonant frequency was identified from the S11 vs. frequency data. The magnitude of the S11 will be marked minimum at the resonant frequency.

4.4 Low-Velocity Impact Testing

The low velocity impact testing was performed on the hybrid structure. The impact test machine used for experiment was developed by Andrew Turner [65, 66]. It was constructed according to ASTM Standard D7136/D7136M-15 as shown in Figure 4.5. The machine consists of two guide bars to make sure that the impactor hits the specimen at the center. A hemisphere base impactor drops from a height of 0.6492 m. The impactor hits the specimen with a velocity of 3.5678 m/s. In this research, the energy level of the impactor assembly was adjusted to 14.05 Joule. The mass of the impactor assembly was 2.208 kg. The energy level was calculated from the kinetic energy (KE) of the impactor just before it hits the specimen.

$$KE = \frac{1}{2} * m * v^2 \tag{10}$$

Where, m is the mass of the impactor assembly and v is the velocity of the impactor. Assuming that the friction of the guide bars is negligible, the velocity can be calculated from potential energy (PE) and kinetic energy. According to the conservation of energy,

energy can neither be created nor destroyed; energy can only be transferred or changed from one form to another. That means KE is equal to PE.

$$PE = m * g * h \tag{11}$$

Where, g is the acceleration due to gravity and h is the height from which impactor drops. By equating eq. (10) and eq. (11), the velocity is given by,

$$v = \sqrt{2 * g * h} \tag{12}$$
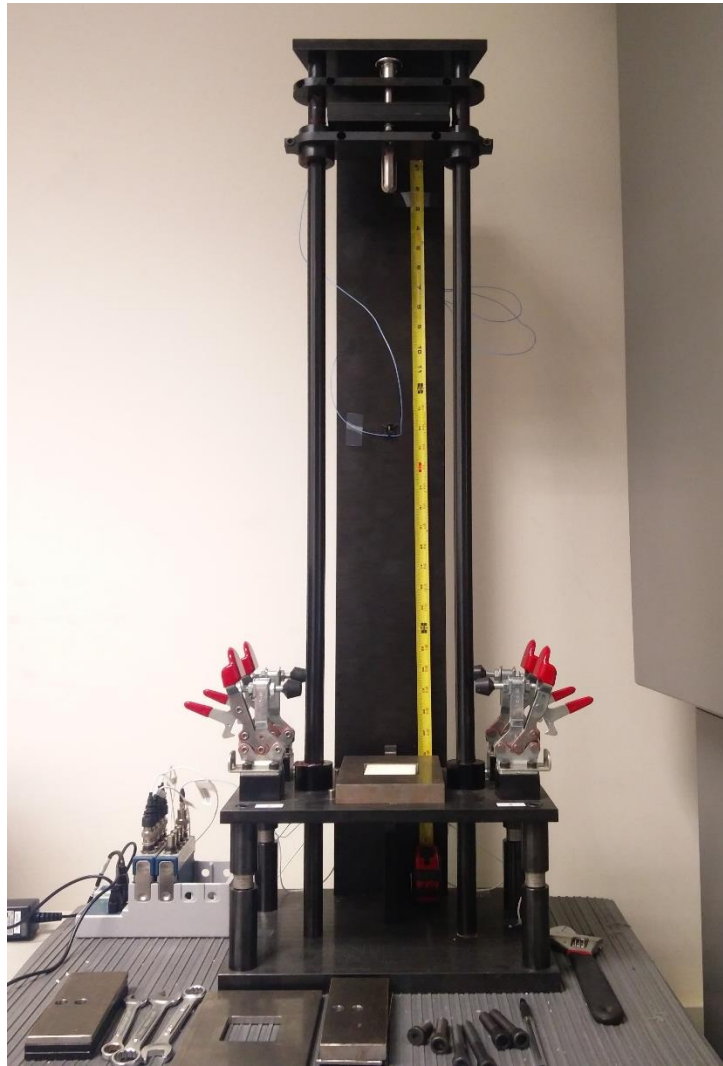
Figure 4.5 Low-velocity impact test machine.

The machine in Figure 4.5 consists of four load cells (Dytran 1051V5 IEPE) which evaluate the amount of load during impact. The energy absorbed by the specimen can be evaluated with the knowledge of the amount of displacement. The displacement is calculated by integrating the acceleration twice with respect to time. The acceleration history is measured by the accelerometer sensor attached to the impactor assembly. The velocity can be measured by integrating the acceleration with respect to time.
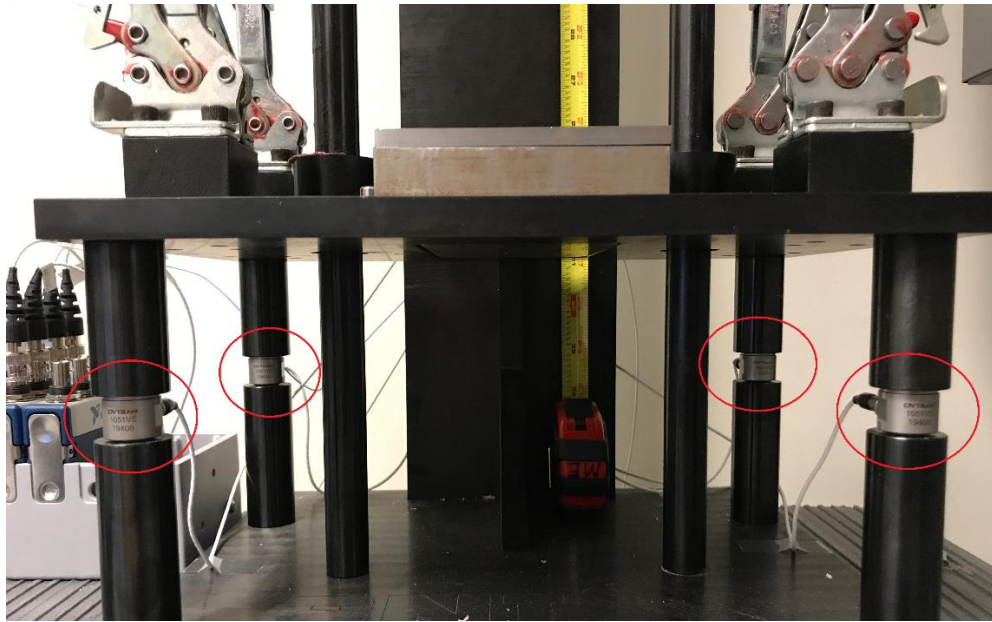
Figure 4.6 Locations of four load cells of the impact machine [61].

The experiment data was saved and post-processed using MATLAB code which was developed by Turner [66]. The MATLAB code generates six plots: load history, velocity history, displacement history, acceleration history, energy absorption history and load-displacement history. The results cannot be interpreted from the above generated graphs as the time taken for testing the specimens differs from one to another. The impact period should be visually analyzed and isolated manually in MATLAB. The impact period can be evaluated from the load and acceleration history. Usually, the testing period is about 4-5 seconds and the impact period is about 4E-3 s. The specimen undergoes elastic and

plastic deformation during the impact period. After the impact, some unit cells of the specimen collapse and some of them undergo only elastic deformation. The specimen is clamped to a body fixture using a toggle clamp as shown in the Figure 4.7(a) which is the boundary condition. The mass of the impactor can be increased by adding weights as shown in Figure 4.8.
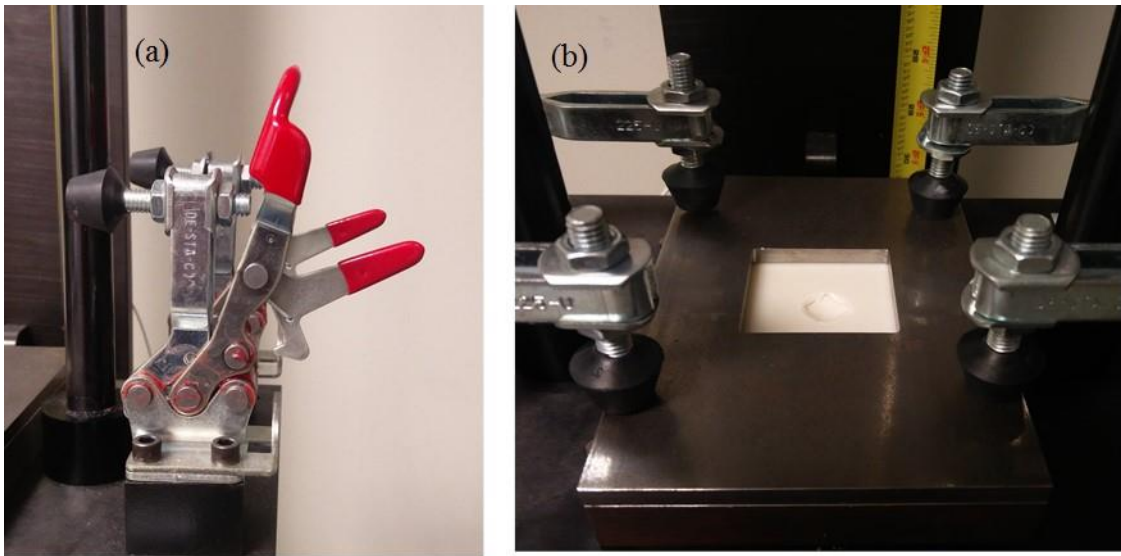
Figure 4.7 (a) The toggle clamp and (b) body fixture.
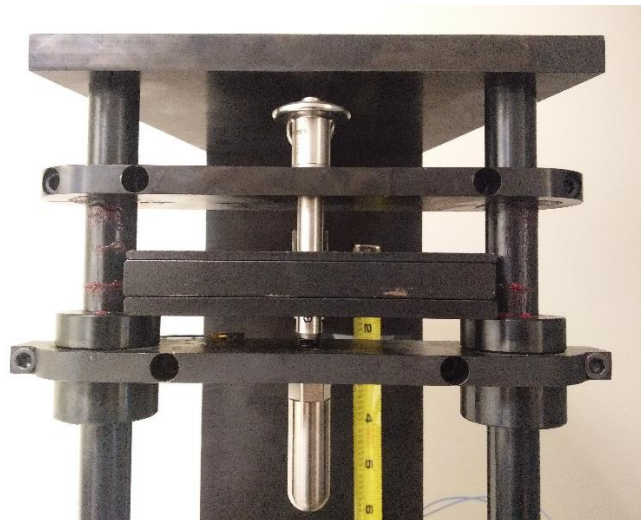
Figure 4.8 The impactor assembly of the impact machine.

4.5 Cross-sectional Analysis of Impact Tested Specimens

This experiment was performed to study the failure of the impact tested specimens, particularly, the depth of indentation. The specimens have been visually inspected for determining the indentation. An approximate estimation was done. For a better understanding, a cross-section analysis was performed. The tested specimen was embedded in a resin and then cut after the resin had hardened.

The resin used in this experiment was PARKS ultra-gloss epoxy resin (Figure 4.10(a)). This resin is made up of two parts: an activator and a resin. Equal parts of resin (Part A) and actuator (Part B) was poured into separate cups, as mixing must be one-to-one ratio. The mixing was done by pouring the Part A into Part B and then gently stirring it with a stick for six minutes to limit air bubbles from entering the mixture. The sides and bottom of the container were scraped with the stirring stick while mixing as instructed in the manual. Finally, the mixed resin and activator was poured into a new container as shown in Figure 4.9.
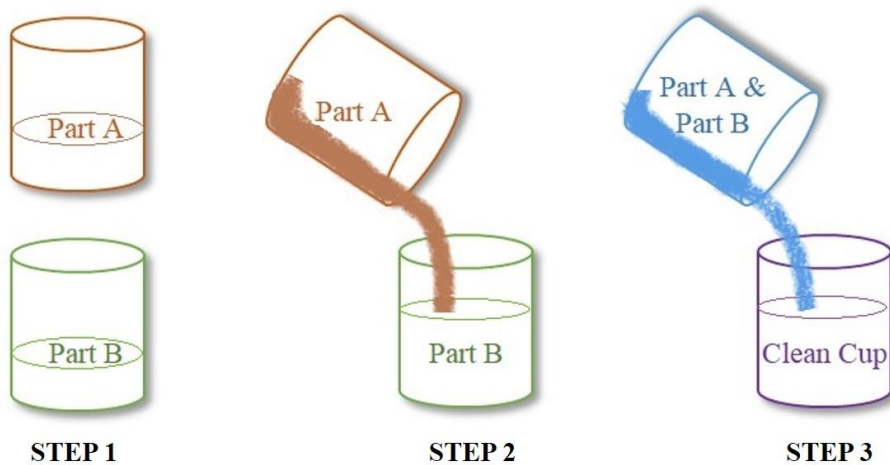
Figure 4.9 Resin mixing directions.

The impact tested specimen was put in a beaker as shown in Figure 4.10(b), and the thoroughly mixed resin was poured slowly into the beaker, so that air bubbles were not trapped in the mixture. The viscosity of the resin increases as time proceeds. Due to resin's high viscosity, it doesn't penetrate into the gaps of the lattice structure. To avoid this problem, a vacuum pump and a sealed container were used in this experiment. The beaker was placed inside the sealed container and the whole chamber's air was sucked out with help of the vacuum pump as shown in the Figure 4.11(a).

Figure 4.10 (a) Parks Resin, (b) Impact tested sample placed in a beaker.

By performing this process, most of the air bubbles present in the resin escape to the surface of the resin. The remaining bubbles were eradicated by opening the vacuum pump valve, so that the pressure created inside the chamber pushes the resin deeper into the lattice structure. An exothermic reaction occurs during the curing of the resin.
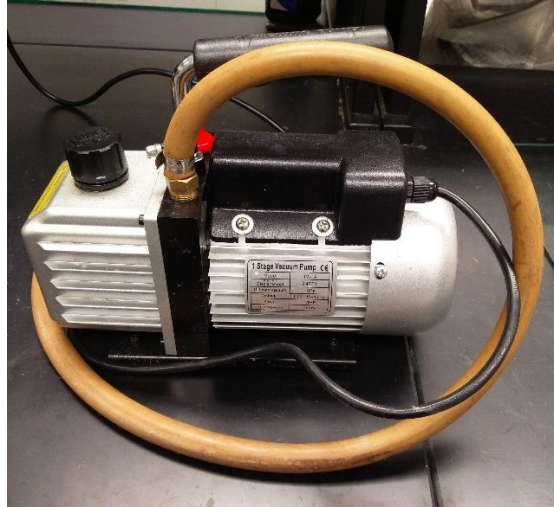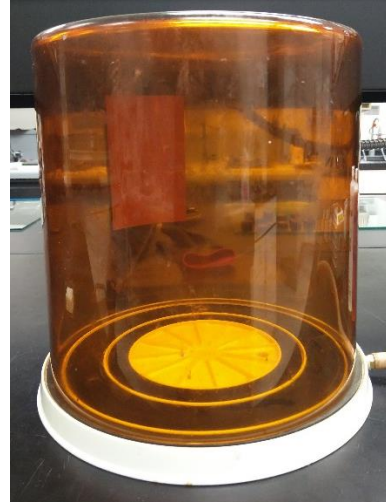
<p align="center">(a)   (b)</p>

Figure 4.11 (a) Vacuum pump, (b) Sealed container

The ideal application temperature of the resin is 70°F. The curing time of the resin is 72 hours. However, higher temperatures lower the curing times. It is important to keep the surface covered during the curing process to protect from dirt and debris. Once the resin cures, it is removed from the beaker and cut into two halves.

Figure 4.12 Specimen immersed in resin and set for curing.

CHAPTER 5 : MODELING

5.1 Overview

ANSYS-HFSS software is used to model the microstrip patch antenna by varying the dielectric permittivity of the substrate both in planar and thickness directions. In this chapter, three different models are discussed. Two models are developed to check effect of the anisotropy in the dielectric property of the substrate. The third model is developed to evaluate the best suitable position of the microstrip patch antenna in the hybrid structure. ABAQUS Explicit software is used to analyze the low-velocity impact test.

5.2 ANSYS – HFSS Modelling

HFSS is typically used to simulate electromagnetic field problems thereby avoiding repeated design iterations and prototyping [67, 68]. Material anisotropy can be defined in the software by specifying the three diagonal elements of an anisotropy tensor; however, anisotropy in relative permittivity is only considered for this study. In this analysis, three separate models were designed (a) Model A - a three-layered model of overall dimensions of 50 mm × 50 mm × 5 mm, (b) Model B – a complete solid model with same overall dimensions, (c) Model C – a hybrid structure model of overall dimensions 50 mm x 50 mm x 20 mm. For both models A and B, a rectangular patch antenna of dimension 16.5 mm × 20 mm and a ground plane of dimension 50 mm x 50 mm were created on the top and bottom surface of the model respectively. A cylinder with radius 0.7 mm and height 5 mm was formed to connect the patch and the ground plane (see Figure 5.1). Copper was

assigned as the material type to both the patch and the ground plane. A coaxial-probe excitation port was designed at the bottom of the model through which the antenna was excited. The reference plane of this port is located directly at the beginning of the radiating plane.
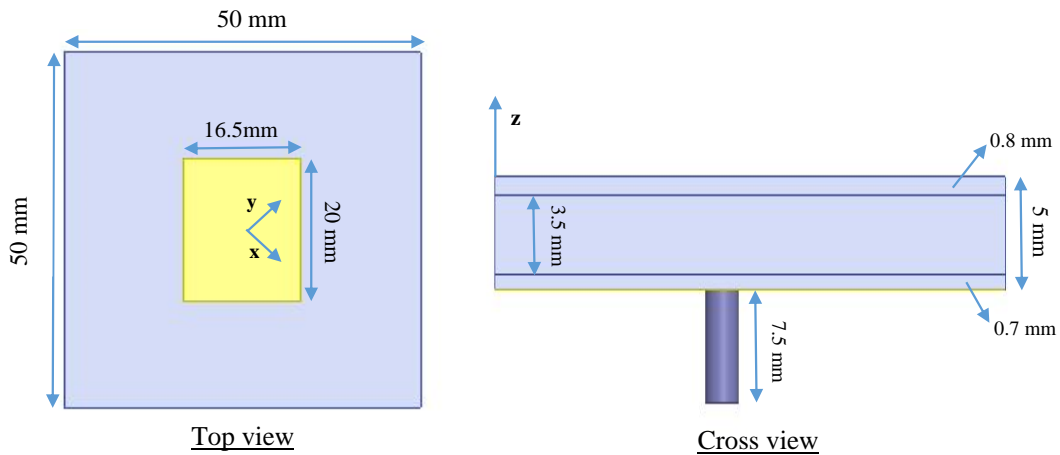
Figure 5.1 Top and Cross views of the HFSS models A and B.

In HFSS, radiation boundaries were considered so that waves were allowed to radiate infinitely far into space. HFSS absorbs the wave at the radiation boundary which is an air box in this case. The patch antenna, ground-plane, feed and excitation were modelled exactly as the measured dimensions of the experimental setup (Figure 5.2). A terminal driven solution type was used to generate the S- parameter graph to calculate the frequency of the antenna.

For all the models, x-y coordinates are rotated 45° with respect to the substrate length and width, while z coordinate is directed along thickness direction. The coordinate system is chosen in this manner to capture the directionality during printing as shown in Figure 3.2.

5.2.1 Model A – Three-Layered Substrate

After fabrication of the LulzBot specimen, they have been X-rayed to see their internal structure by using a 3D X-ray microscope. Surprisingly, from the images, it was observed that the preset fill density was only employed in the core of the specimens. In general, the preset fill density in FDM process is only employed at the substrate core creating a structure with distinct three layers as shown in Figure 5.2. Based on this observation, the substrate was divided into three layers. The top and bottom layers are the skin and the middle layer is the core of the substrate.
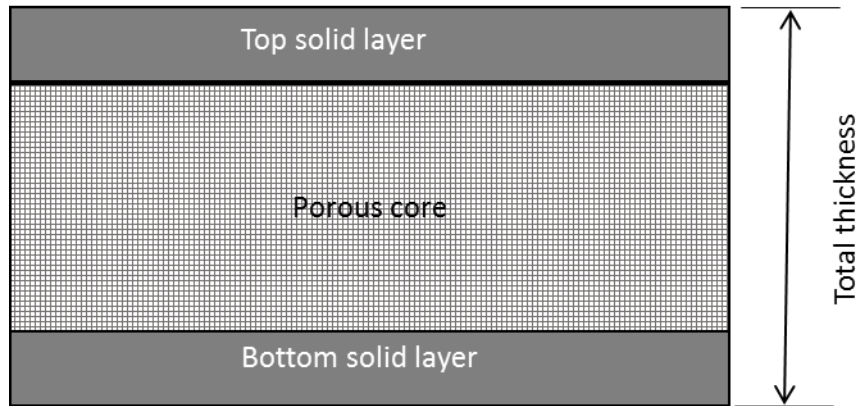
Figure 5.2 3D printed material having a three-layer sandwich construction.

Thicknesses of these layers were chosen based upon the x-ray images of the printed samples. The top and bottom layer thickness of the skin were observed to be 0.8 mm and 0.7 mm respectively, and the thickness of the core was 3.5 mm. These layers were designed in SolidWorks and saved in .IGES format, which is compatible with HFSS software. These layers were imported in to ANSYS-HFSS software to perform the antenna RF characterization. These imported layers were stacked together accordingly to form the model of overall dimensions 50 mm × 50 mm × 5 mm as shown in Figure 5.2.
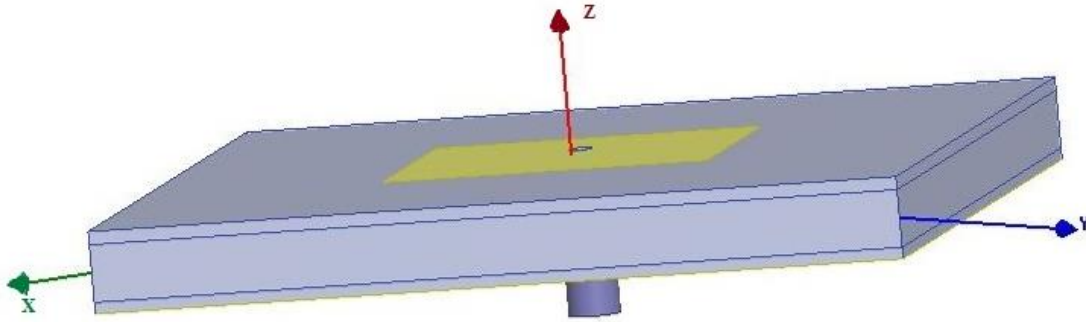
Figure 5.3 3D isometric view of the HFSS model A.

Due to the layer-by-layer fabrication of fused deposition modeling (FDM) based 3DP process, the printed dielectrics are inherently uniaxial anisotropic having different permittivity in two orthogonal directions, for example in planar and thickness directions, depending upon the toolpath [69] [70] [52]. Anisotropic dielectric constants or relative permittivity in x, y (planer) and z (thickness) directions $\varepsilon_{rx}, \varepsilon_{ry}$, and ε_{rz} were assigned for each layer. These values were calculated by using the equations (13) and (14). The ABS material properties have been assigned to the three layers. In this case, the dielectric constants were considered to be the equivalent dielectric constants by incorporating the effect of voids. Based on the results from the 3D x-ray images and computed solid volume fractions, directional dielectric constants were calculated by considering air void and solid in either parallel or series using the following equations of rule of mixture [71]. For clear understanding, an x-ray image of the core of a 25% fill density sample is shown in Figure 5.4. It is clear from the image that the voids and ABS solids are arranged in series in x and y direction while they are parallel in z direction.
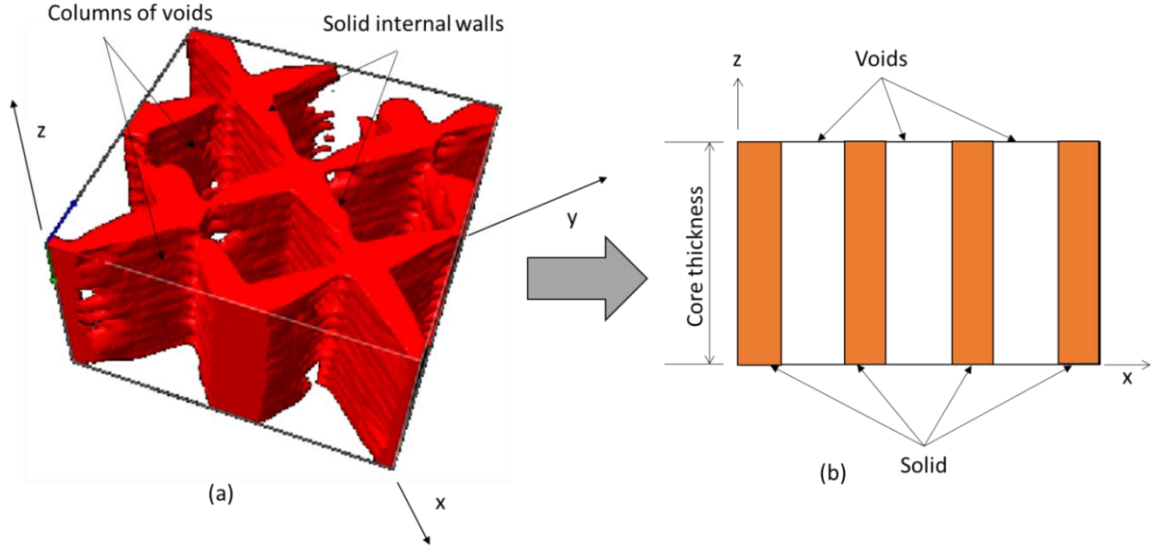
Figure 5.4 (a) Core internal structure at 25% fill density. (b) Voids and solid are in series in x and y direction while they are arranged in parallel in z direction.

$$\varepsilon_{r,eqv,parallel} = V * \varepsilon_{r,solid} + (1 - V) * \varepsilon_{r,air} \tag{13}$$

$$\frac{1}{\varepsilon_{r,eqv,series}} = \frac{V}{\varepsilon_{r,solid}} + \frac{(1 - V)}{\varepsilon_{r,air}} \tag{14}$$

Where, V = solid volume fraction of the substrate, and $\varepsilon_{r,solid}$ and $\varepsilon_{r,air}$ are the dielectric constant of solid and air, respectively. Note that, $\varepsilon_{r,air} = 1$. In the event, the air-solid arrangement was not as clear as in Figure 5.4, the equivalent dielectric constant was calculated using the equation (15). In this case, the void is considered to be distributed in solids.

$$\varepsilon_{r,eqv} = \varepsilon_{r,solid} \left\{ 1 + \frac{3(1-V)}{\frac{\varepsilon_{r,air} + 2\varepsilon_{r,solid}}{\varepsilon_{r,air} - \varepsilon_{r,solid}} - 1 + V} \right\} \tag{15}$$

It can be observed from Figure 3.2 that the motion of the print head is diagonally linear and the substrate and air are printed in series and parallel combination along the surface and thickness direction respectively. Based on this observation, x, y coordinates are chosen to be oriented at an angle of 45° with the length and width of the antenna substrate while z coordinate in the thickness direction as shown in Figures 5.1 and 5.2. For the core, the equivalent dielectric constant along the x and y directions are same due to symmetry and were calculated and using equation (14). Equation (13) was used for calculating z direction property. Since the top and bottom layers have very low porosity, their distribution is considered uniform. In this case, equation (15) was used to calculate equivalent dielectric constants in x, y, and z directions. The last column of Table 3 is the effective z direction dielectric constant of the substrate is calculated by using rules of mixture as given in equation (14). In this case, volume fraction of core is 3.5/5 or 0.7 and that of top and bottom skin is 0.3. Layering construction of printed substrates and anisotropy introduced in each layer are expected to affect antenna response [72] [17]

After assigning these dielectric tensor values to the layers, a region which was large enough for the radiation at the lower frequency (one-fourth of the wave) was created. This region was all directional with absolute offset of 35 mm. An air box was assigned as a radiation boundary. Finite conductivity was assigned to all the conducting surfaces in the model (Feed, ground plane and the connector). A solution analysis was setup with a frequency of 2.4 GHz with twenty number of passes. An interpolating frequency sweep was added with a range of 1 GHz – 10 GHz with 0.01 step size. The validation check was performed to check that all parameters were assigned.

Table 3 - The calculated equivalent series and parallel dielectric constants along the x, y, and z directions (ε_{rx}, ε_{ry} and ε_{rz})

Fill Densities	X-ray measured solid volume fraction	Dielectric constant in x(ε_{rx}) and y (ε_{ry}) direction	Dielectric constant in z (ε_{rz}) direction	Effective Dielectric constant of substrate in z (ε_{rz}) direction
Core-25%	0.335	1.22	1.40	1.56
Core-50%	0.544	1.42	1.65	1.76
Core-75%	0.753	1.69	1.90	1.96
Skin	0.94	2.10	2.10	-

5.2.2 Model B – Effect of Substrate Anisotropy

Once the modeling scheme used in Model A was validated through experimental results, similar modeling technique was adopted to understand the directional dependence of dielectric constant of printed substrates. In this case, a cuboid of dimensions 50 mm × 50 mm × 5 mm was designed in ANSYS-HFSS for further analysis. Two models were simulated with base dielectric constant of 3 and one model with base dielectric constant of 4. This was achieved by editing the dielectric permittivity for each model while assigning the material properties. While assigning the material properties to the model, anisotropy was considered but the x, y, and z tensors were given same value to check if there was any difference in the results (frequency of the antenna). Table 4 shows the assigned material properties. The relative permittivity shown in the Table 4 was varied in x, y and z directions to understand the anisotropy effect on resonant frequency.

Table 4 - Material properties assigned for Model B

Name	Type	value	units
Relative Permittivity	Anisotropic		
T(1,1)	Simple	3	
T(2,2)	Simple	3	
T(3,3)	Simple	3	
Relative Permeability	Anisotropic		
T(1,1)	Simple	1	
T(2,2)	Simple	1	
T(3,3)	Simple	1	
Bulk Conductivity	Anisotropic		siemens/m
T(1,1)	Simple	0	
T(2,2)	Simple	0	
T(3,3)	Simple	0	
Dielectric Loss Tangent	Anisotropic		
T(1,1)	Simple	0.01	
T(2,2)	Simple	0.01	
T(3,3)	Simple	0.01	
Magnetic Loss Tangent	Anisotropic		
T(1,1)	Simple	0	
T(2,2)	Simple	0	
T(3,3)	Simple	0	
Magnetic Saturation	Simple	0	tesla
Lande G Factor	Simple	2	
Delta H	Simple	0	A_per_meter
Measured Frequency	Simple	9.40E+09	Hz
Mass Density	Simple	1052	Kg/m^3

As the material is printed in a crisscross manner in x and y directions, the properties in the x and y directions will be identical; however, the z direction properties will be different. Three models were simulated by changing the dielectric property in x, y and z directions. The 3D isometric view of the model B is shown in Figure 5.4.
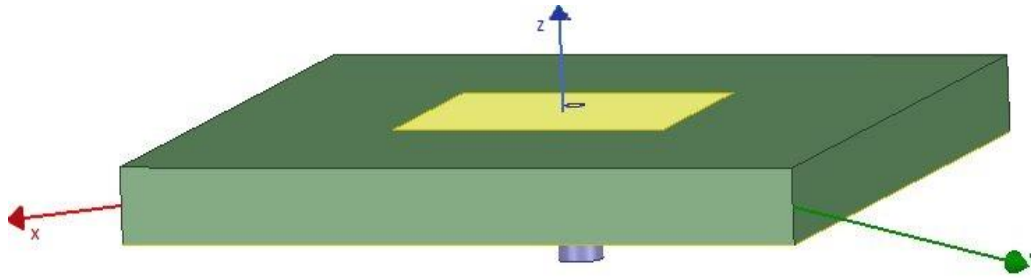
Figure 5.5 3D isometric view of the HFSS model B.

For the first model (Model B-I), ε_{rx}, ε_{ry} were considered to be 3, while ε_{rz} was varied between 20% and 100% of ε_{rx}. For the second model (Model B-II), ε_{rx} and ε_{ry} were considered to be 4, while ε_{rz} was varied between 15% and 100% of ε_{rx}. The third model (Model B-III) was similar to that of first model, but the z direction, dielectric constant ε_{rz} was kept constant and the x, y direction properties were varied between 20% and 100% of ε_{rz}.

5.2.3 Model C – Hybrid Structure

The hybrid structure comprising of lattice and solid part was imported into ANSYS-HFSS for evaluating the antenna performance. From the results of the impact test, it was observed that the indentation was about 9 mm. If the hybrid structure is impacted on its solid part under which the patch antenna is placed at the contact surface of the lattice and solid part, it would get damaged. So, impacting the hybrid structure on the lattice would be the correct orientation of the structure. In this way, the frequency of the antenna can be controlled by the changing the fill density of the solid base resulting to a good electro-mechanical structure.

While performing the numerical EM analysis on the hybrid structure, the software was not able to solve due to the complexity of the structure. As the impact was only affecting a thickness of 10 mm in the structure, the hybrid structure was remodeled to a final dimension of 50 mm x 50 mm x 10 mm which had only one layer of lattice structure (model C-I). A simulation was performed at a frequency of 2.4 GHz with only a single adaptive pass. Figure 5.6 shows the model C-I with tetrahedron element mesh.
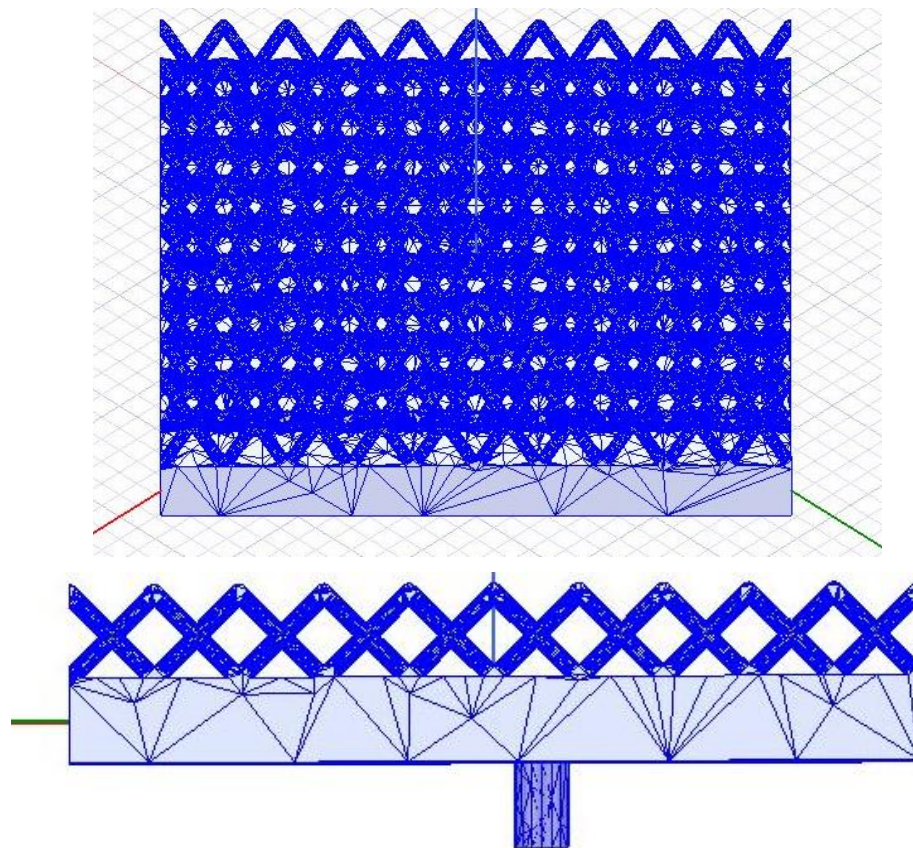
Figure 5.6 3D view and side view of model C-I with mesh.

For simplifying the simulation of the hybrid structure, two models were designed and simulated. For simulating a single layer of the hybrid structure, it took approximately two hours. First model (model C-II) consists of two solids with dimensions of 50 mm x 50

mm x 5 mm as shown in Figure 5.6. This model was designed exactly to match the model C-I. In the lattice structure, the substrate and the air were considered to be in series combination. The volume fraction of the single layer lattice was measured as 0.18. The equivalent dielectric strength of the single layer of lattice (using the equation (14)) was calculated to be 1.1378. The dielectric strength of the solid was considered as 3 for the above calculation. Both the models C-I and C-II gave approximately same results. Figure 5.7 shows the resonant frequencies of the models C-I and C-II.
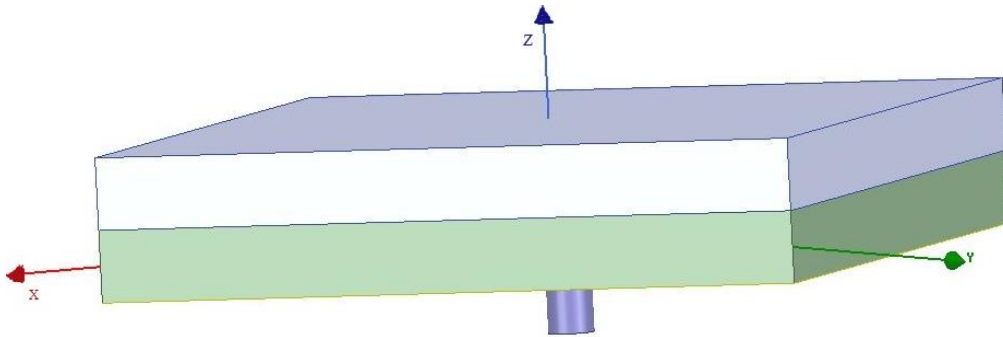
Figure 5.7 3D isometric view of model C-II.
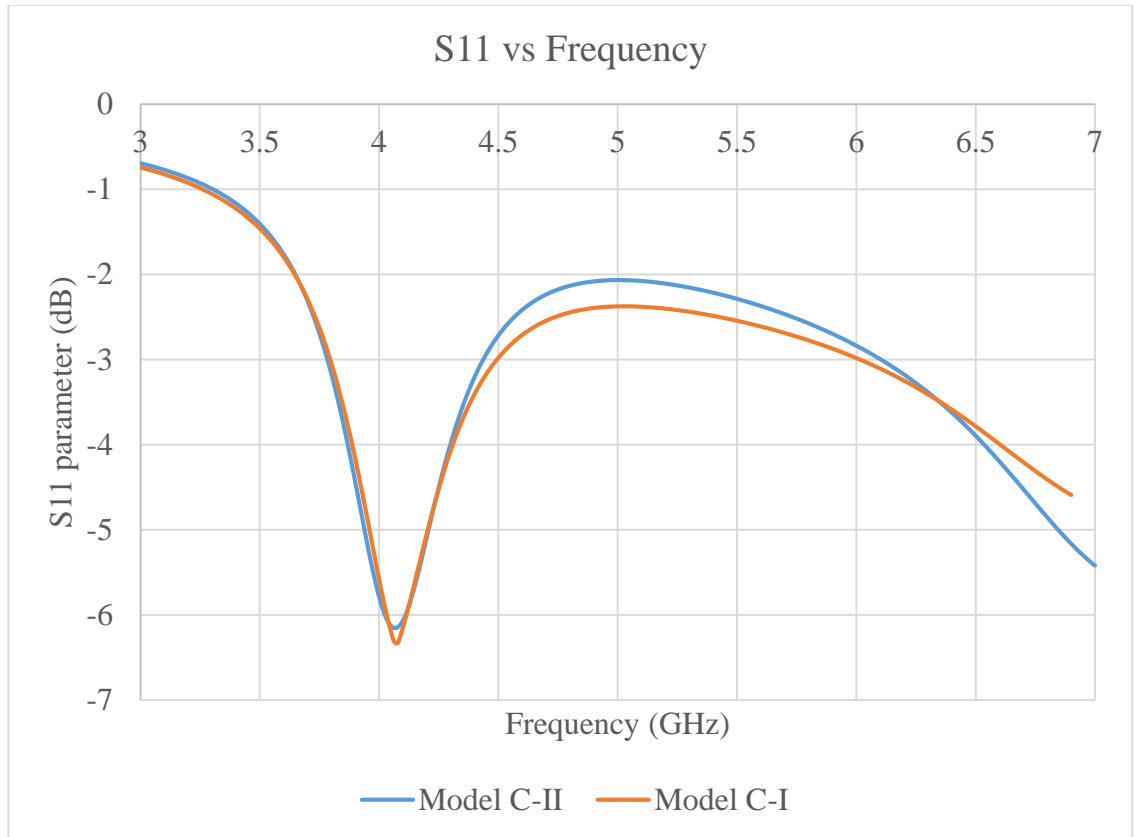
Figure 5.8 HFSS simulation results of models C-I and C-II.

5.2.4 HFSS Modeling Before Impact Testing

5.2.4.1 Before Impact on Lattice Side

The HFSS model impacted on the lattice side was excited through a co-axial probe. From the results of model C-I and C-II, it was clear that the lattice in the hybrid structure can be replaced with an equivalent dielectric solid (model C-III). So, the 15 mm lattice structure was replaced with a 15 mm thick solid of similar dielectric strength as shown in the Figure 5.9. The bulk dielectric strength of substrate was considered as 3. Using equation (14), the equivalent dielectric strength was calculated to be 1.1359. By using this type of modeling approach, a lot of computation time and memory was saved.
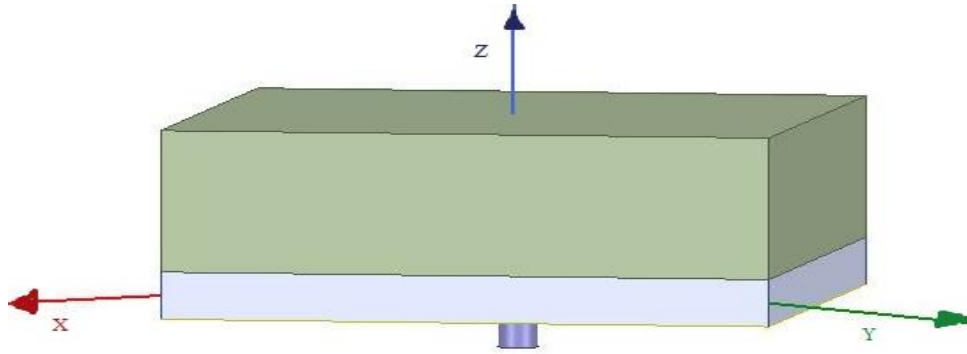
Figure 5.9 3D isometric view of the model C-III.

5.2.4.2 Before Impact on the Solid Side

As the ground plane is on the top surface of the solid part, the patch antenna was excited through a microstrip line as shown in the Figure 5.10. The dimensions of the microstrip line is 15 mm x 2.5 mm. The microstrip line was united with the patch and finite conductivity was assigned as boundary condition. The red colored strip in the Figure 5.10 is assigned as lumped port. Now the 15 mm solid cuboid replacing the lattice structure with equivalent dielectric properties is imported as shown in Figure 5.11 and the simulation is run.
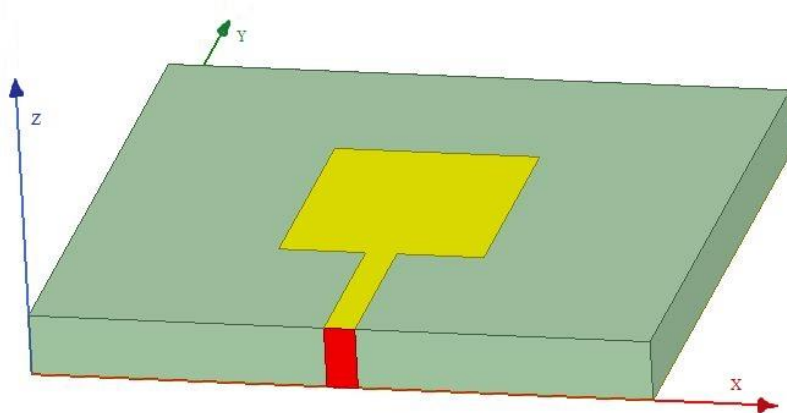
Figure 5.10 Microstrip line attached to patch antenna (Yellow) and Excitation port (Red).
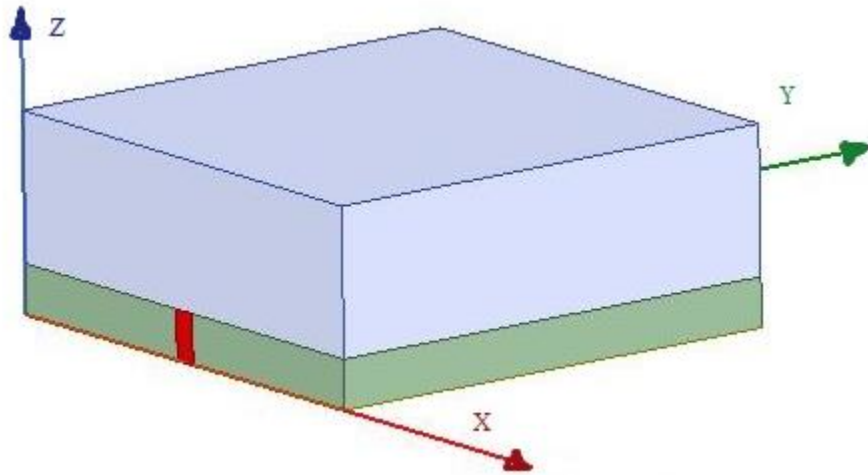
Figure 5.11 3D view of HFSS model before impacting on solid part.

5.2.5 HFSS Modeling After Impact Testing

5.2.5.1 After Impact on Lattice Side

The experimental results of the low velocity impact test on the lattice side were considered for modeling the impacted hybrid structure in ANSYS-HFSS. The model C-III was modified by creating a semi-spherical recess of radius 4.5 mm on the 15 mm thick equivalent solid part as shown in Figure 5.12. Equation (14) was used to calculate the equivalent dielectric strength of the lattice structure considering that lattice and air are in series arrangement. Two different materials were created in the materials library; one with the equivalent dielectric properties given to the 15 mm thick solid and the other with regular ABS dielectric properties. The model was simulated at 2.4 GHz frequency with a step size of 0.02 and 20 adaptive passes. These adaptive passes are given generally to increase the accuracy of the results.

70
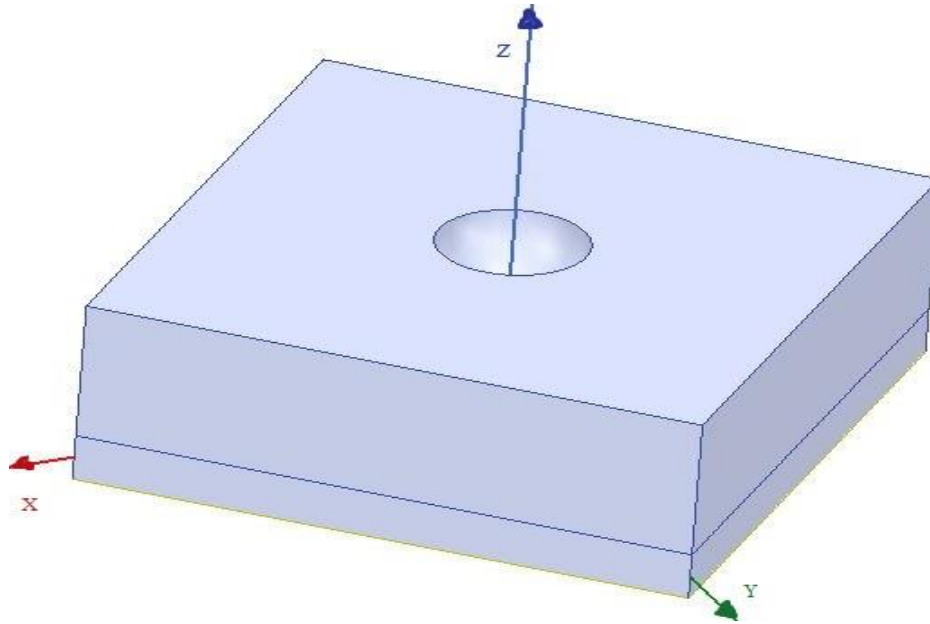
Figure 5.12 HFSS model after impact on lattice side.

5.2.5.2 After Impact on Solid Side

It is observed from the cross-sectional analysis of the impacted specimens that the solid surface has deformed about 3.34 mm. As the deformation is in the shape of a semi-sphere, it is difficult to create a sheet on the deformed surface. As solution to this problem, a cylinder is assumed instead of a semi-sphere. The height and radius of the cylinder are taken as 3.34 mm and a sheet is wrapped along the surface of the cylinder. A circular sheet of radius 3.34 mm is drawn on the top surface of the cylinder and united. Later, a rectangular sheet of dimensions 13.62 mm x 16.51 mm is drawn and a circle of radius 3.34 mm is subtracted from center of rectangle. The rectangle is added with united cylinder wrap to form the deformed shape of patch antenna as shown in Figure 5.13. Similar procedure is followed for designing the ground plane. The patch antenna is excited through the microstrip line. The lattice structure is replaced with a solid cuboid with the equivalent dielectric properties as shown in Figure 5.14 and the simulation is run.

71
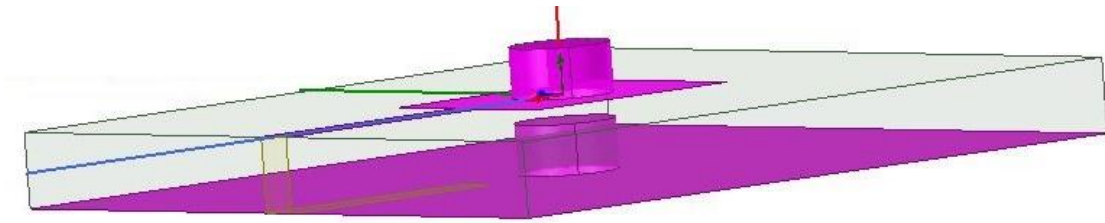
Figure 5.13 Solid part of hybrid structure with deformed antenna and ground plane.
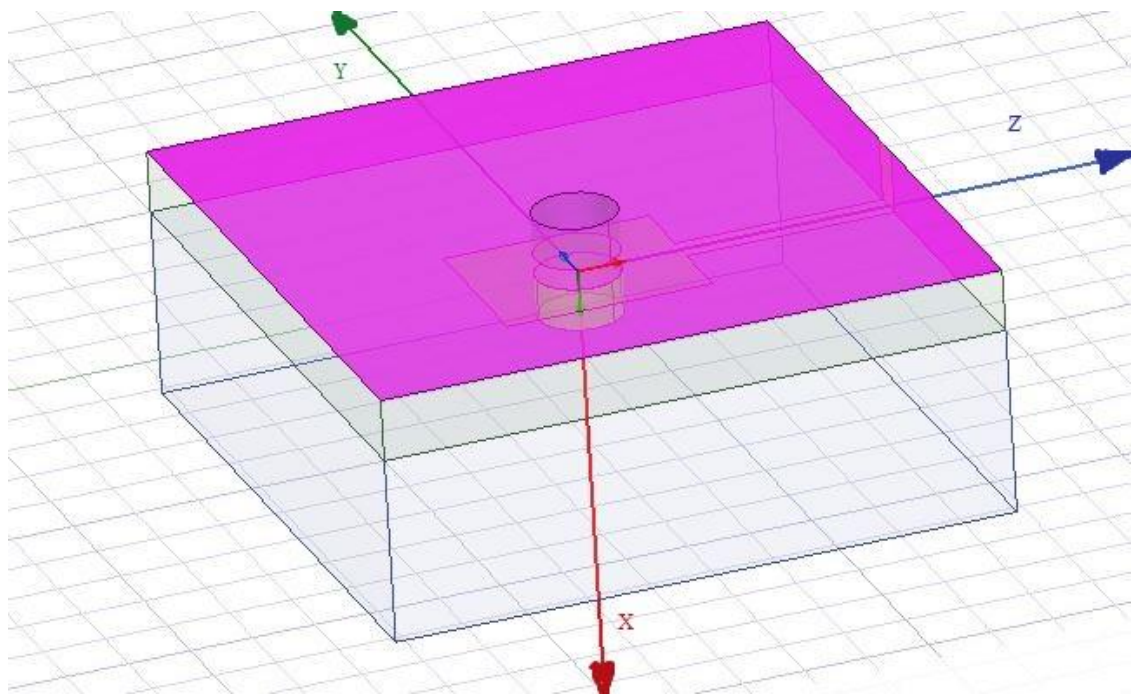
Figure 5.14 HFSS model of the Hybrid structure impacted on the solid side.

5.3 FEA Modeling of Low-Velocity Impact Test using ABAQUS

Low velocity impact analyses of the hybrid structure were performed using the ABAQUS Explicit program. The dynamic explicit analysis model consisted of hybrid structure and an impactor based on the experimental set up. The structure was impacted on both top and bottom surfaces (solid and lattice respectively). The quadratic tetrahedrons (C3D10M) with a size of 0.3 mm were chosen as element type for meshing the hybrid structure. The impactor was designed using ABAQUS CAE and meshed using a linear

72

quadrilateral element (R3D4). For the model in which lattice structure was impact tested, a Kevlar sheet was designed as shown in Figure 5.15(a) and the material properties were given.
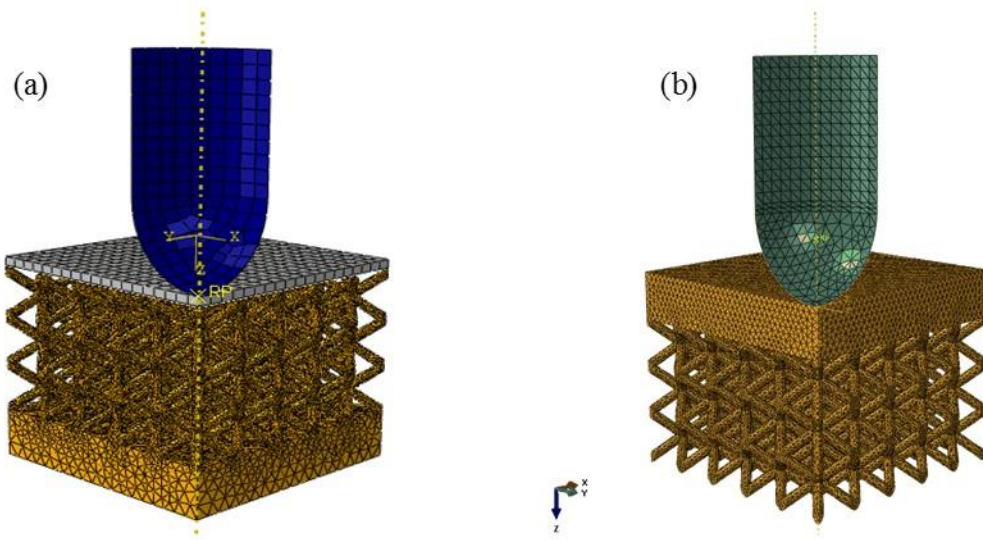
Figure 5.15 ABAQUS quarter model impacted on (a) lattice part, (b) solid part.

The material properties of ABS were taken from Table 3 [57] and the mechanical properties of the Kevlar face sheets were taken from the Hexcel website [56]. Figure 5.15 shows the element size of the impactor tip, ABS hybrid structure and the Kevlar face sheets. A quarter part of the model was selected for analysis to reduce the simulation time. To get accurate results, the step time was set up with an increment of 1E-07. The simulation time for the quarter model was about 7 hours.

Clamped boundary condition was used for the analysis, similar to the experimental test. The sides of the Kevlar face sheets were fixed and the bottom surface of the model was also fixed. Since only quarter part of the model was selected for analysis, it was important to give symmetry boundary conditions on the inner faces of the structure as shown in Figure 5.16.
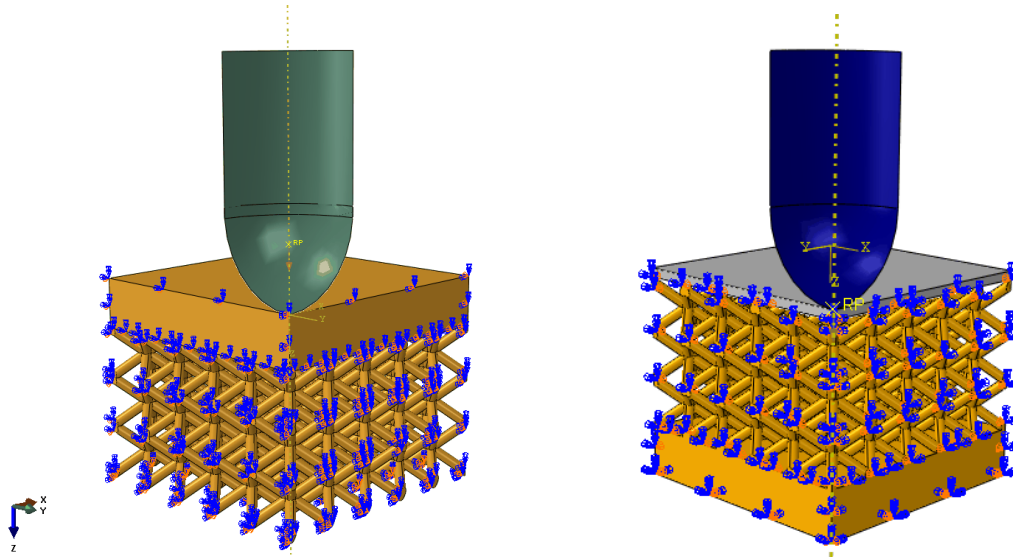
Figure 5.16 Symmetry boundary conditions at the inner faces and fixed boundary condition at outer faces of the quarter model.

Load, velocity, displacement and energy absorption history have been obtained from the results of the simulation. The data was processed in an Excel worksheet and compared with experimental results as explained in CHAPTER 6: RESULTS AND DISCUSSION.

CHAPTER 6 : RESULTS AND DISCUSSION

6.1 Overview

The experimental results along with the FEA results have been discussed in this section. A total of six specimens were impact tested with low velocity, in which three were impacted on the solid part and three were impacted on the lattice structure. These results were compared with the ABAQUS model results. The RF response of the patch antenna printed on the porous substrates was compared with the ANSYS-HFSS model results. The damage tolerance capabilities of embedded hybrid structure were investigated to analyze the minimal damage after impact.

6.2 3D X-ray Microscopy Results

3D images and related slice views are shown in Figure 6.1, 6.2 and 6.3 that give a clear depiction of the internal components of the printed substrates. For all Figures 6.1-6.3, panels a, b, and c show the slice views in vertical plane, three orthogonal planes, and horizontal plane through the core, respectively. Panels d, e, and f represent 3D view of top shell, core, and entire section, respectively. It is clear from each of the 3D images that the printer's preset fill densities are just employed in the core. Vertical plane slice views in Figure 6.1(a), 6.2(a), and 6.3(a) are also presented with dimensions in mm. It is observed that the top and base layers are around 0.4 and 0.9 mm, respectively for 25% samples (Figure 6.1a), around 0.3 and 0.8 mm, respectively for 50% samples (Figure 6.2a) and around 0.6 and 0.7 mm, respectively for 75% samples (Figure 6.3a). For all the samples,

printer preset thicknesses were considered to be 0.6 mm. It is thus concluded that the

LulzBot printer has limitation in precision printing at low in-fill densities. Top and bottom

layers appeared to be printed practically solid and all specimens are printed in diagonal

direction per layer and in-fill pattern is clearly linear as expected according to Figure 3.2.
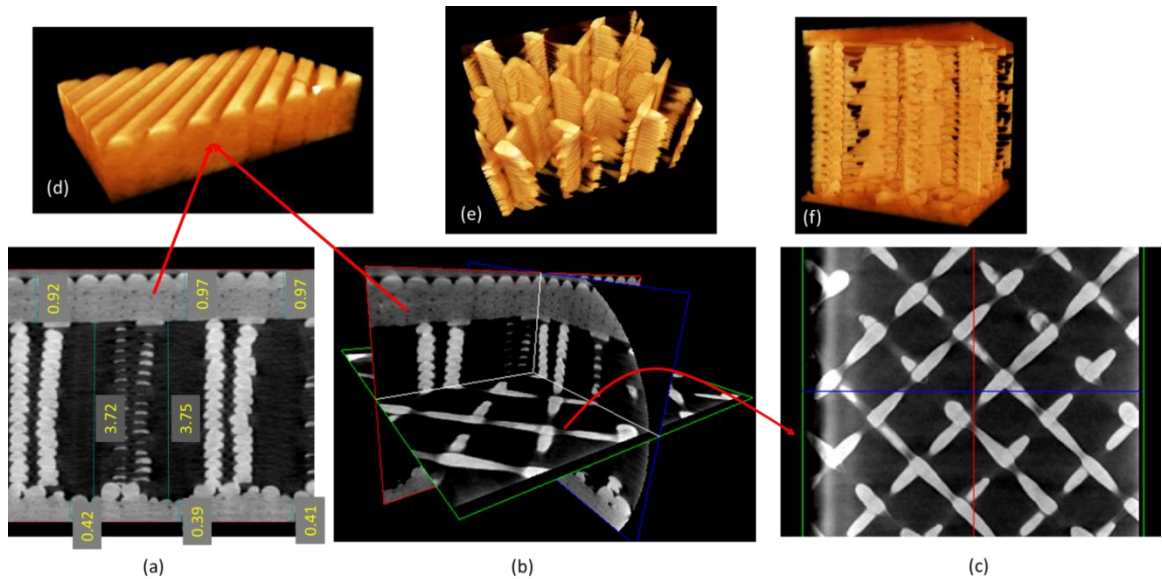
Figure 6.1 X-ray images of samples created with printer setting of 25% in-fill density. (a) Vertical plane slice view with dimensions in mm, (b) Slice view of three orthogonal planes, (c) Slice view of horizontal plane through the core, (d) 3D view of top shell, (e) Core and (f) Entire section

The X-ray images showing the lattice structure of cores uniformly patterned and

distributed (panel b, c, and e of Figures 6.1-6.3). It is clear from the images that columns

of void and solid structures are arranged in parallel in y (thickness) direction and in series

in x and y directions. The actual solid volume fraction may be different from the machine

preset fill density due to the printer limitation. To compute actual solid volume fraction,

pore volume was isolated from solid by performing advanced image segmentation (using

Scan IP software).
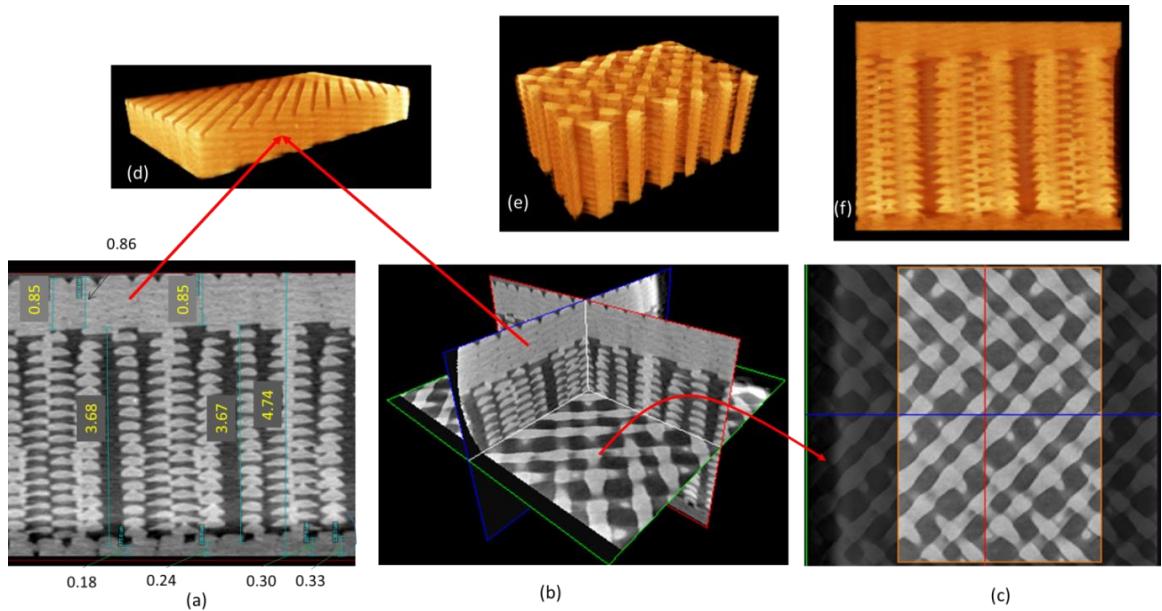
Figure 6.2 X-ray images of samples created with printer setting of 50% in-fill density. (a) Vertical plane slice view with dimensions in mm, (b) Slice view of three orthogonal planes, (c) Slice view of horizontal plane through the core, (d) 3D view of top shell, (e) Core and (f) Entire section
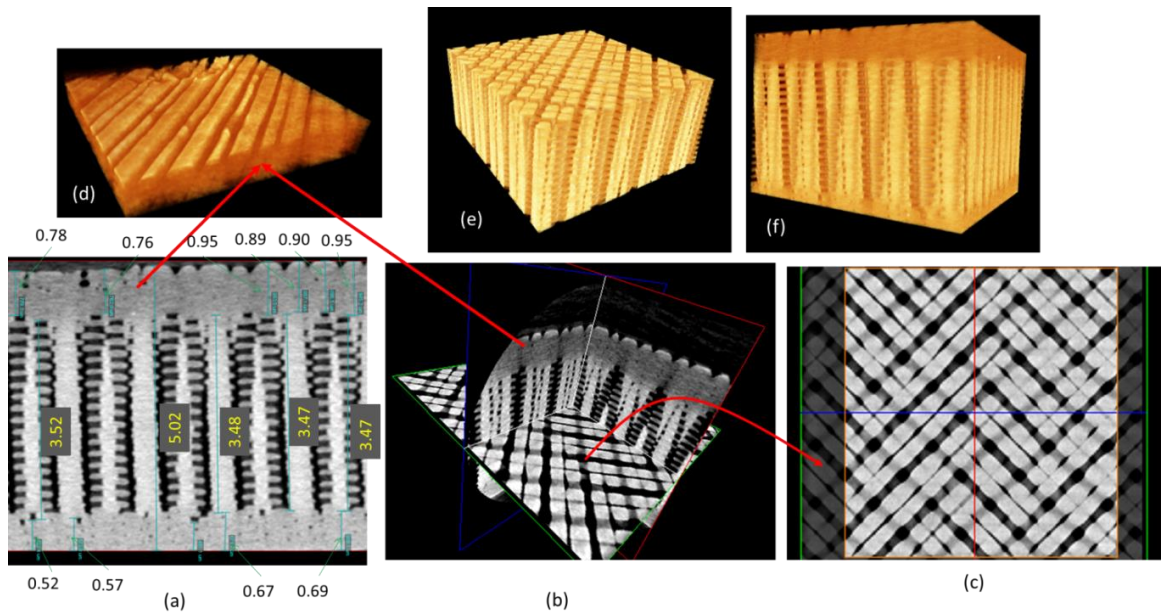
Figure 6.3 X-ray images of samples created with printer setting of 75% in-fill density. (a) Vertical plane slice view with dimensions in mm, (b) Slice view of three orthogonal planes, (c) Slice view of horizontal plane through the core, (d) 3D view of top shell, (e) Core and (f) Entire section.

Then the ratio of solid volume section from a representative volume element (RVE) was calculated. RVEs were isolated from the x-ray images shown in Figures 6.1-6.3 for both core and skin regions. The measured solid volume fraction for core regions were 33.5%, 54.4%, and 75.3% from printer settings of 25%, 50%, and 75%, respectively. The solid volume fraction for top and bottom skins were measured to be 94% for all samples although it was supposed to be completely solid. The x-ray image analysis shows that the true solid volume fraction after manufacturing matches nearly for higher fill densities; though, 25% fill density gives 33% volume solid fraction. Again, the discrepancy may be attributed to the limitation of LulzBot printer for printing low density structures.

6.3 RF Characterization

The RF characterization was performed on the microstrip patch antenna. The representative resonant frequency (S_{11}) data from the LulzBot created samples are shown in Figure 6.4. The average resonant frequency data along with the 3D X-ray measured porosity and the machine preset fill density is summarized in Table 5.

Table 5 LulzBot printer preset porosity and experimentally Measured porosity vs. resonant frequency

Printer Setting		X-ray measured porosity (%)	Resonant Frequency (GHz)
Fill density (%)	Porosity (%)		
25	75	66.5	5.68
50	50	45.6	5.47
75	25	24.7	5.15
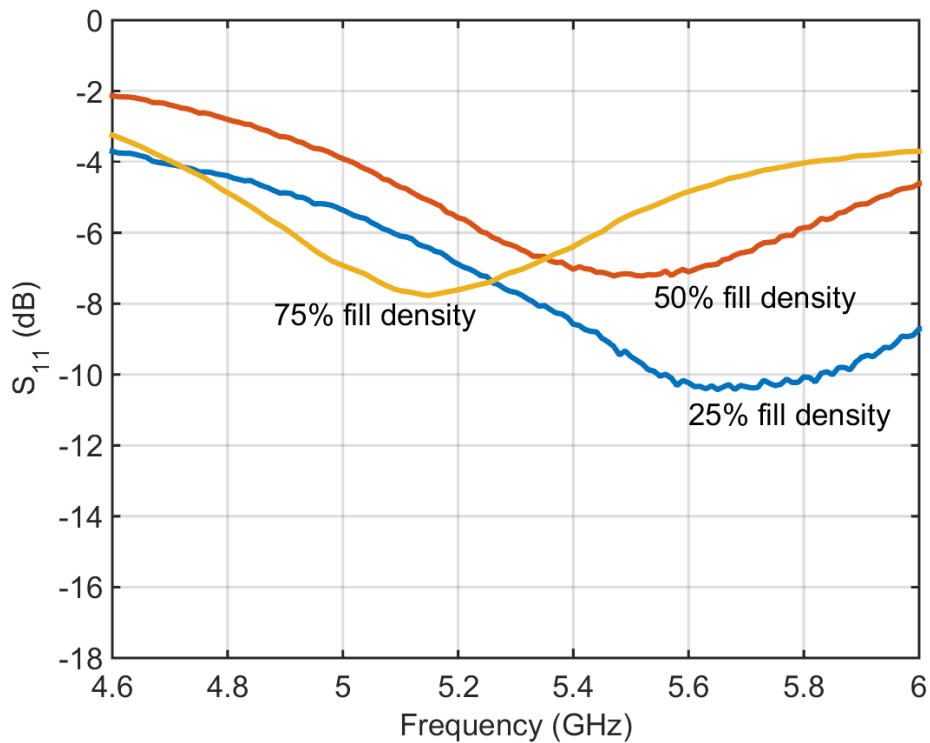
Figure 6.4 Representative measured S11 (dB) vs. frequency plots for LulzBot printed samples [22].

Resonant frequencies of antennas created on 25%, 50%, and 75% substrates were measured to be 5.68, 5.47, and 5.15 GHz, respectively. Thus, the resonant frequency appears to decrease as the core fill density increases. These results obtained from the experiment are intuitively correct as higher the core fill density, higher is the dielectric constant. Since the antenna dimension is approximately half of the operating wavelength, specimens with high dielectric constant (e.g. high dielectric constant) should exhibit a lower resonant frequency according to equation (8). At this point, direct correlation between the dielectric constant and resonant frequency was not possible as dielectric constant of bulk ABS material used with the printer was not known. The experimental frequency data along with the measured porosity of the printed samples and ANSYS-HFSS

model can be used to back calculate the bulk dielectric constant, which is explained in section 5.2.1.

6.4 ANSYS-HFSS Results

The EM analysis was performed on the HFSS models designed in the section 5.2. The resonant frequency was plotted with the S_{11} parameter for all the models. Detailed explanation is given below:

6.4.1 Model A – Three-Layered Substrate

An iterative simulation was performed on the model with 75% fill density to determine the resonant frequency that matches with the experimental frequency by changing the dielectric strength of solid (thereby varying ε_{rx}, ε_{ry}, ε_{rz}). The bulk dielectric constant was found to be $\varepsilon_r = 2.2$ for which the computational frequency was 5.16 GHz, which is close to the experimental measurements of 5.15 GHz. The same dielectric constant was utilized to compute the respective frequencies of the models with 50% and 25% fill densities. The dielectric constant calculated for the fill densities 25%, 50%, and 75% and used in the models are tabulated in Table 6.

Table 6 Printer preset fill density and experimentally measured volume fraction vs experimental and ANSYS-HFSS simulated resonant frequency

Printer Setting Fill density (%)	Experimental Resonant Frequency (GHz)	HFSS Resonant Frequency (GHz)	Difference between the Experiment and HFSS results
25	5.68	5.61	1.2 %
50	5.47	5.37	1.8 %
75	5.15	5.16	-

The resonant frequencies simulated in ANSYS-HFSS are relatively similar to the experimental resonant frequencies. The resonant frequencies determined in HFSS are plotted in Figure 6.5 and are shown in Table 6 as well. It is observed from Table 6 that the computational resonant frequencies are within only 1.8% of the experimental measurements. Thus, the modeling scheme adopted here can be considered acceptable. Same modeling schemes were used for further understanding the influence of anisotropy in dielectric constant on patch antenna resonant frequencies.
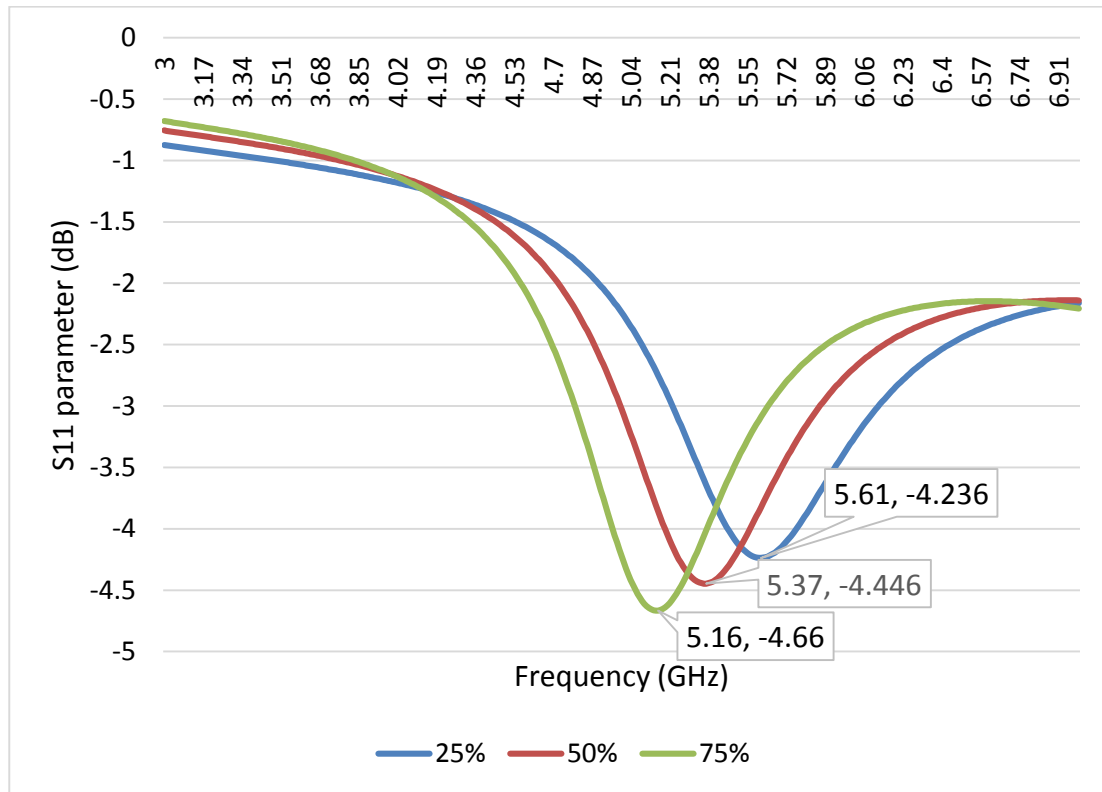
Figure 6.5 ANSYS-HFSS result of the frequencies for printer present in-fill densities of 25%, 50%, 75% (Model A).

6.4.2 Model B – Effect of Substrate Anisotropy

The directional dependence of dielectric constant of printed substrates was understood with the help of this modeling technique. Figure 6.6 illustrates the simulated results of the Model B-I, where the z direction dielectric constant was varied between 100% and 20% of $\varepsilon_{rx} = 3$. The resonant frequency for ε_{rz} equals to 100% of ε_{rz} is observed to be 4.31 GHz, while at 20% the frequency has substantially increased to 6.35 GHz. As the dielectric constant in the z direction ε_{rz} is varied from 100% to 20% of $\varepsilon_{rx} = 3$, the resonant frequency gradually increased about 47.3%. A similar behavior can be observed in Figure 6.7 for the Model B-II with a 58.0% increase in the resonant frequency for $\varepsilon_{rx} = 4$.
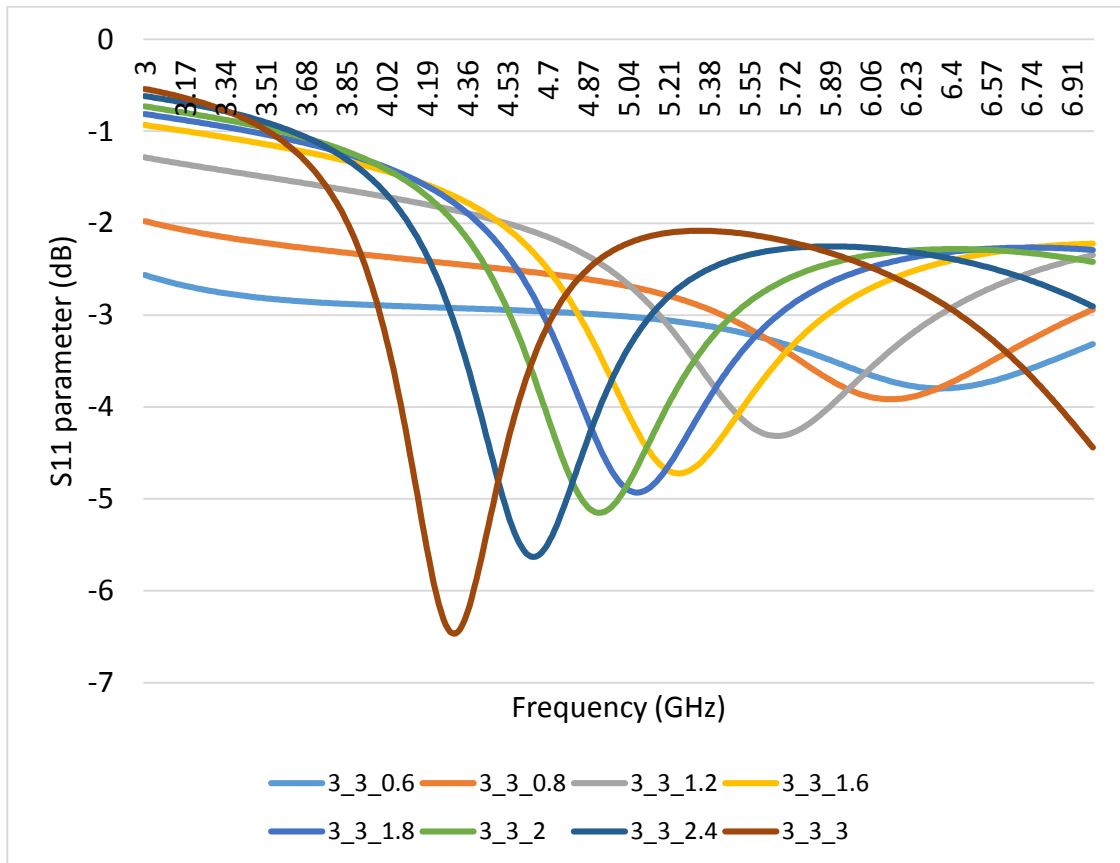
Figure 6.6 ANSYS-HFSS results from Model B-I for constant ε_{rx} and ε_{ry} and varied ε_{rz}. In this case, $\varepsilon_{rx} = \varepsilon_{ry} = 3$. The plot legend is formatted as ε_{rx} _ε_{ry} _$\varepsilon_{rz.}$
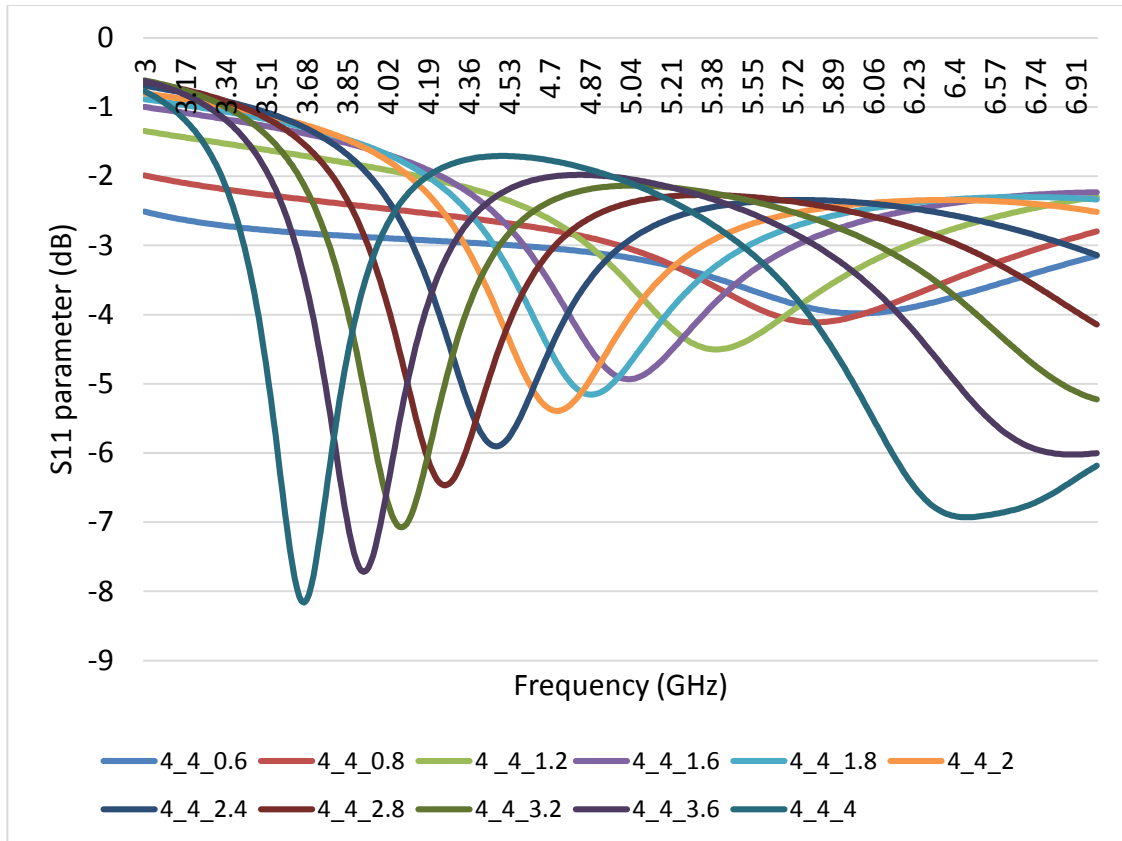
Figure 6.7 ANSYS-HFSS results from Model B-II for constant ε_{rx} and ε_{ry} and varied ε_{rz}. In this case, $\varepsilon_{rx} = \varepsilon_{ry} = 4$. The plot legend is formatted as $\varepsilon_{rx} \_ \varepsilon_{ry} \_ \varepsilon_{rz}$.

Figure 6.8 indicates the result of the model B-III, where the directional dielectric constant ε_{rx} and ε_{ry} are varied from 100% to 20% of ε_{rz}. The resonant frequency at 100% and 20% are 4.31 GHz and 4.67 GHz respectively, which indicates only a minor change of 8%. Since the resonant frequency is not affected much by the variation of lateral direction dielectric constants, results from Figures 6.6 and 6.7 are summarized in Figures 6.9 and 6.10 for better understanding the effect of thickness direction dielectric constants. Figure 6.9 illustrates the correlation between the thickness direction relative permittivity ε_{rz} and the resonant frequency for $\varepsilon_{rx} = 3$ and $\varepsilon_{rx} = 4$. This figure also includes the thickness direction relative permittivity of printed substrates obtained from the experimental results and HFSS Model A. It may be mentioned here that lateral direction relative permittivity is

different for different fill density. It is observed that resonant frequency f decreases

nonlinearly with thickness direction relative permittivity for both $\varepsilon_{rx}=3$ and $\varepsilon_{rx}=4$.
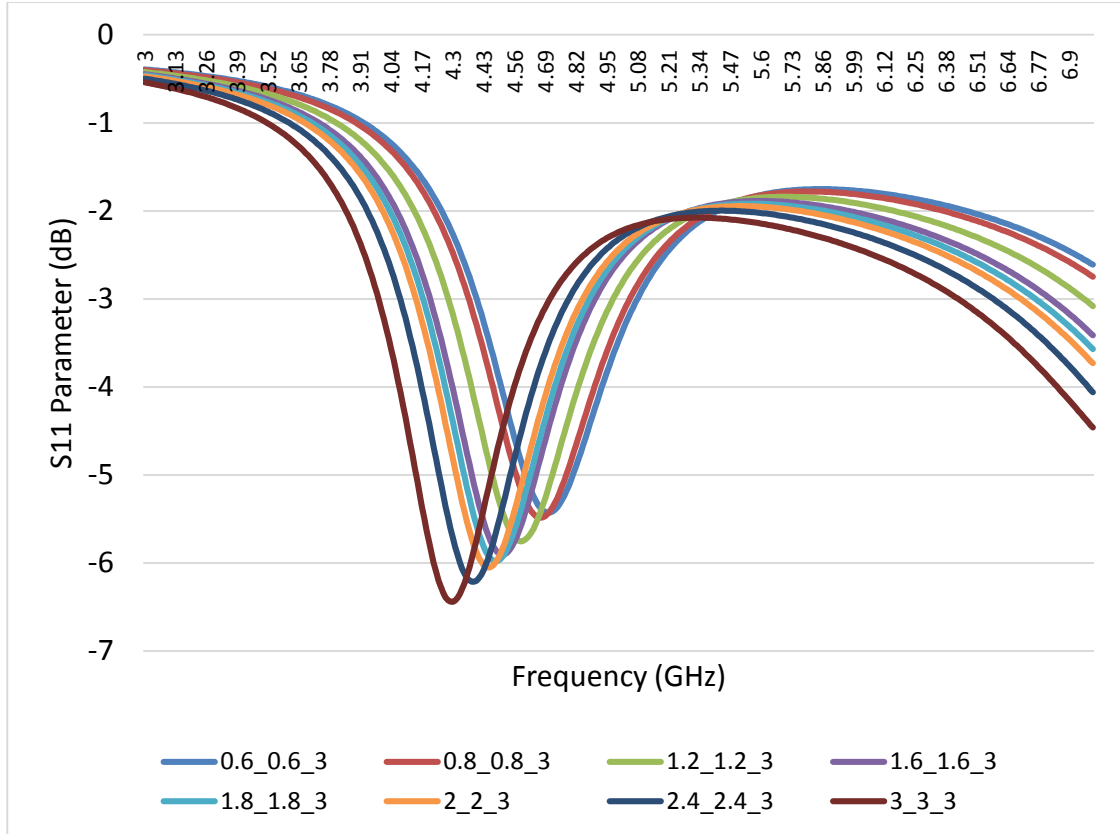
Figure 6.8 ANSYS-HFSS results from Model B-III for constant ε_{rz} and varied ε_{rx} and ε_{ry}. In this case, $\varepsilon_{rz} = 3$. The plot legend is formatted as $\varepsilon_{rx}\_\varepsilon_{ry}\_\varepsilon_{rz.}$

Results from Figure 6.9 are used to plot the permittivity ε_{rz} vs. the inverse of the

square of resonant frequency $(1/f^2)$ and is shown in Figure 6.10. The results depicted from

Figure 6.10 exemplify the linear relationship that complies with equation (9). From the

above discussion, it can be inferred that the dependence of the resonant frequency on the

change in z (ε_{rz}) direction dielectric constant is more effective when compared to changes

in the lateral x and y direction dielectric constants ε_{rx} and ε_{ry}, respectively.
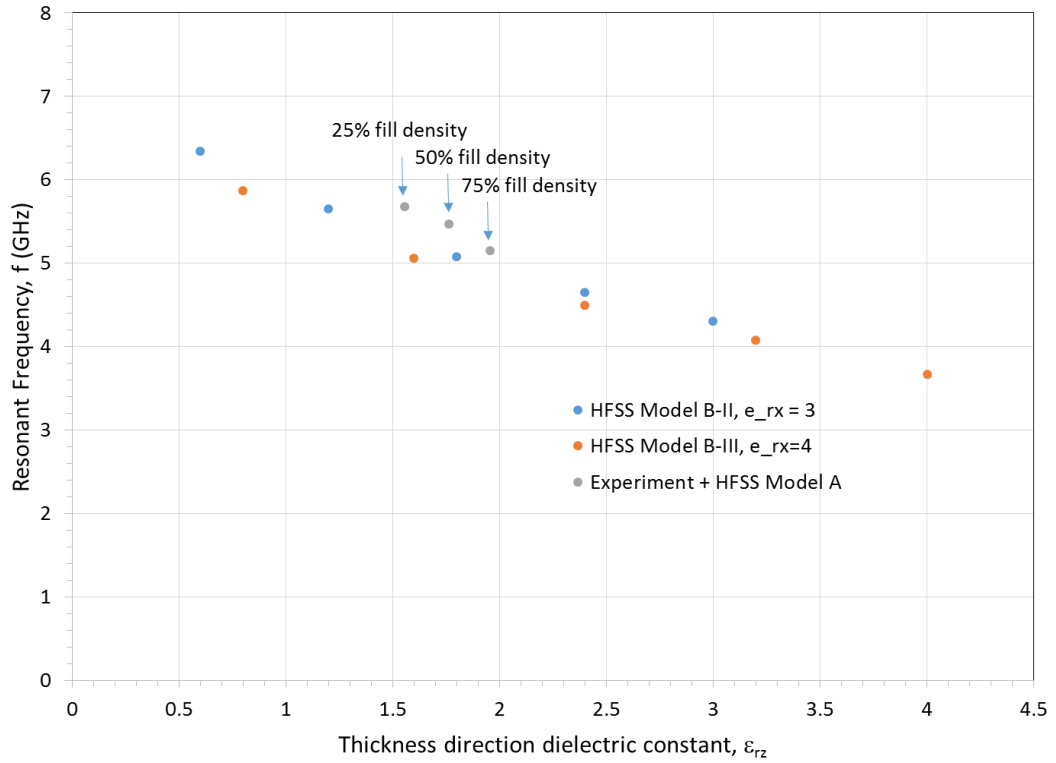
Figure 6.9 Dependence of resonant frequency on thickness direction permittivity.
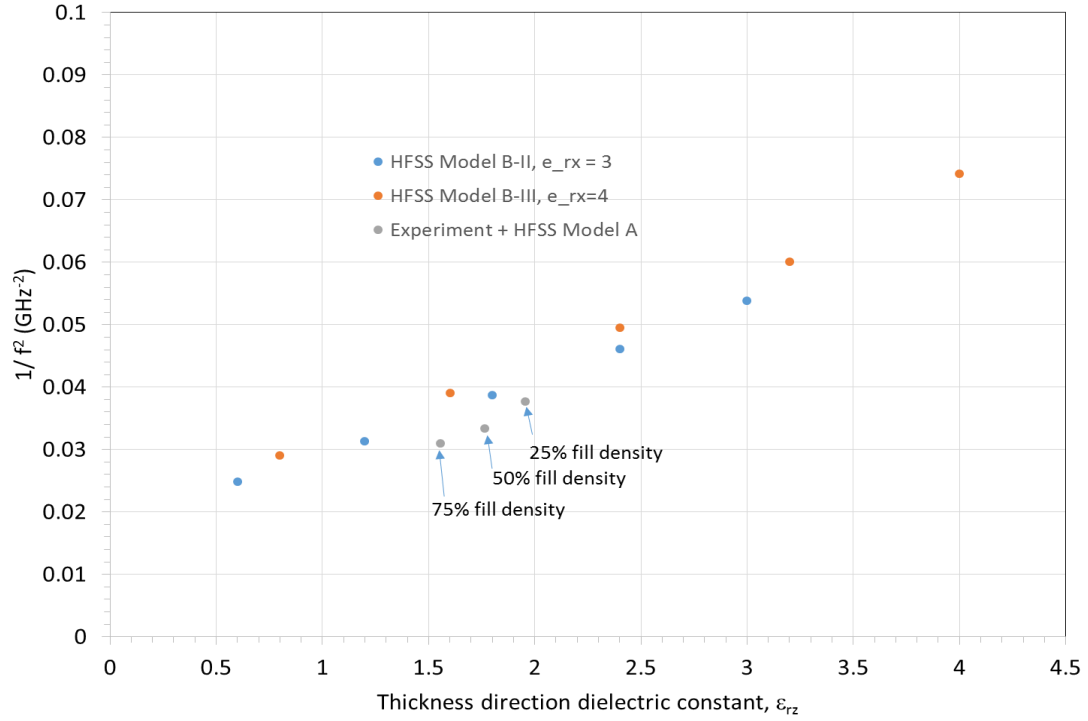
Figure 6.10 Correlation between thickness direction permittivity and inverse square resonant frequency.

The ANSYS-HFSS results exemplify that with the decrease in the material density the resonant frequency increases. By changing the directional properties, the resonant frequency can be controlled. The dominant role of the dielectric constant in the thickness direction in terms of patch antenna resonant frequency is due to such antenna's mode of radiation. The patch antenna radiates due to the fringing fields at the two opposite ends of the patch along a straight line that contains the feed. The fringing fields occur between the patch and the ground plane e.g. along the thickness direction. So naturally dielectric constant variation along the thickness direction has a more pronounced effect on the resonant frequency of the patch antenna.

6.4.3 HFSS Results of the Models Before Impact Test

The calculated equivalent dielectric properties of the lattice of the hybrid structure are defined in the material properties of the replacing solid cuboid. The validation check is performed on the model C-III and the simulation is run. The result of the simulation is shown in Figure 6.11. It can be interpreted from the Figure 6.11 that the resonant frequency of the model C-III is simulated to be 4.17 GHz. The S_{11} parameter represents how much power is reflected from the antenna, and hence is known as the reflection coefficient or return loss. The S_{11} parameter can be varied by changing the location of coaxial probe (which is used for exciting the antenna) along the length of the antenna. As this research only focuses on the frequency at which the antenna radiates, the S_{11} parameter is neglected. This model represents the hybrid structure before impact on the lattice side.
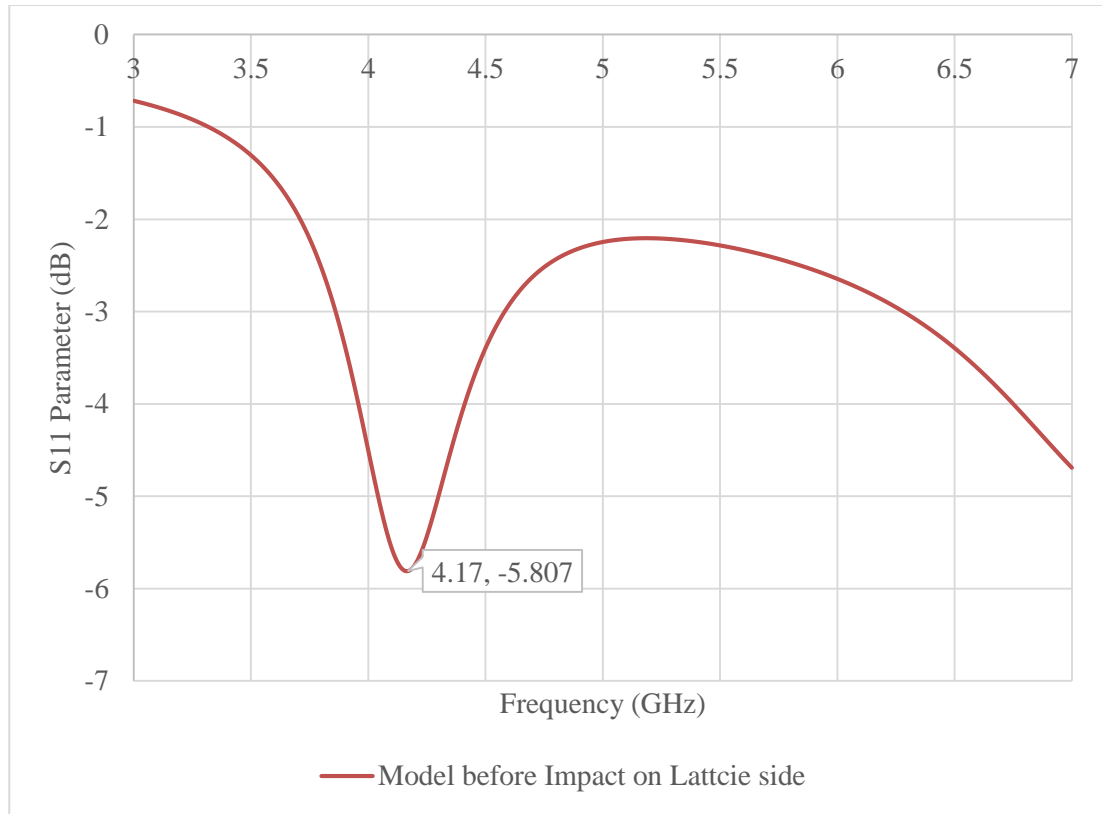
Figure 6.11 S_{11} vs Frequency plot of the HFSS model before impact test on lattice side of the hybrid structure.

Figure 6.12 shows the S_{11} parameter vs resonant frequency plot of the HFSS model before impact test on the solid side. It can be observed from the result that the resonating frequency of the model before impact on the solid side is 3.56 GHz. The S_{11} parameter, i.e. the power losses for this model are low when compared with the model before impact on the lattice side.
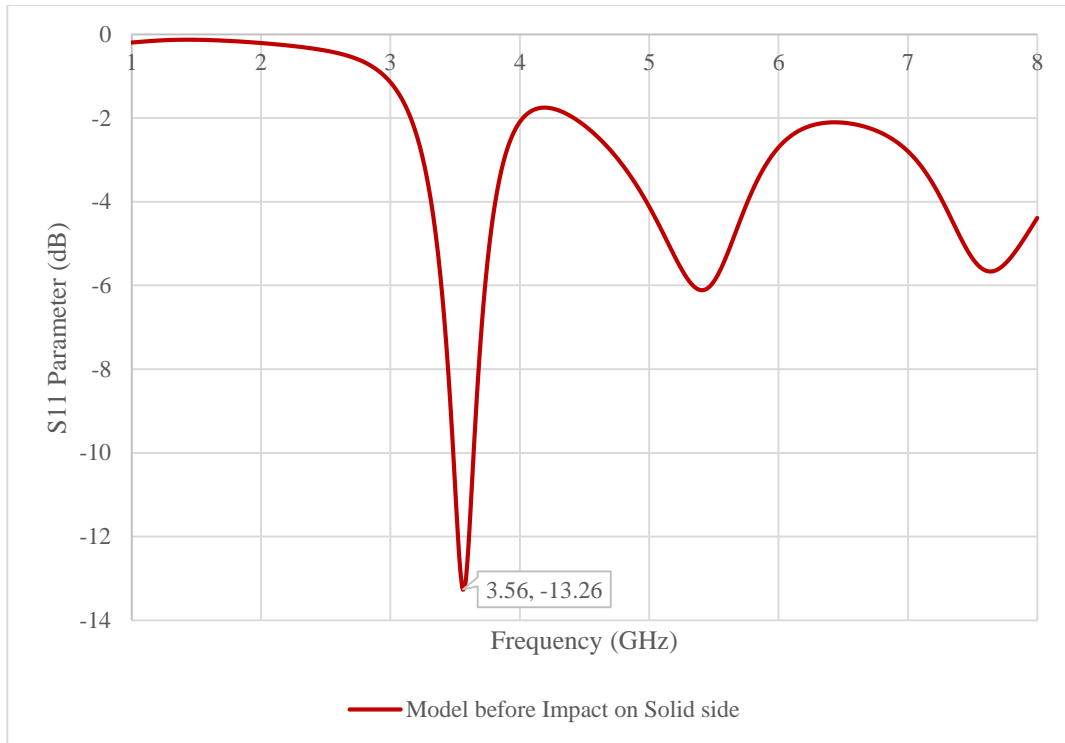
Figure 6.12 S$_{11}$ vs Frequency plot of the HFSS model before impact test on Solid side of the hybrid structure.

6.4.4 HFSS Results of the Models After Impact Test

As mentioned in the section 5.2.5, a semi-sphere hole was created on the top surface of the lattice structure (15 mm thick equivalent dielectric solid) based on the impact test results for the model impacted on lattice side. This model is checked for any errors and is simulated for achieving the results. The resonant frequency of the antenna in this model is 4.22 GHz as shown in Figure 6.13. It can be observed that the resonant frequency of the antenna has negligibly changed before and after the impact on lattice side. A solid cuboid of dimensions 50 mm x 50 mm x 5 mm is modeled to check the resonant frequency of the antenna without the lattice part of the hybrid structure. Figure 6.14 shows the results of hybrid model before and after impact on lattice side and model without lattice structure.
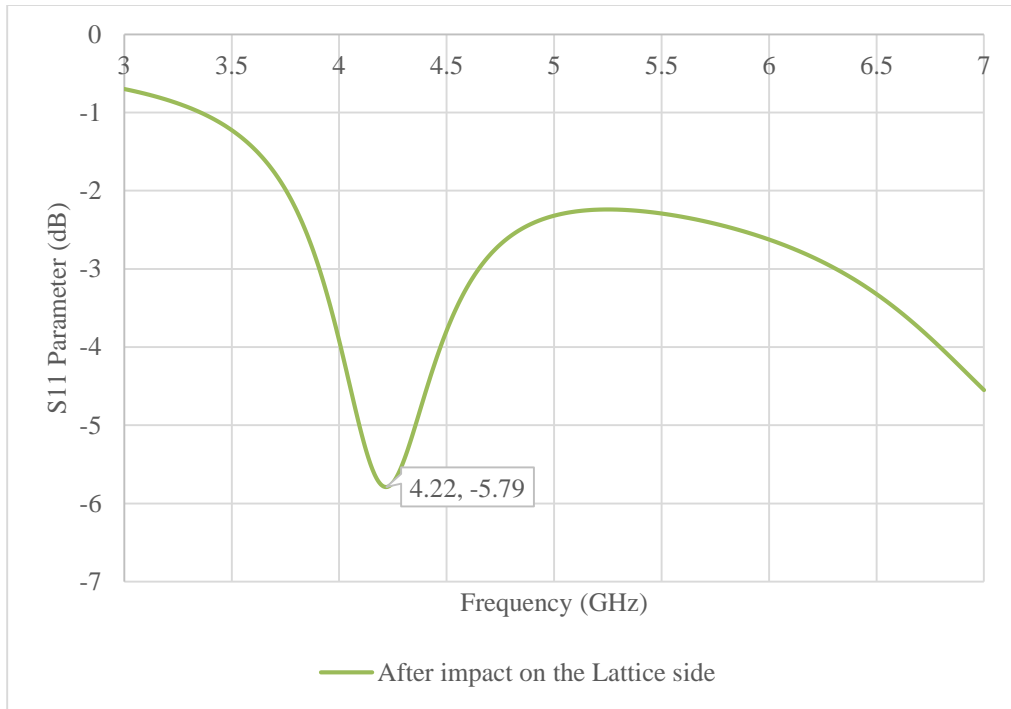
Figure 6.13 ANSYS-HFSS results of the hybrid structure after impact test on the lattice side.
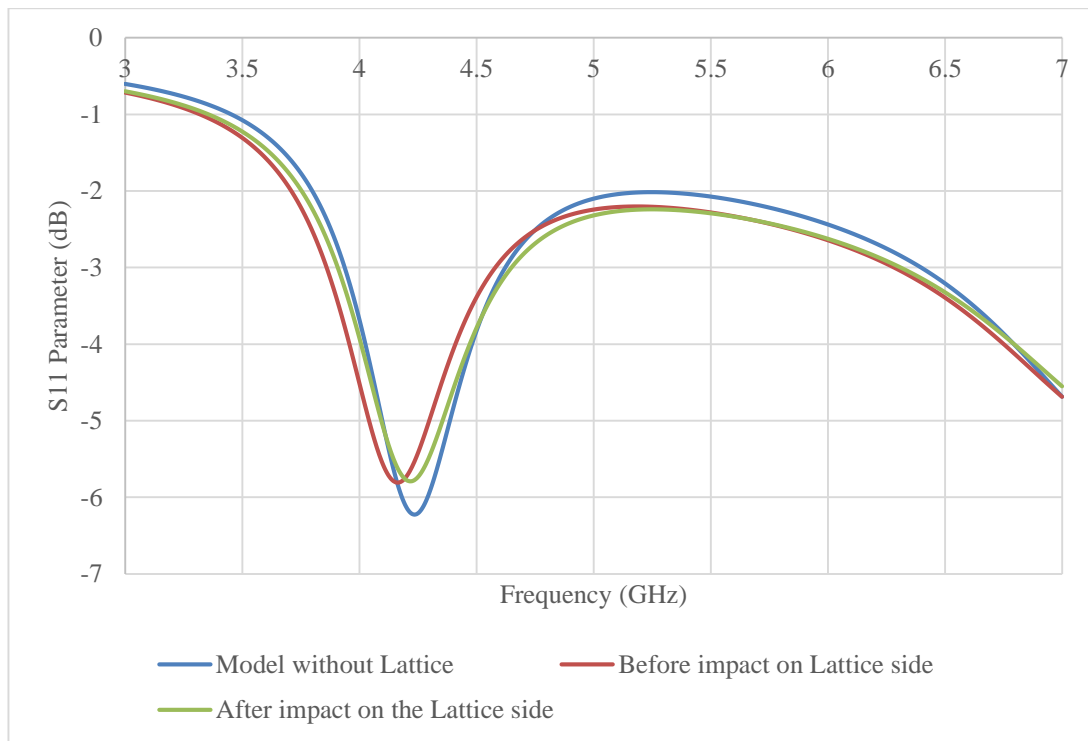
Figure 6.14 Combined ANSYS-HFSS results of hybrid model before and after impact on lattice side and model without lattice structure.

The resonant frequency of the hybrid model without lattice structure is simulated to be 4.23 GHz. The S_{11} parameter of this model is low when compared to S_{11} parameter of the hybrid model before and after impact, which indicates that the return losses are low. The resonant frequencies of the model after impact on lattice side and the model without lattice part are approximately same and the resonant frequency of the model before impact on the lattice side varies about 1.1% from the other two models.

Figure 6.15 shows the HFSS simulation results of the hybrid structure model impacted on the solid side. It can be observed that the resonating frequency of this model is 5.48 GHz. The frequency of the patch antenna has varied about 35% after the impact on the solid side of the hybrid structure.
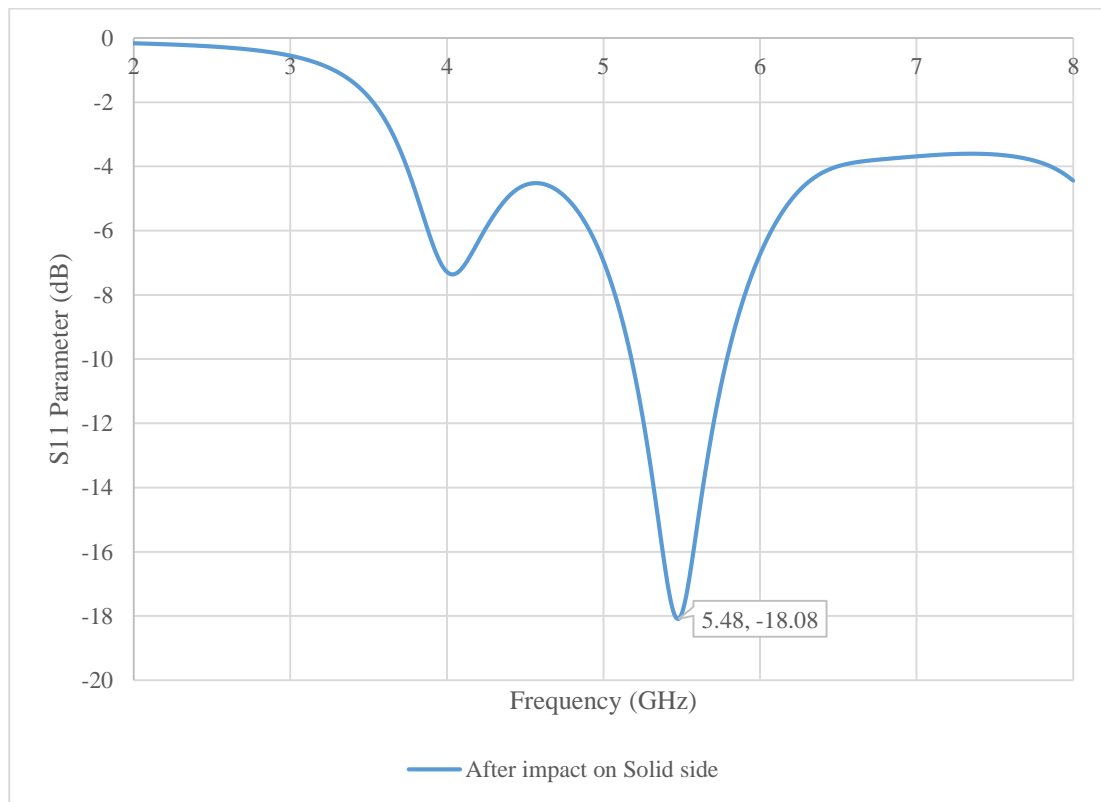
Figure 6.15 ANSYS-HFSS results of the hybrid structure after impact test on the solid side.

6.5 Low-Velocity Impact Test

The experimental and the FEA results are plotted together in an excel sheet for comparison. The experiment was performed using ASTM Standard D7136/D7136M-15 impact test machine. The height from which the impactor is dropped is measured as 0.6492m. The energy with which the impactor hits the specimens is 14.05 Joule. The impactor bounces 4-5 times after the release till it rests on the specimen. The impact machine's software gives acceleration and force in the results. MATLAB software is used to post-process the obtained data. The data is considered till the point where the impactor leaves the specimen when the velocity reaches zero as the specimen damages after the first impact. A total of 250-350 readings are obtained for each specimen tested. The data is transferred to excel sheet to plot the load-displacement graphs. Later, the velocity and mass of the impactor are used as inputs for the FEA (ABAQUS) analysis. The load history, displacement history, velocity history is obtained from the results and are imported into excel sheet to combine with experimental results. The impact test is performed on both sides of the hybrid structure. Specimens 1, 2 and 3 are impacted on the lattice part of the hybrid structure and specimens 4, 5 and 6 are impacted on the solid part of the hybrid structure.

6.5.1 Impact Test on the Lattice Part of Hybrid Structure

6.5.1.1 Displacement History

The acceleration obtained from the experiment is integrated twice with respect to time to get the velocity history of the specimens using MATLAB. The impactor displacement is calculated as it should be similar to the deformation of the ABS lattice

structure and the Kevlar face sheet. The maximum indentation or the displacement is recorded when velocity is zero. The indentation cannot be measured by using Vernier scale because of the elastic behavior of the Kevlar and the lattice structure. Figure 6.16 shows the displacement history of the lattice part of hybrid structure. The maximum deformation observed in the graph is about 9.28 mm which is 46% of the structure height.
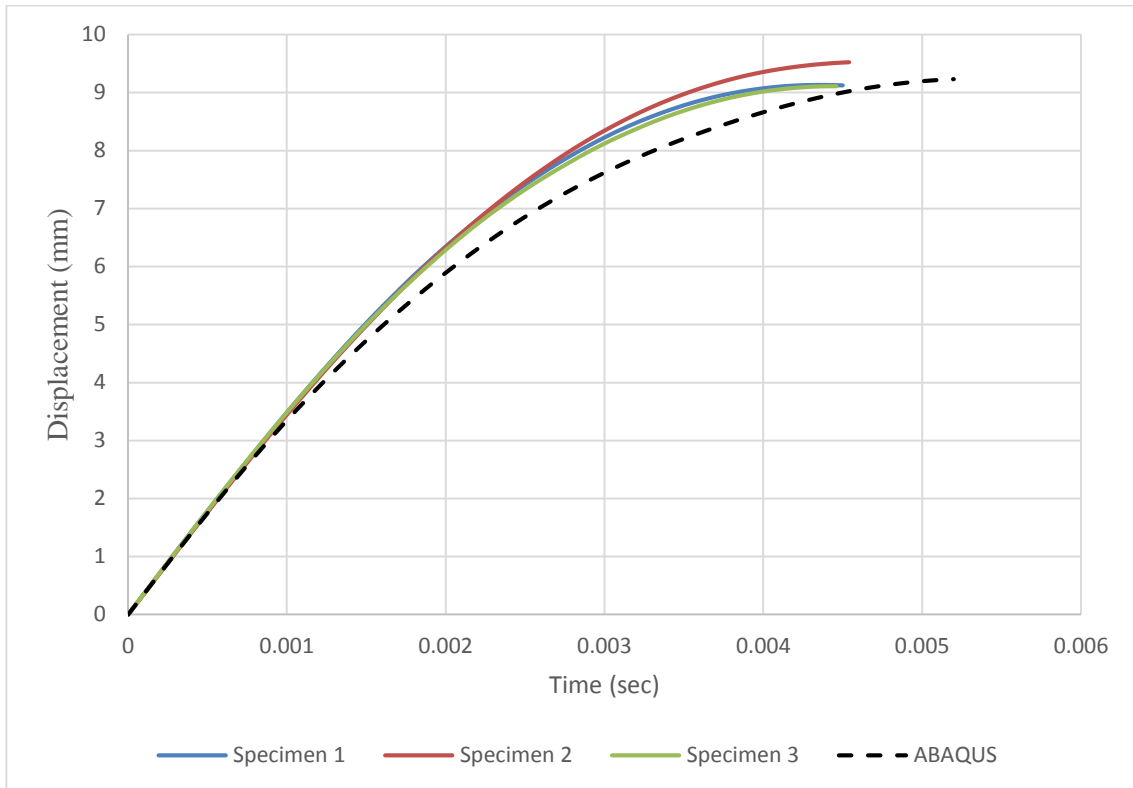
Figure 6.16 Displacement history of the hybrid structure impacted on the lattice part with 14.05 Joules.

6.5.1.2 Velocity History

Velocity history plays a key role in evaluating the maximum displacement of the structure. Figure 6.17 represents the velocity-time graph of the specimens impacted on the lattice part of the hybrid structure. The data generated during experiment showed a good

match for all the three specimens during the impact period. There was a little uncertainty because of the uncontrolled amount of epoxy resin between the lattice and the Kevlar face sheet. The FEA result is comparatively good than the experimental results. The results are slightly deviated due the uncertainty (not firmly fixed) in the toggle clamp boundary conditions.
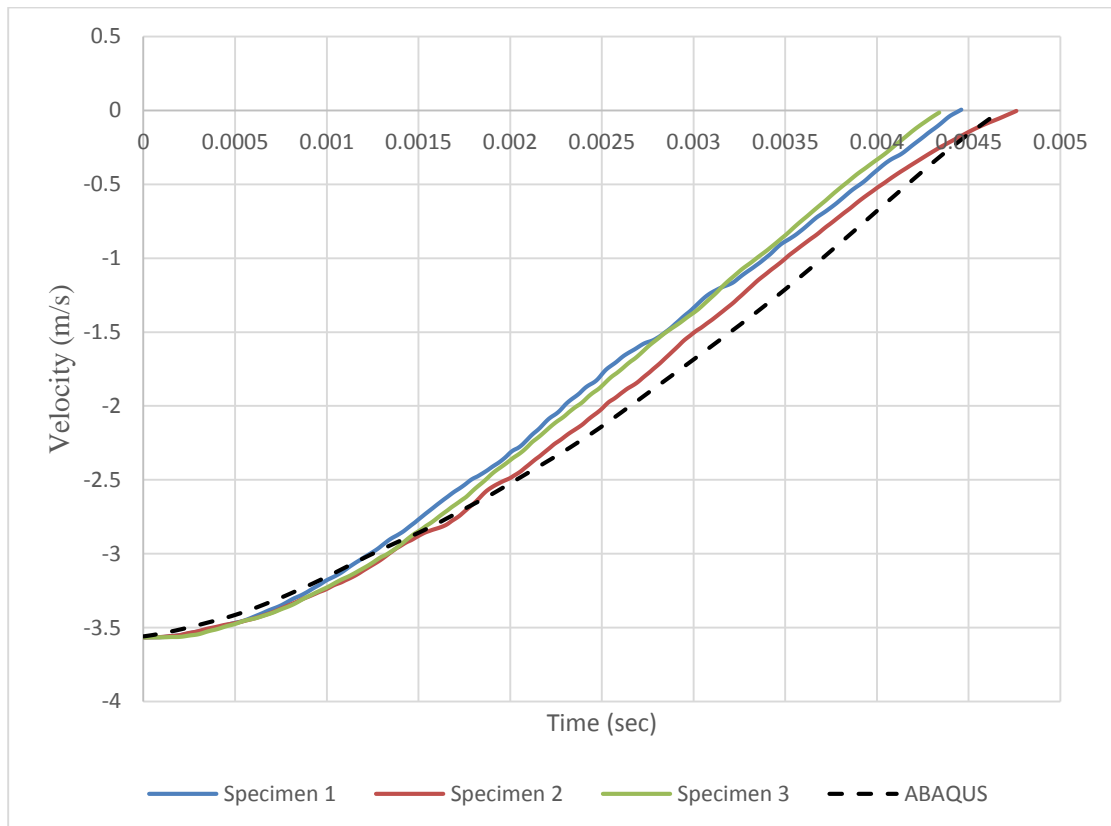
Figure 6.17 Velocity history of the hybrid structure impacted on the lattice part with 14.05 Joules.

6.5.1.3 Force History

The impact machine was installed with four load cells at the base to capture the force history of the impactor. The MATLAB software processes the data obtained from the load cells into a single graph for each test. This data is copied into excel sheet for comparing

the experimental results with the FEA results. The maximum load measured was about 2.7 KN. At this load, plastic deformation occurs in the specimen. The spikes in the Figure 6.18 were caused due to the high sensitivity of the load cells. There is slight deviation in the FEA results when compared with the experimental results.
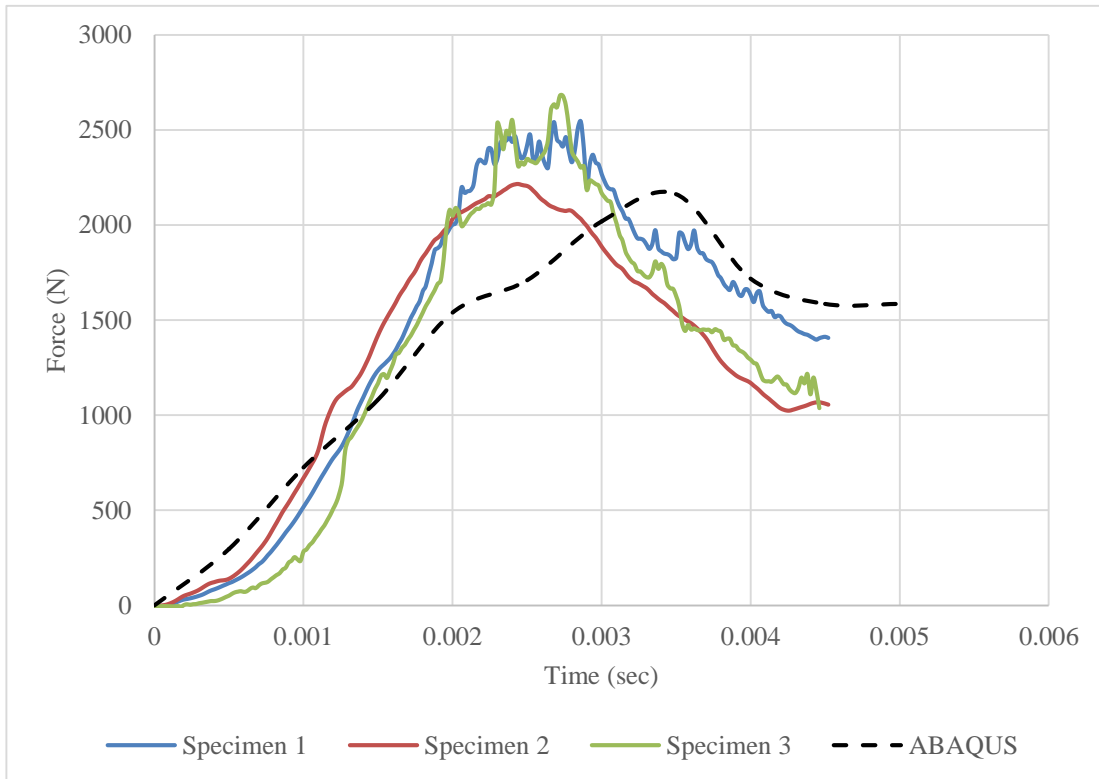
Figure 6.18 Force history of the hybrid structure impacted on the lattice part with 14.05 Joules.

6.5.1.4 Load-Displacement Curve

The load history and the displacement history data is compiled together to obtain the load-displacement curve. The area under the curve gives the amount of energy absorbed by the structure. Figure 6.19 displays the load-displacement curve of the hybrid structure impacted on the lattice part. This impacted side of the structure had less force with high

94

deformation as shown in Figure 6.19. The FEA analysis performed in ABAQUS showed a good approximation of the experimental results. The precision in the results can be increased by decreasing the step time increment. To obtain these results, a mass scale of 1E-07 time increment was used and it took about 6-7 hours for the simulation to run as the structure was complex.
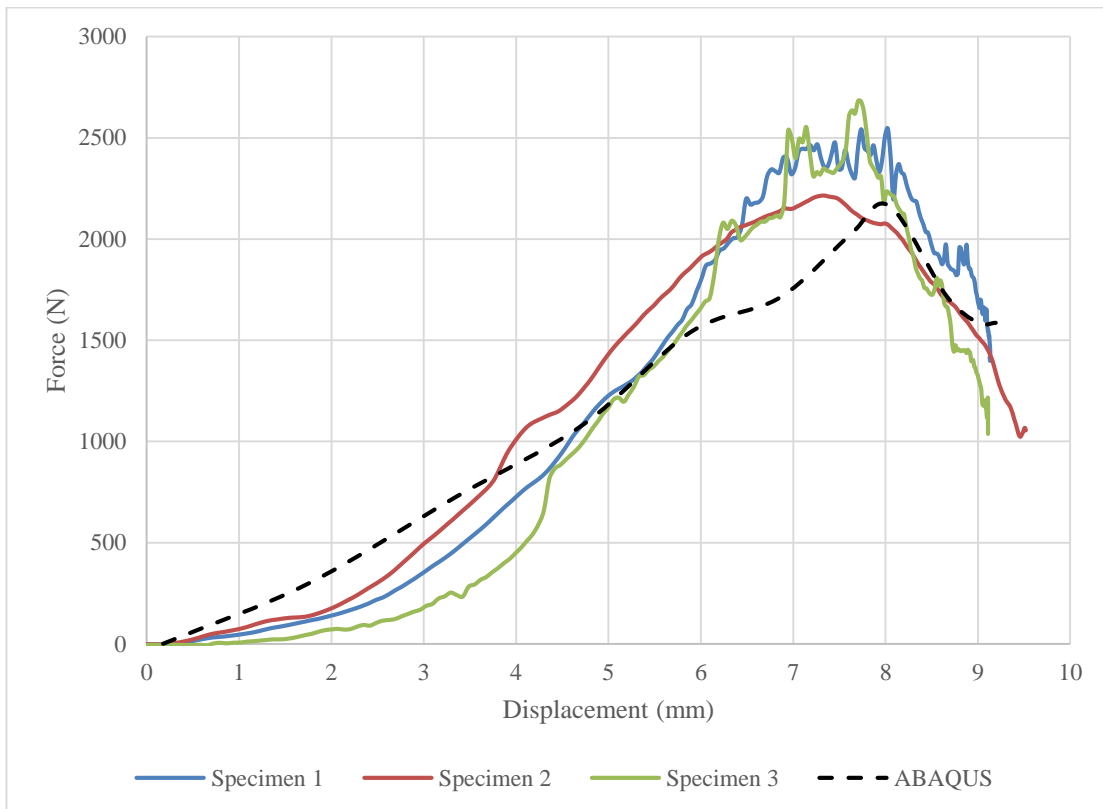
Figure 6.19 Load-displacement curve of the hybrid structure impacted on the lattice part with 14.05 Joules.

6.5.1.5 Absorption Energy History

The energy absorbed by the structure is calculated by integrating the area under the load-displacement curve using a MATLAB code. The absorption energy is plotted against the impact time period. The FEA results are compared with the experimental results by

plotting them using an excel sheet. Figure 6.20 illustrates the total energy vs time of the hybrid structure impacted on the lattice side. The maximum absorbed energy in the experiment and FEA analysis are approximately 10.93 Joules and 10.48 Joules respectively. The FEA result was deviating from the experimental results due to the low impact energy levels. The other reason could be large increment time used for the simulation. The best solution for this inaccuracy could be increasing the energy level which decreases the effect of vibration and friction on the experimental results.
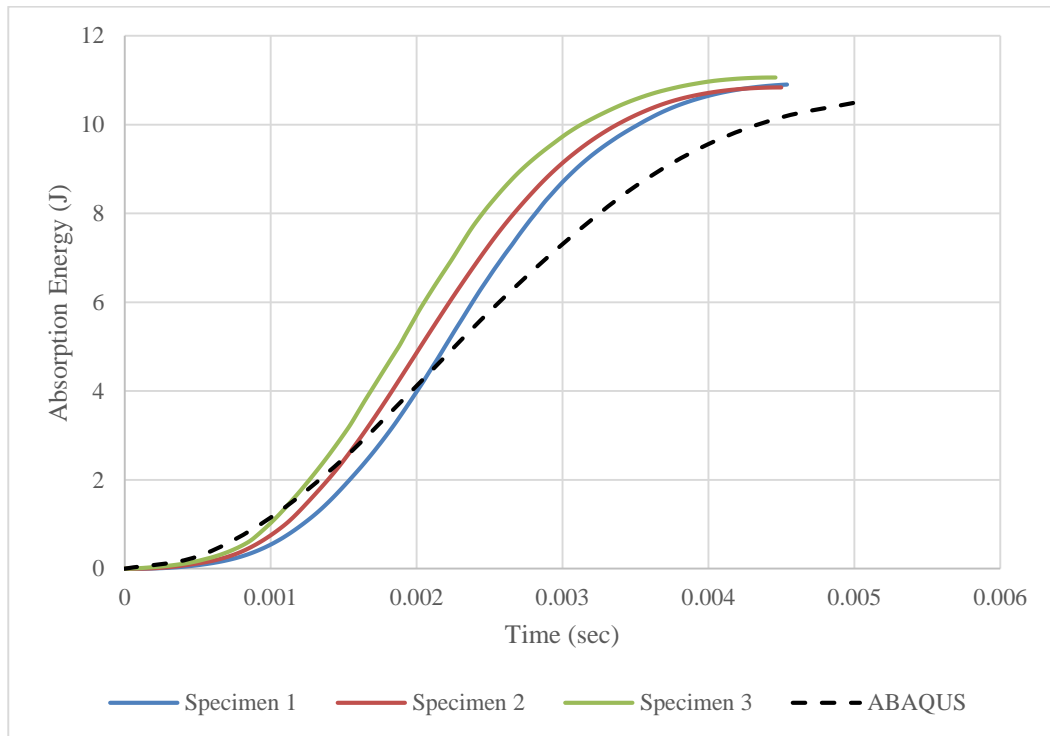
Figure 6.20 Energy absorption vs time curves of the hybrid structure impacted on the lattice side.

6.5.2 Impact Test on the Solid Part of Hybrid Structure

6.5.2.1 Displacement History

The solid part of the hybrid structure is impacted with a velocity of 3.5678 m/s. The accelerometer sensor captures the rate of acceleration of the impactor as it hits the specimen. The data captured during the experiment is post processed in MATLAB. The acceleration is integrated twice with respect to time to achieve the displacement. As the solid part of the hybrid structure is rigid, the impactor bounced 4-5 times. So the final displacement which can be seen is not the actual deformation of the structure. When the velocity of the impactor reaches zero, it can be considered that the first impact is completed. So, the data is transferred to an excel sheet to plot them along with the FEA results for comparison. Figure 6.21 illustrates the experimental results along with ABAQUS results of the amount of deformation in the Specimens 4, 5 and 6. The amount of displacement in the experimented specimens is found to be 7 mm. The FEA analysis deformation is simulated to be 7.32 mm.

The cross-sectional analysis was performed on the experimented specimens as mentioned in the section 4.5 earlier. The beaker was kept at room temperature for about 72 hours. The epoxy resin cured to form a thick transparent solid. The cured specimen was cut into two halves with the help of a band saw machine to see the internal damage of the structure caused by the impact test. Figure 6.22 shows the cross-sectioned image of the impacted hybrid structure. It can be depicted from the Figure 6.22, that the hybrid structure was damaged till the first layer of lattice structure. So, it can be summarized from the observation that due to the 4-5 bounces of the impactor, the total deformation is about 10 mm.
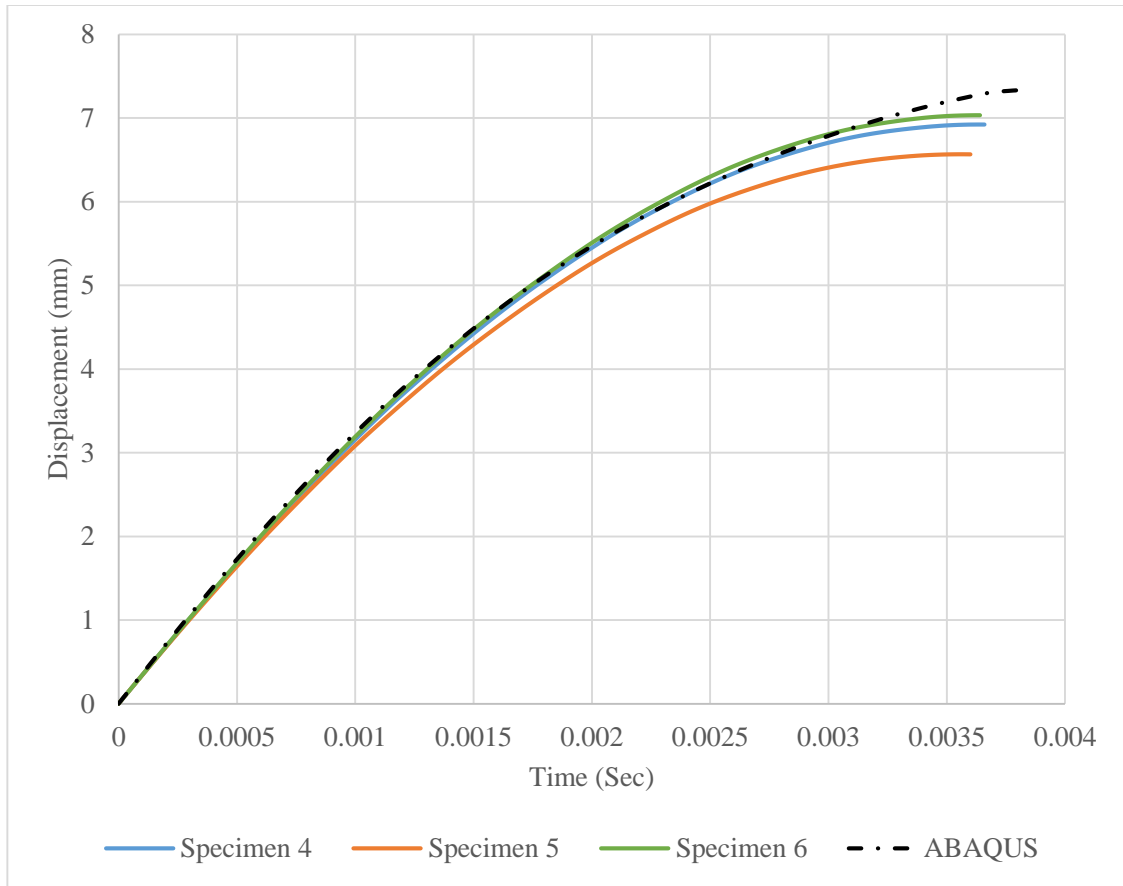
Figure 6.21 Displacement history of the hybrid structure impacted on the solid part with 14.05 Joules energy.
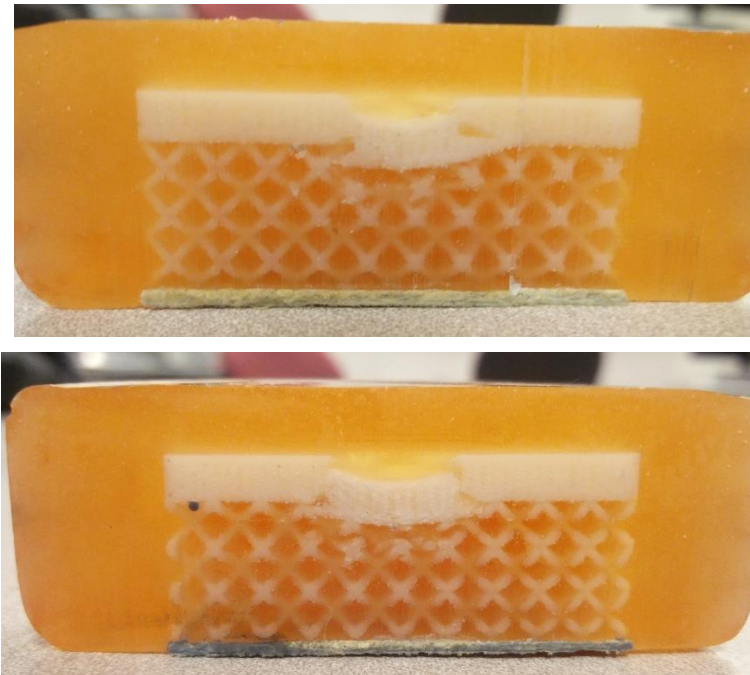
Figure 6.22 Cross-sectioned impact tested specimen embedded in epoxy resin

6.5.2.2 Velocity history

The data captured during the experiment contains only the force and acceleration readings. The calculated velocity of the impactor using the conservation of energy principle is 3.5678 m/s. The first impact is considered to be completed when the velocity of the impactor reaches zero. The acceleration is integrated with respect to time to obtain the velocity using the MATLAB program. This data is transferred to an excel spreadsheet to plot the velocity values against time. The FEA model results are also plotted with the experimental results for comparison. Figure 6.23 illustrates that the FEA and experimental results are approximately same.
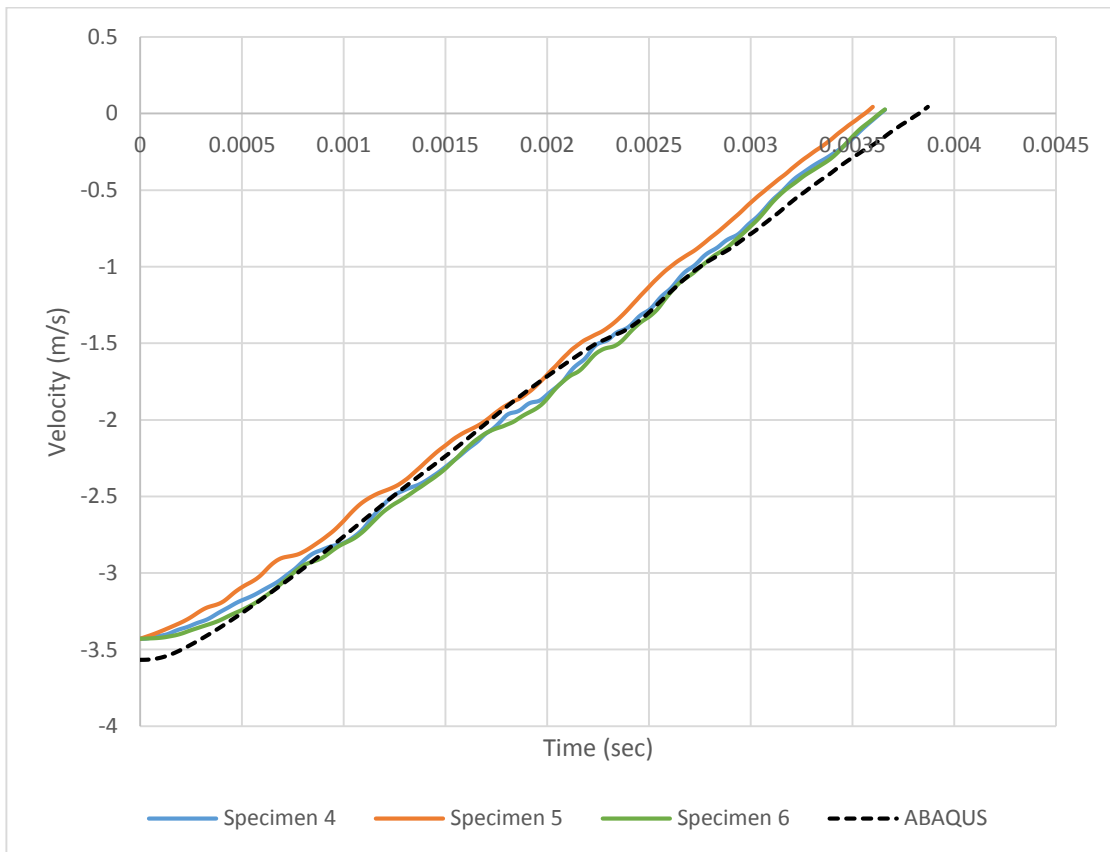
Figure 6.23 Displacement history of the hybrid structure impacted on the solid part with 14.05 Joules energy.

6.5.2.3 Load history

The four load cells installed at the base of the impact test machine are used to capture the force history of the experimented specimens. These sensors are highly sensitive and can capture even the voice vibrations. The data attained from the experiment is post processed in MATLAB. The four load cells give different readings and these readings are combined together to calculate the total impact force. Figure 6.24 depicts the ABAQUS and the experimental force history of the hybrid structure specimens impacted on the solid part. The maximum average force observed in the experiment and FEA results are 4900 N and 4800 N respectively. This deviation can be corrected by decreasing the time increment scale in FEA analysis.
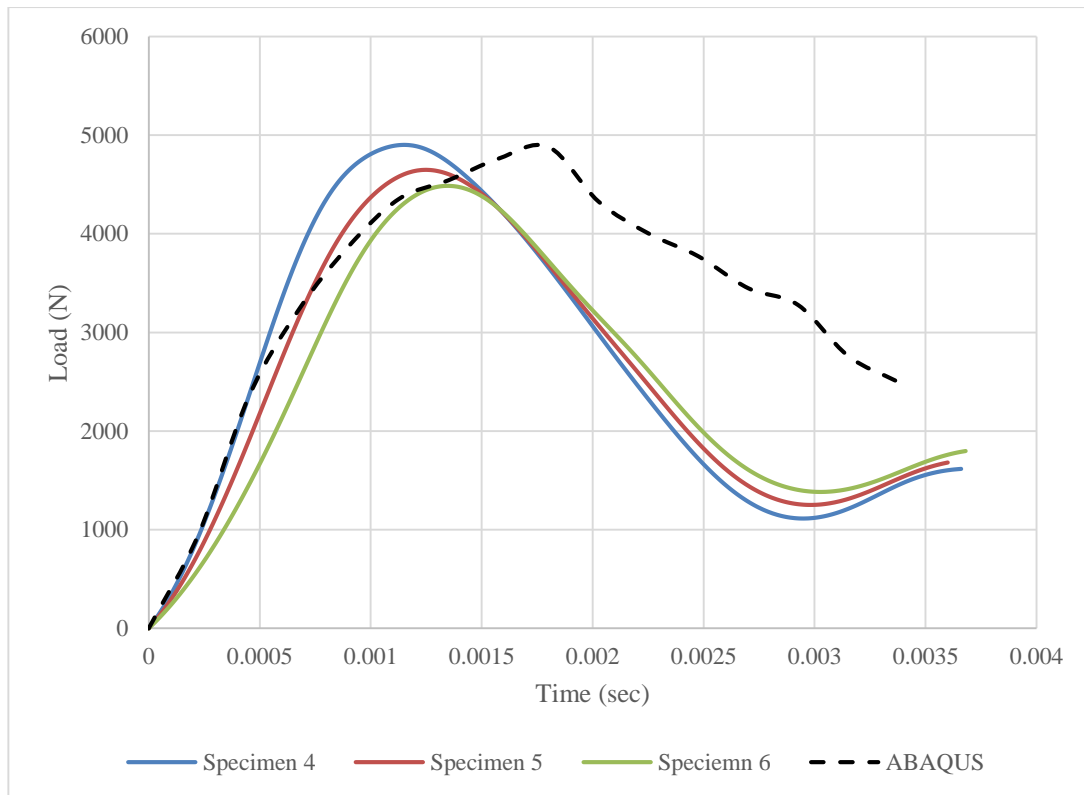
Figure 6.24 Force history of the hybrid structure impacted on the solid part with 14.05 Joules energy.

6.5.2.4 Load vs Displacement history

The y-axis values of the force and displacement histories are copied into a new excel spreadsheet. These readings are plotted together to form the load-displacement curves. The area under the load-displacement curve gives the amount of energy absorbed by the specimen. These specimens could withstand a higher load but less deformation when compared with lattice impacted specimens. Figure 6.25 shows the load-displacement curves of the experimented specimens and the ABAQUS model. There is a little deviation between the experiment and FEA results which can be resolved by decreasing the time increment scale of the FEA analysis.
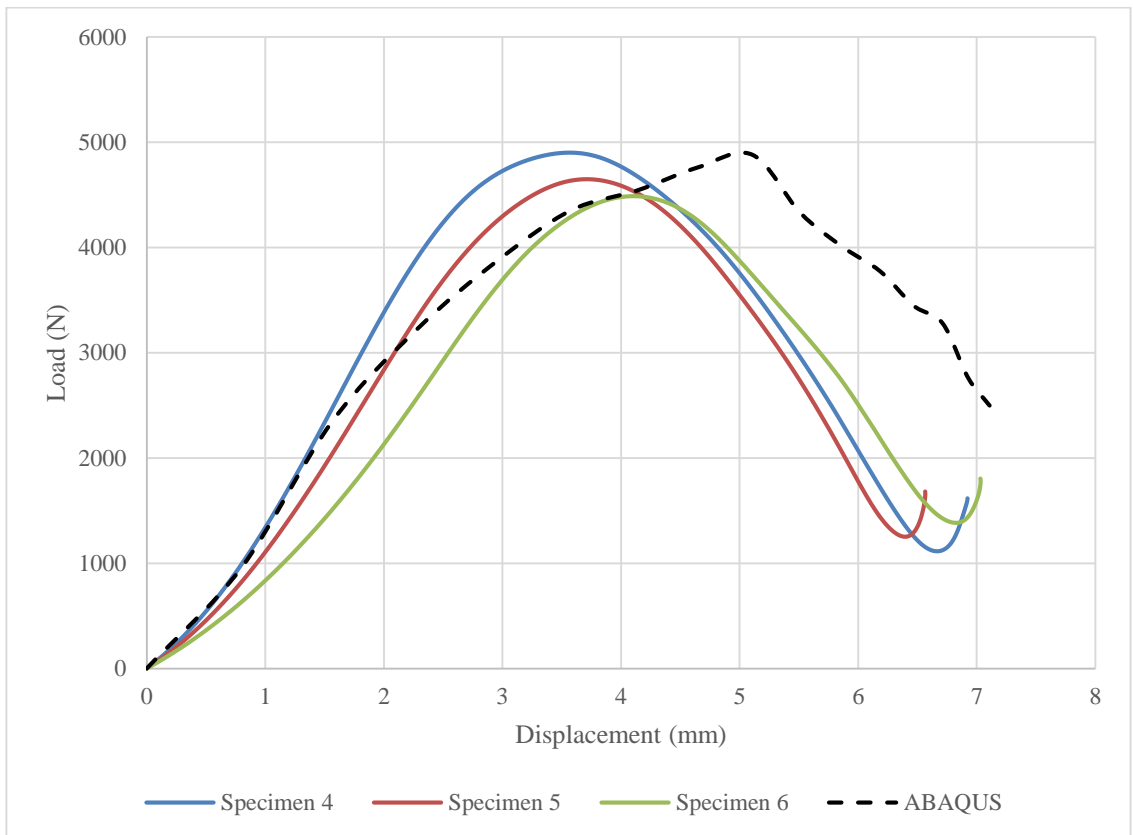
Figure 6.25 Load-displacement history of the hybrid structure impacted on the solid part with 14.05 Joules energy.

6.5.2.5 Absorption Energy history

The energy absorbed by the specimen during the impact is calculated by integrating the area under the load-displacement curve plotted earlier. The absorption energy histories of the impacted specimens are plotted with the help of MATLAB software. These readings are transferred to an excel spreadsheet for plotting these graphs along with the ABAQUS model result. Figure 6.26 shows the combined plots of experiment and ABAQUS analysis results. It can be observed that the experimental results match reasonably well with FEA results. Since the impacted energy level was 14.05 Joule, the specimens have absorbed energy about 13.28 Joules.
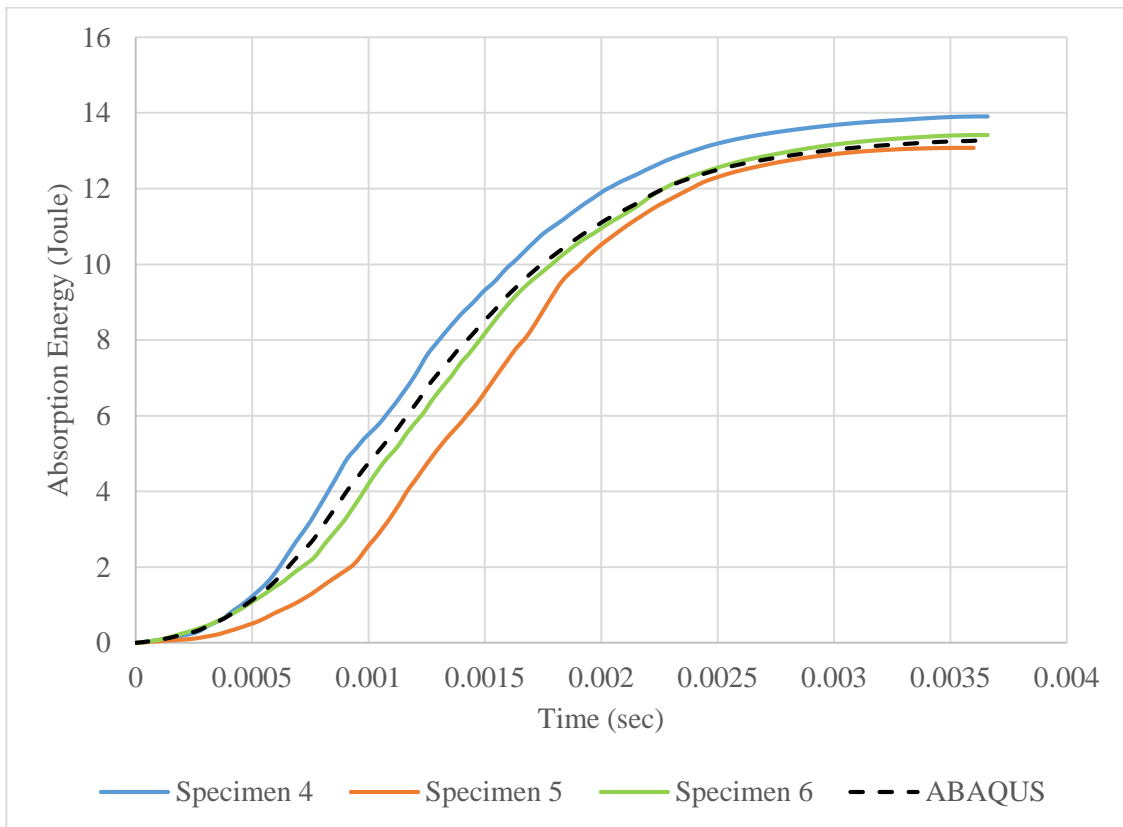
Figure 6.26 Absorption energy history of the hybrid structure impacted on the solid part with 14.05 Joules energy.

The main objective of performing the low-velocity impact test was to observe the amount of indentation in the hybrid structure, so that there will be no damage to the microstrip patch antenna embedded at the solid/lattice interface of the hybrid structure. From the above graphs, the values of the indentations and total energies of the experimented specimens along with the FEA models have been put together in Table 7. There is about nine percent of variation between the experimental and ABAQUS total energies when the lattice part is impacted and in case of the solid part, there is only 1.3% difference between the experimental and ABAQUS total energies. Before testing the specimens impacted on the lattice side, it was observed that some of the struts of unit cells were fabricated with uneven diameter. This error of fabrication could have affected the experimental results.

Table 7 Comparison of the average indentations and the average total energies.

Hybrid structure impacted on	Experimental Indentation (mm)		ABAQUS Indentation (mm)	Experimental Total Energy (J)		ABAQUS Total Energy (J)	Percent of Variation
	9.52			10.90			
Lattice part	9.11	9.28	9.22	10.84	10.93	10.48	4.1%
	9.22			11.06			
	6.92			13.9			
Solid part	6.88	6.94	7.29	13.41	13.46	13.28	1.3%
	7.03			13.07			

For a better comparison between the total energy of experiment and FEA, a bar chart has been plotted, as shown in Figure 6.27.
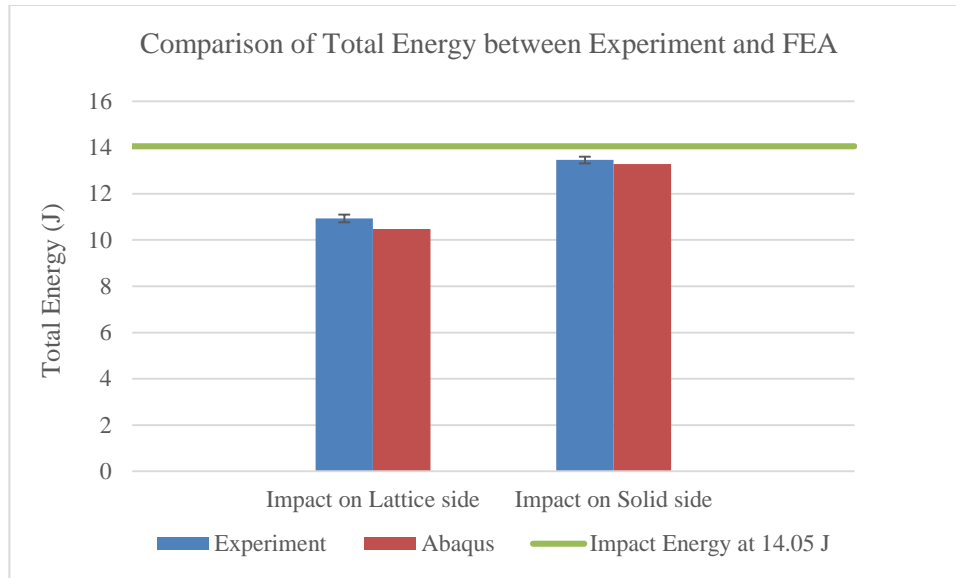
Figure 6.27 Bar chart comparing the total energy of experiment and Abaqus.
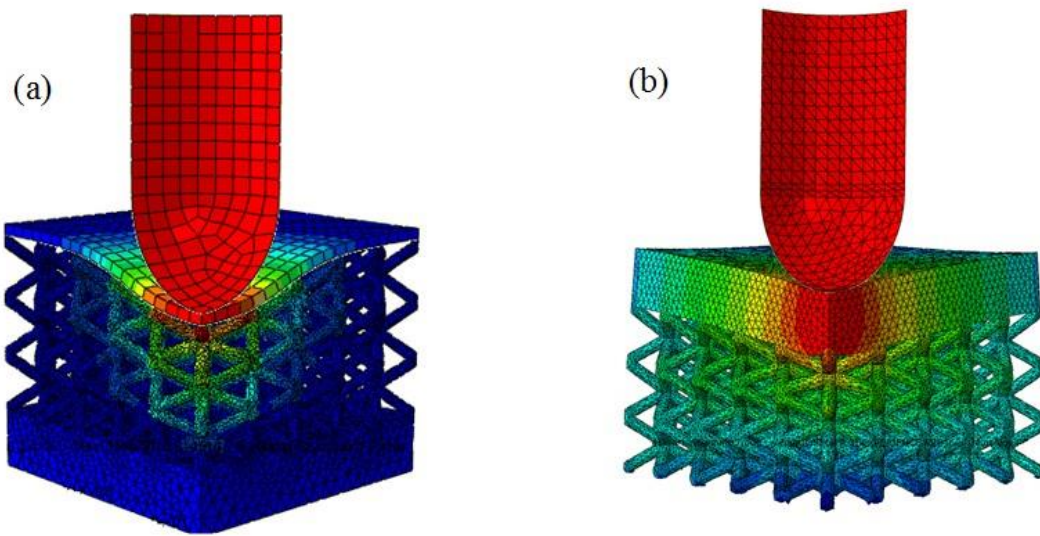
Figure 6.28 ABAQUS displacement results of hybrid structure impacted on (a) Lattice side, (b) Solid side.

CHAPTER 7 : SUMMARY AND CONCLUSION

7.1 Summary

The main objective was to design a mechanical effective structure with good electrical performance (electro-mechanical structure). For this purpose, a model of dimension 50 mm x 50 mm x 5 mm was printed with three different preset fill densities using an extrusion based 3D printer-LulzBot TAZ 5. The operational frequencies of the microstrip patch antennas created on these printed samples were measured using the VNA. 3D X-ray microscopy was performed on the printed samples. This work leverages the RF measurement results and delves deeper into the x-ray images of the dielectric materials to understand the nature of anisotropy both in lateral and thickness direction. The selection of in-fill density only applies to the core region while the top and bottom layers are almost solid. Layering construction of printed substrates and anisotropy introduced in each layer affected antenna response and the extent of their influence was investigated. The simulation models were developed based on permittivity anisotropy in the substrate material. ANSYS-HFSS modeling was adopted to understand the effect of material heterogeneity on RF response. The effect of uniaxial anisotropy in permittivity on patch antenna response was also investigated using ANSYS-HFSS. These results clearly demonstrated the ability to control the dielectric constant of the 3D printed material based on prescribed fill density and can be implemented in the solid part of the hybrid structure based on the application.

Hybrid structure of dimension 50 mm x 50 mm x 20 mm, was fabricated using Stratasys 3D printer and was tested on a low-velocity impact machine (an ASTM Standard D7136) at 14.05J energy level. The structure was impacted on both sides to calibrate the depth of indentation. Cross-sectional analysis was performed on the sample impacted on the solid part to aid in HFSS modeling. The patch antenna was embedded at the interface of the solid and lattice part of hybrid structure. The frequency of the antenna was measured before and after the impact on the both sides of the hybrid structure.

MATLAB code was used to generate the load-displacement graphs, so that the absorption energy of the specimens can be calculated. By considering the above results, an Electro-Mechanical structure with desired properties can be designed and fabricated based on the area of application.

7.2 Conclusion
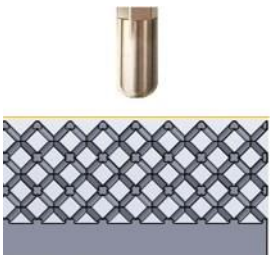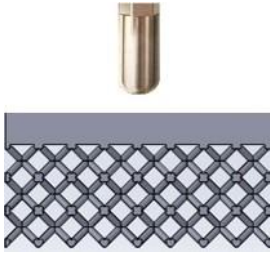
This research aims at developing heterogeneous structures via numerical simulation and experimental testing for electromechanical applications. Specifically, the research relates the use of additive manufacturing process to fabricate electromechanical hybrid substrates whose dielectric property can be controlled by varying the infill density in combination with mechanical elements – (lattice structures in this case).

Additive manufacturing technique allows the construction of orthotropic substrates that can be leveraged to tune an antenna or enhance its overall performance. A three-dimensional nondestructive visualization using X-ray microscope was immensely helpful in quantifying achieved microstructural details for validation of 3D printed geometry and subsequent computational modeling. The relationship between dielectric properties and fill

density for 3D printed ABS substrates has been characterized. The resonant frequencies of microstrip patch antennas created on 3D printed ABS substrates with the core porosity of 66.5%, 45.6%, and 24.7%   were found to be 5.68 GHz, 5.47 GHz, and 5.15 GHz for experimental and 5.61 GHz, 5.37 GHz, and 5.16 GHz for simulation, respectively. In addition, the simulation results show that the thickness direction dielectric properties have pronounced effect on patch antenna resonant frequency, while the lateral direction properties have minimal effects. Thus, it can be concluded that care should be taken in manipulating the thickness direction properties to design a substrate for patch antennas to operate at particular frequencies. Results clearly demonstrate the ability to local control the dielectric constant within a 3D printed substrate based on prescribed fill density. Results calculated from this part research are important to design microstructure of dielectric substrates and tune RF response with desired anisotropy. There is a good agreement between the numerical model and the experimental tests, thus exhibiting a very good reliability of the proposed simulation process.

Mechanical functionality was incorporated by adding a lattice structure to the above discussed model, naming it as hybrid structure. The structure's mechanical robustness was demonstrated by performing a low-velocity impact test at an energy level of 14.05 J. A numerical analysis (ABAQUS) was also performed to match the experimental results. The antenna was embedded at the interface of the solid and lattice part of the hybrid structure. HFSS simulation was carried out to observe the performance of the antenna before and after the impact. The results are shown in Table 8.

Table 8 Experimental Displacement and HFSS simulated resonant frequencies before and after impact on lattice and solid side of hybrid structure

Impacted side	Displacement after impact-Experimental (mm)	Frequency before impact (GHz)	Frequency after impact (GHz)	Note
	9.28	4.17	4.22	The impact load does not affect the resonating frequency of the patch antenna
	6.94	3.56	5.48	Due to the impact on the antenna, the resonating frequency has increased by 53.9%

The hybrid structure concept makes it possible to design embedded antenna structures which are structurally effective for the communicative body panels present in the automobiles and can be extended to aerospace applications, promising an innovative future communication technology.

7.3 Recommendations for Future Work

The present work mainly focuses on developing an electro-mechanical structure. The structure includes a microstrip patch antenna embedded at the interface of solid and lattice part. For designing the lattice structure, BCC unit cell was used.

There are several recommendations for future work in this field of research.

- The band width of the resonant frequency of the microstrip antenna can be analyzed by varying the dimensions of the antenna.

- Slots and connecting paths can be created in the solid part of hybrid structure for embedding the sensors.

- In the HFSS analysis, the solution frequency can be varied to observe the resonating frequency. Optimization of the results can be done with the help of ANSYS workbench.

- The printer parameters like printing speed, layer height can be varied to match the machine preset fill density. The printing direction and orientation of the samples can be varied to observe their energy absorption behavior.

- Instead of using a regular BCC unit cell, the lattice structure can be strengthened by adding alternative struts in between four layers, or by using a lattice structure that has good absorption energy than BCC structure. Other materials can also be investigated.

- The impact machine used for this research can be modified for higher impact energy levels, reduce the friction of the sliding bars. The boundary conditions of the impact machine can be modified to reduce the delamination of the Kevlar face sheets.

- It is also recommended to do Multiphysics modeling, specifically, modeling the RF response of the antenna before and after impact. The antenna response can be modeled on a composite dielectric structure. The FEA modeling can be done using software like LS-DYNA, Hyper mesh and NASTRAN. Topology optimization can be investigated for constructing a structure which absorbs relatively more energy.

REFERENCES

[1] D. P. D. Dr. S.A. Patil, "Electronics For You," [Online]. Available: http://electronicsforu.com/technology-trends/microstrip-antenna-applications. [Accessed 25 September 2017].

[2] A. S. M. M. M. a. S. P. Joshua, "Design & Optimization of Microstrip Patch Antenna Case," *International Journal of Emerging Trends & Technology in Computer Science ,* vol. 2, no. 5, pp. 139-141, 2013.

[3] M. Brandt, Laser Additive Manufacturing : Materials, Design, Technologies, and Appilcations, Australia: Elsevier Science & Technology, 2016.

[4] L. M. A. Gibson, Cellular Solids: Structure and Properties, Cambridge: Cambridge University Press, 1997.

[5] T. M. A. C. Noel Tessier, "Engineered Syntactic Systems," [Online]. Available: http://esyntactic.com/products-solutions/syntactic-buoyancy-materials/macrosphere-syntactic-foam/. [Accessed 28 September 2017].

[6] "Wikipedia," [Online]. Available: https://en.wikipedia.org/wiki/Crystal_structure. [Accessed 28 September 2017].

[7] B. V. Zeghbroek, "Principles of Semiconductor Devices," 2011. [Online]. Available: https://ecee.colorado.edu/~bart/book/book/chapter2/ch2_2.htm. [Accessed 28 September 2017].

[8]   A. A. a. M. Pumera, "3D-printing technologies for electrochemical applications," *Chem. Soc. Rev. ,* vol. 45, pp. 2740-2755, 2016.

[9]   "Explore Additive 3D Modelling / 3D Printing," January 2007. [Online]. Available: http://www.arch.virginia.edu/arch549/assignments/Project_2-3Dprint.pdf. [Accessed 5 September 2017].

[10] D. W. R. a. B. S. I. Gibson, Additive manufacturing technologies, Springer, 2010.

[11] "3D HUBS," [Online]. Available: https://www.3dhubs.com/what-is-3d-printing#technologies. [Accessed 11 September 2017].

[12] "Omnia (CS)," [Online]. Available: http://www.omnia-cs.co.uk/sandwich-panels/panels-overview. [Accessed 29 September 2017].

[13] J.-J. DeLisle, "Microwaves and RF," 10 November 2014. [Online]. Available: http://www.mwrf.com/software/what-are-differences-between-various-em-simulation-numerical-methods. [Accessed 1 October 2017].

[14] A. (Ansoft)-HFSS, "An Introduction to HFSS: Fundadmental Principles, Concepts, and Use," 2009. [Online]. Available: http://e-science.ru/sites/default/files/upload_forums_files/8u/HFSSintro.pdf. [Accessed 5 May 2016].

[15] J. F. a. T. Belytschko, A First Course in Finite Elements, Wiley, 2007.

[16] "Dassault Systems," 2002-2017. [Online]. Available: https://www.3ds.com/products-services/simulia/products/abaqus/abaqusexplicit/. [Accessed 14 October 2017].

[17] S. N. C. C. W. W. G. a. V. J. C. Zhang, "Novel 3D Printed Synthetic Dielectric substrates," *Microwave and Optical Technology Letters,* vol. 57, no. 10, pp. 2344-2346, 2015.

[18] V. S. Tummala, A. Mian, N. H. Chamok, M. Ali, J. Clifford and P. Majumdar, "3D Printed Porous Dielectric Substrates for RF Applications," *ASME International Mechanical Engineering Congress and Exposition,* vol. 10, p. ASME. 50640, November 2016.

[19] F. Yang, X.-X. Zhang, X. Ye and Y. Rahmat-Samii, "Wide-band E-shaped patch antennas for wireless communications," *IEEE Transactions on Antennas and Propagation ,* vol. 49, no. 7, pp. 1094-1100, 2001.

[20] K. F. L. F. Y. A. E. Ahmed Khidre, "Wideband Circularly Polarized E-Shaped Patch Antenna for Wireless Applications," *IEEE Antennas and Propagation Magazine ,* vol. 52, no. 5, pp. 219-229, 2010.

[21] F. B. A. K. Yamina Tighilt, "Modeling and design of printed antennas using neural networks," *International jounal RF and Microwave Computer-Aided-Engineering,* vol. 21, pp. 228-233, 2011.

[22] S. D. a. N. H. D. M. Pozar, "A comparison of commercial software packages for microstrip antenna analysis," *IEEE Antennas and Propagation Society International Symposium,* vol. 1, pp. 152-155, 2000.

[23] G. A. Deschamps, "Microstrip Microwave Antennas," in *Third USAF Symposium on Antennas*, 1953.

[24] H. G. a. G. Baissinot, "Flat Aerial for Ultra High Frequencies". French Patent 703 113, 1955.

[25] R. Garg, Microstrip Antenna Design Handbook, India: Artech House, 2001.

[26] K. F. L. a. K.-F. Tong, Microstrip Patch Antennas, Singapore: Springer Science+Business Media Singapore, 2015.

[27] S. D. R. W. Lo Y, "Theory and experiment on microstrip antennas," *IEEE Trans Antennas Propag,* vol. 27, no. 2, pp. 137-145, 1979.

[28] G. F. Mosig J, "General integral equation formulation for microstrip antennas and scatterers.," *IEEE Proc H Microwaves Antennas Propag ,* vol. 132, no. 7, pp. 424-432, 1985.

[29] L. K. Dahele JS, "Theory and experiment on microstrip antennas with airgaps.," *IEE Proc H Microwaves Antennas Propag,* vol. 132, no. 7, pp. 455-460, 1985.

[30] C. A. Balanis, Antenna Theory: Analysis and Design, John Wiley & Sons, February 2016.

[31] M. E. W. R. Lopes AJ, "Integrating stereolithography and direct print technologies for 3D structural electronics fabrication.," *Rapid Prototyp J,* vol. 18, pp. 129-143, 2012.

[32] J. B. N. C. K. B. A. C. G. E. F. M. F. W. R. Palmer JA, "Mesoscale RF relay enabled by integrated rapid manufacturing," *Rapid Prototyp J,* vol. 12, pp. 148-155, 2006.

[33] M. F. E. C. Wicker R.B, "Multiple material microfabrication: extending stereolithography to tissue engineering and other novel applications," *15th Annual Solid Freeform Fabrication Symposium,* pp. 754-764, 2-4 August 2004.

[34] M. D. M. F. M. E. W. R. Castillo S, "Electronics integration in conformal substrates fabricated with addtive layered manufacturing," *Proceedings of the 20th Annual Solid Freeform Fabrication Symposium,* pp. 730-737, 2009.

[35] S. R. H. G. M. D. O. R. M. E. I. M. W. R. C. K. N. M. Z. B. Gutierrez C, "CubeSat fabrication through additive manufacturing and micro dispensing," in *International Microelectronics Assembly and Packaging Society Symposium*, 2011.

[36] M. E. Wicker RB, "Multi-material, multi-technology stereolithography," *Virtual Phys Prototyp,* vol. 7, pp. 181-194, 2012.

[37] D. W. M. ,. M. R. B. W. David Espalin, "3D Printing multifunctionality: structures with electronics," *International Journal For Additive Manufacturing Technology,* vol. 72, pp. 963-978, 2014.

[38] F. U. a. GregoryK., "Modelling and simulation of delamination in fibrous composite panels under low velocity impact from variable shape impactors," *European Journal of Scientific Research ,* vol. 4, no. 25, pp. 638-648, 2009.

[39] F. U. a. G. K., " Computational modelling and simulation of low velocity impact on fibrous composite panels drop-weight un-partitioned model," *ARPN J of Eng & Appl Sci ,* vol. 2, no. 4, 2009.

[40] A. S, Impact on composite structures, Cambridge: Cambridge University Press, 1999.

[41] C. G, "Modelling of impact damage in composite laminates.," *Composites,* vol. 20, no. 3, pp. 209-214, 1989.

[42] S. Q. a. K. M. Fan XL, "Review of damage tolerant analysis of laminated composites," *Journal of Solid Mechanics,* vol. 2, no. 3, pp. 275-289, 2010.

[43] NASA/TP-2000-210481, "A comparison of quasi-static indentation to low velocity impact," *NASA Reference Publication,* 2000.

[44] U. F. a. P. Myler, "Finite element simulation of damage and failure predictions of relatively thick carbon fiber-reinforced laminated composite panels subjected to flat and round noses low velocity drop-weight impact," *Thin-Walled Structures,* vol. 104, pp. 82-105, 2016.

[45] V. R. &. D. D. Ursenbach DO, "An engineering model for deformation of carbon fibre reinforced composite plates during penetration," *Composite Structures,* vol. 32, pp. 197-202, 1995.

[46] B. A. &. S. J. Nyman T, " Equivalent damage and residual strength for impact damaged composite structure," *J Reinforced Plastics and Compos,* vol. 19, no. 6, pp. 428-448, 2000.

[47] F. U. a. G. K, "Simulation of progressive failure prediction of filament wound composite tubes subjected to multiple loading with membrane-flexion coupling effects," *ARPN J of Eng & Appl Sci (ISSN 1819-6608),* vol. 4, no. 5, pp. 75-85, 2010.

[48] V. 6. ABAQUS, "Abacus analysis user's manuals," Dassault Systems, Rising Sun Mills, 166 Valley Street, Providence, USA..

[49] C. K. J. R. N. E. Pongsak Nimdum, "Low velocity impact responses and impact-induced damages on steel cord-rubber composite," in *15TH EUROPEAN CONFERENCE ON COMPOSITE MATERIALS*, Venice, Italy, 24-28 June 2012.

[50] V. S. D. a. N. A. F. L. St-Pierre, "The low velocity impact response of sandwich beams with a corrugated core or a Y-frame core," *International journal for Mech. Sci.,* vol. 91, pp. 71-80, 2015.

[51] "LulzBot," Aleph Objects, Inc., [Online]. Available: https://www.lulzbot.com/store/printers/lulzbot-taz-5. [Accessed 14 June 2016].

[52] S. M. M. O. D. R. S. a. W. P. K. Ahn, "Anisotropic material properties of fused deposition modeling ABS," *Rapid Prototyping Journal,* vol. 8, no. 4, pp. 248-257, 2002.

[53] "LulzBot," Aleph Objects, Inc, [Online]. Available: https://www.lulzbot.com/cura. [Accessed 6 July 2016].

[54] W. C. R. M. a. Y. L. Y. Shen, "Low-velocity impact performance of lattice structure core based sandwich panels," *J. Compos. Mater.,* vol. 48, no. 25, pp. 3153-3167, 2014.

[55] "Support Cleaning Apparatus," PADT, [Online]. Available: https://www.padtinc.com/supportremoval/. [Accessed 06 May 2017].

[56] Hexcel, "Resin Systems for Advanced Composites," 1996. [Online]. Available: http://hexcel.com/user_area/content_media/raw/F161_us.pdf. [Accessed 16 January 2017].

[57] M. J. Al Rifaie, "OhioLINK," [Online]. Available: https://etd.ohiolink.edu/pg_10?0::NO:10:P10_ACCESSION_NUM:wright1502760 172343413. [Accessed 29 September 2017].

[58] J. C. M. K. H. M. H. D. D. A. G.-S. M. C. W.-C. S. Y. R. J. M. A. a. v. B. J. A. Da Silva, "Assessment of the 3-D pore structure and individual components of preshaped catalyst bodies by X-Ray imaging," *ChemCatChem,* vol. 7, no. 3, pp. 413-416, 2015.

[59] A. a. G. S. Akbari, "Bioaccessible Porosity in Soil Aggregates and Implications for Biodegradation of High Molecular Weight Petroleum Compounds," *Environ. Sci. Technol.,* vol. 49, no. 24, pp. 14368-14375, 2015.

[60] C. Zeiss, "3D X-ray Microscopy," March 2015. [Online]. Available: https://www.zeiss.com/content/dam/Microscopy/us/download/pdf/Products/X-Ray/xraymicroctdigital.pdf. [Accessed 7 October 2017].

[61] C. Zeiss, "wikimedia," Wikimedia Commons, [Online]. Available: https://commons.wikimedia.org/wiki/File:ZEISS_Xradia_520_Versa_X-ray_microscope_(12286854824).jpg. [Accessed 12 October 2017].

[62] T. a. N. C. Srisuji, "Analysis on microstrip patch antennas for wireless communication," in *2nd Int. Conf. Electro. Commun. Syst., no. Icecs*, 2015.

[63] C. T. M. M. a. H. W. You, "Multilayer Effects on Microstrip Antennas for Their Integration with Mechanical Structure," *IEEE Transactions Antennas Propagation,* vol. 55, no. 4, pp. 1051-1058, 2007.

[64] N. H. A. M. A. T. a. W. S. J. Chamok, "Ultra-Thin UHF Broadband Antenna on a Non-uniform Aperiodic (NUA) Meta-surface," *IEEE Antennas and Propagation Magazine,* vol. 57, no. 02, pp. 167-180, 2015.

[65] A. D7136, "Standard Test Method for Measuring the Damage Resistance of a Fiber-Reinforced Polymer Matrix Composite to a Drop-Weight Impact Event," *Analysis,* vol. i, no. C, pp. 1-16, 2005.

[66] A. J. Turner, "LOW-VELOCITY IMPACT BEHAVIOR OF SANDWICH PANELS WITH 3D PRINTED POLYMER CORE STRUCTURES," Ohiolink.etd, Dayton, 2017.

[67] S. J. Y.-C. Y. Y.-B. L. C.-Y. a. G. J.-G. Gai, "Design of a Novel Microstrip-Fed Dual-Band Slot Antenna for WLAN Applications," *Progress In Electromagnetics Research Letters,* vol. 13, pp. 75-81, 2010.

[68] . S. B. C. A. a. B. C. R. Reese, "Design of a stacked microstrip patch antenna using HFSS," in *IEEE International Symposium on Antennas and Propagation and USNC/URSI National Radio Science Meeting, APSURSI*, North Charleston, SC, 2009.

[69] C. C. N. G. W. C. Vardaxoglou, "Antennas on quasi synthetic media," *Applied Physics A,* vol. 115, no. 2, pp. 605-611, May 2014.

[70] W. G. W. a. J. C. V. Chinwe C. Njoku, "Microstrip Patch Antennas With Anisotropic and Diamagnatic Synthetic Heterogeneous Substrates," *IEEE TRANSACTIONS ON ANTENNAS AND PROPAGATION,* vol. 63, no. no. 7, pp. 1-6, JULY 2015.

[71] A. Sihvola, "Mixing Rules with Complex Dielectric Coefficients," *Subsurface Sensing Technologies and Apllications,* vol. 1, no. 4, pp. 393-415, 2000.

[72] N. A. M. J. Z. D. B. W. T. a. A. M. Bishop, "A Broadband High-Gain Bi-Layer LPDA for UHF Applications," *IEEE Transactions on Antennas and Propagation,* vol. 63, no. 5, pp. 2359-2364, 2015.

APPENDIX

The MATLAB code used for interpreting the impact machine's experimental data is mentioned below. The code generates the load history, velocity history, acceleration history, absorption energy history, displacement history and force history.

```matlab
% clc
% clear all
% close all
format long
% Custom
file1 = 'bcc_1';
f_S = 50000; % frequency of Strain Gauges(Hz)
% Reference
items_ACC1 = {'cDAQ1Mod2_ai0'};
items_LC1 = {'cDAQ1Mod1_ai0'};
items_LC2 = {'cDAQ1Mod1_ai1'};
items_LC3 = {'cDAQ1Mod1_ai2'};
items_LC4 = {'cDAQ1Mod1_ai3'};
% Upfront - Acceleration TMDS Funcion was provided by:Dr. Ryan Merritt at Ahmic Aerospace
Solutions
filePath1 = 'Acceleration.tdms';
addpath('TMDS_function')
params = {...
 'UTC_DIFF' -5 ...%Refer timestamps to U.S. Central Time (UTC - 6)
 'USE_INDEX' false ... %index may be corrupted, use tdms file, not tdms_index
 'MAX_NUM_OBJECTS' 1100 ... %We have about 1000 objects, +100 for padding
 'DATE_STR_FORMAT' 'dd-mmm-yyyy' ... %Only return data info for properties
 %NOTE: timestamp data is returned in such a format that datestr()works
 %on it
 };
% BREAK RUN APART
name1 = strcat('RAW\',file1,'\',filePath1);
filePath = name1;
tempOutput = TDMS_readTDMSFile(filePath,params{:});
output = TDMS_dataToGroupChanStruct_v1(tempOutput);
list = fieldnames(output);
filename = char(list{2});
filename = filename(1:23);
c2 = cellstr(filename);
ACC1 = output.(list{2}).(items_ACC1{1}).data;
% Upfront - Force
```

```matlab
filePath1 = 'Force_(IEPE).tdms';
addpath('TMDS_function')
params = {...
 'UTC_DIFF' -5 ...%Refer timestamps to U.S. Central Time (UTC - 6)
 'USE_INDEX' false ... %index may be corrupted, use tdms file, nottdms_index
 'MAX_NUM_OBJECTS' 1100 ... %We have about 1000 objects, +100 forpadding
 'DATE_STR_FORMAT' 'dd-mmm-yyyy' ... %Only return data info forproperties
 %NOTE: timestamp data is returned in such a format that datestr()works
 %on it
 };
% BREAK RUN APART
name1 = strcat('RAW\',file1,'\',filePath1);
filePath = name1;
tempOutput = TDMS_readTDMSFile(filePath,params{:});
output = TDMS_dataToGroupChanStruct_v1(tempOutput);
list = fieldnames(output);
filename = char(list{2});
filename = filename(1:23);
c2 = cellstr(filename);
LC1 = output.(list{2}).(items_LC1{1}).data;
LC2 = output.(list{2}).(items_LC2{1}).data;
LC3 = output.(list{2}).(items_LC3{1}).data;
LC4 = output.(list{2}).(items_LC4{1}).data;
% SOLVE
MA = 10001;
l1 = length(LC1);
t1 = 0:1/f_S:l1/f_S-1/f_S;
t2 = 0:1/f_S:l1/f_S-1/f_S;
LC_sum = LC1 + LC2 + LC3 + LC4;
% ISOLATE Impact
acc_interval1 = 9.1405;
acc_interval2 = 9.1875;
delta_t = acc_interval2-acc_interval1;
lc_interval1 = 9.1502;
lc_interval2 = lc_interval1+delta_t;
a = lc_interval1*f_S;
b = lc_interval2*f_S;
c = acc_interval1*f_S;
d = acc_interval2*f_S;
t2 = t2(c:d);
t1 = t1(a:b);
lt=length(t1);
t3 = 0:1/f_S:lt/f_S-1/f_S;
LC_sum = LC_sum(a:b);
ACC1 = ACC1(c:d);
% filter accelleration
n = 6; % Filter Order
f1 = 1001; % low frequency
wn = f1/(f_S/2); % Normalized cutoff frequency (Wn = 1 is half ofsample Hz)
[b1,a1] = butter(n,wn,'low');
f_ACC1 = filtfilt(b1,a1,ACC1);
% filter load
n = 2; % Filter Order
```

```matlab
f1 = 700; % low frequency
wn = f1/(f_S/2); % Normalized cutoff frequency (Wn = 1 is half ofsample Hz)
[b1,a1] = butter(n,wn,'low');
f_LC_sum = filtfilt(b1,a1,LC_sum);
% CALCULATE - VELOCITY/DISPLACEMENT
%without filtering
ACC1g = ACC1*32.2;
ACC1_vel = cumtrapz(t2, ACC1g); %Adjust Velocity to Zero Axis
% Shift Velocity
ACC1_vel = ACC1_vel-11.25;
ACC1_disp = -12*cumtrapz(t2, ACC1_vel);
% Plot Load
figure(1)
set(gca,'FontSize',12)
hold on
h = plot(t3,LC_sum,'bl','LineWidth',2);
h = plot(t3,f_LC_sum,'g','LineWidth',2);
legend('Raw Data','700-Hz Filter')
ylabel('Force (lbf)','fontsize',14);
xlabel('Time (sec)','fontsize',14);
grid on;
% Plot Acceleration
figure(2)
hold on
h = plot(t3,ACC1,'bl','LineWidth',2);
h = plot(t3,f_ACC1,'g','LineWidth',2);
ylabel('Acceleration (g)')
xlabel('Time (sec)');
grid on;
% Plot Velocity
figure(3)
hold on
h = plot(t3,ACC1_vel,'bl','LineWidth',2);
ylabel('Velocity (ft/s)')
xlabel('Time (sec)');
grid on;
% Plot Displacement
figure(4)
hold on
h = plot(t3,ACC1_disp,'bl','LineWidth',2);
ylabel('Displacement (in)')
xlabel('Time (sec)');
grid on;
% Plot Load vs Displacement
figure(5)
hold on
h = plot(ACC1_disp,LC_sum,'bl','LineWidth',2);
h = plot(ACC1_disp,f_LC_sum,'g','LineWidth',2);
xlabel('Displacement (in)')
ylabel('load (lbf)','FontSize',14);
grid on;
% Absorption Energy
A_E = cumtrapz(ACC1_disp, LC_sum)/12;
max_AE = max(A_E);
```
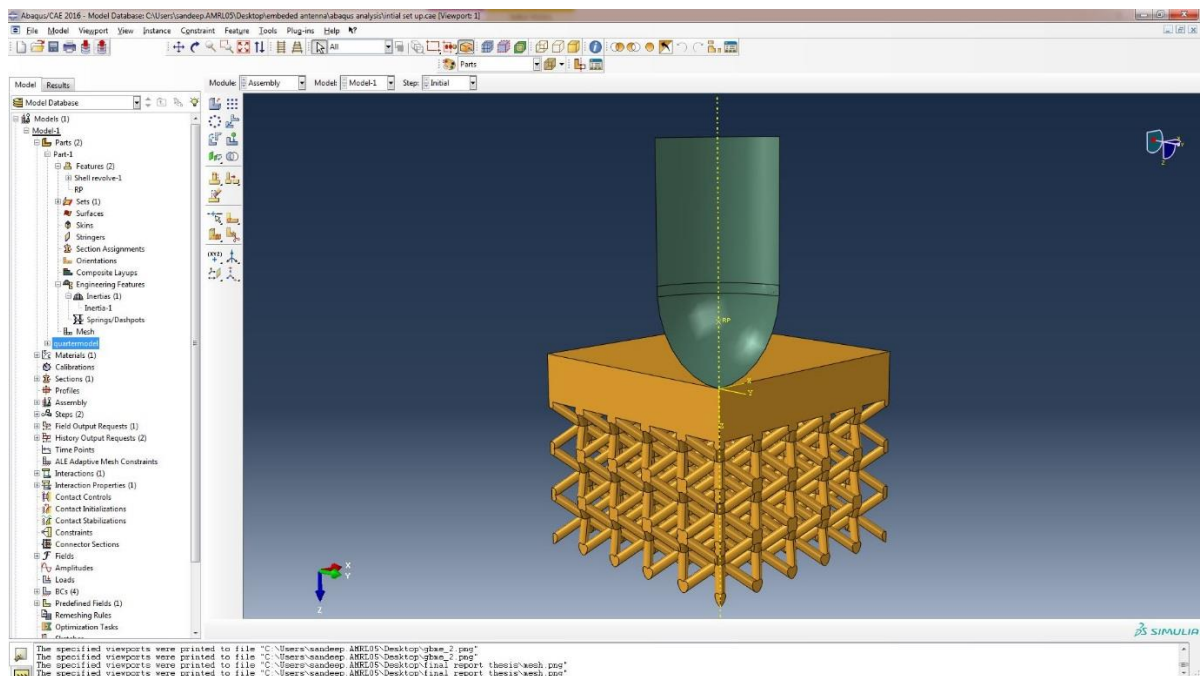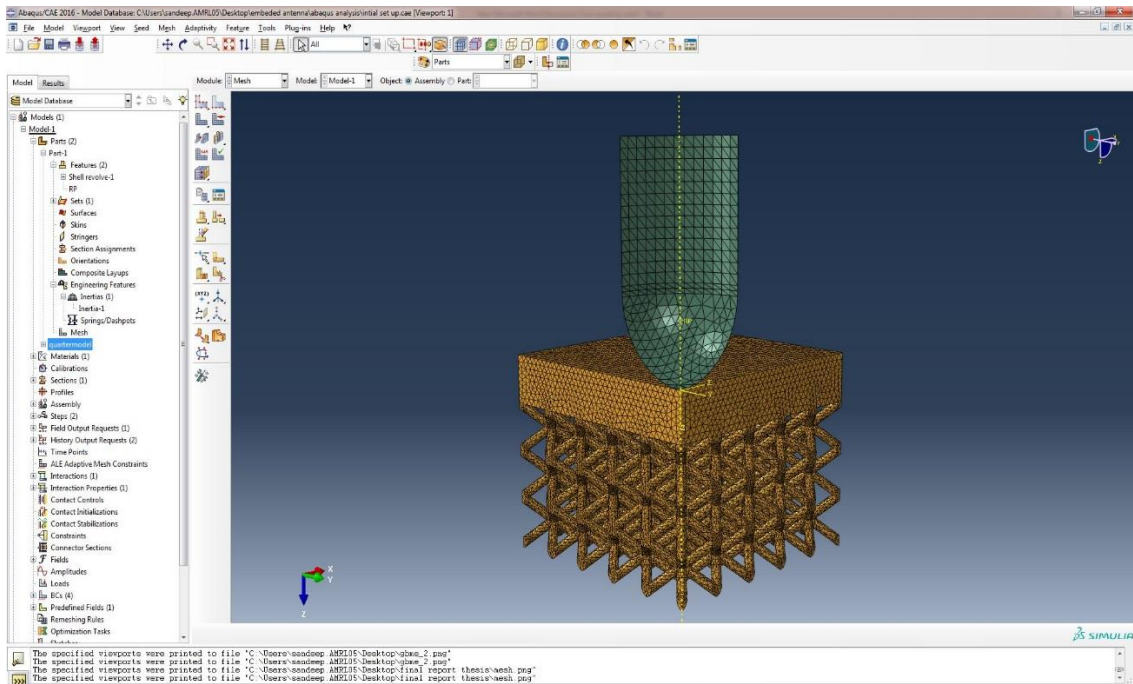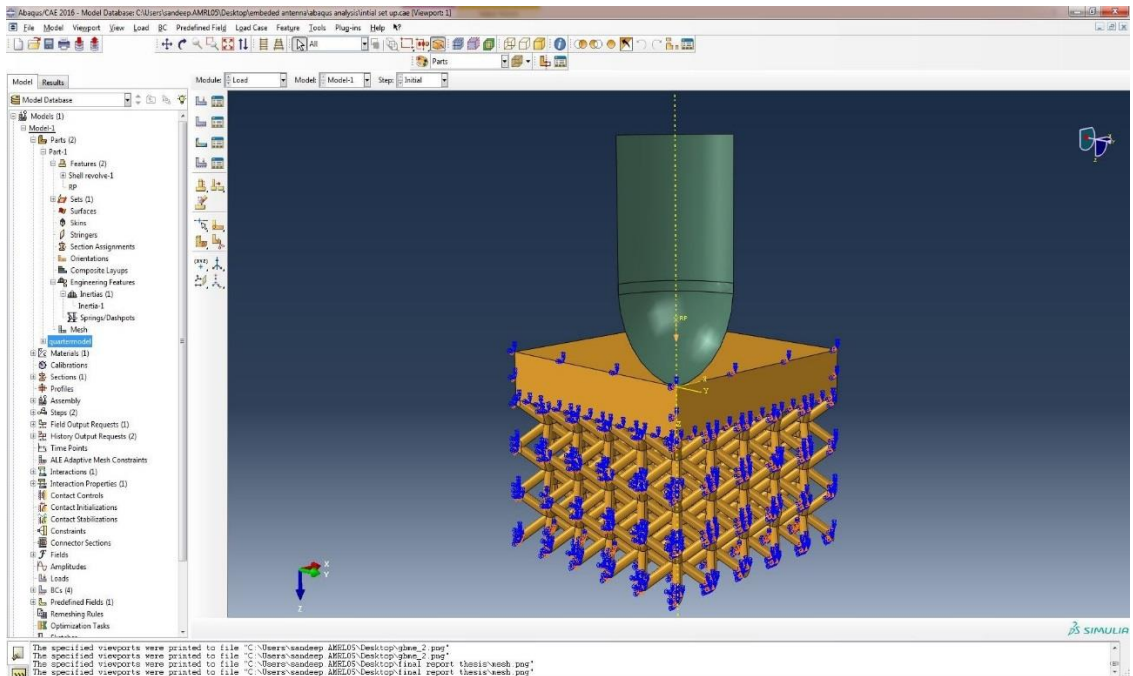
```
% Plot Absorption Energy vs time
figure(6)
hold on
h = plot(t3,A_E,'bl','LineWidth',2);
xlabel('Time (sec)')
ylabel('Absorption Energy (ft-lb)','FontSize',14);
grid on;
```
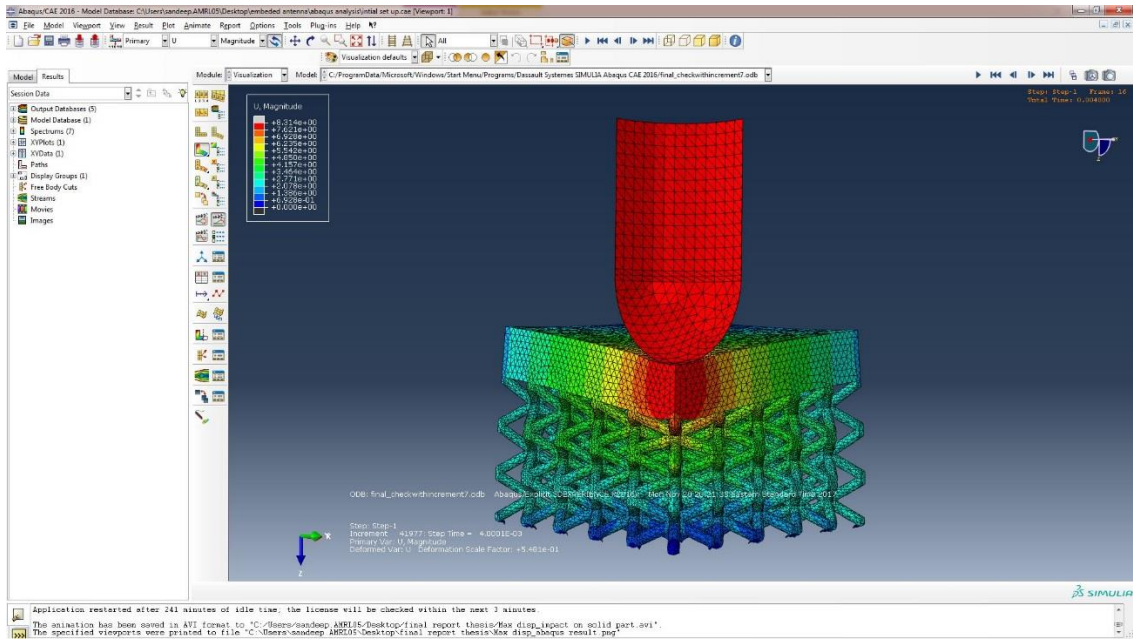
ABAQUS/Explicit Dynamics

The following pictures of hybrid structure are screenshot images of the ABAQUS window. The picture include model assembly, meshing size, boundary conditions and maximum displacement result.

Material properties of ABS material

ABS > Constants

Density	7.92e-007 kg mm^-3

ABS > Isotropic Elasticity

Temperature C	Young's Modulus MPa	Poisson's Ratio	Bulk Modulus MPa	Shear Modulus MPa
22	861.59	0.35	957.32	319.11